Modelling Structural Phase Transitions in Crystalline Solids

Da Silva, Estelina Lora

Award date:
2018

Awarding institution:
University of Bath

Modelling Structural Phase Transitions in Crystalline Solids

Da Silva, Estelina Lora

Award date:
2018

Awarding institution:
University of Bath

Modelling Structural Phase Transitions in Crystalline Solids

submitted by

Estelina Lora da Silva

for the degree of Doctor of Philosophy

of the

University of Bath

Department of Chemistry

February 2018

Acknowledgments

I would like to express my very great appreciation for my supervisors, Professors Aron Walsh, Steve Parker and Paul Raithby, who, since the very early stages of my work, have motivated me to pursue the goals of the project, and have enabled me to undertake my research at the University of Bath. Special thanks go to Prof. Aron Walsh, Drs. Jonathan Skelton, Keith Butler and Scott Mckechnie (King's College of London) who have provided scientific guidance for the computational methodologies, as well as fruitful discussions, which were essential for a good understanding of the foundations and methods employed in this work. I also acknowledge many discussions with members of the Walsh group in which I was pleased to participate. I also want to express the support and guidance provided by my very good friends Drs. Marco Molinari (University of Huddersfield) and Yang Tao (Chinese Academy of Sciences).

This work is supported by EPSRC Programme Grants (No. EP/K004956/1 and EP/K016288/1) and the ERC (Grant No. 277757). I acknowledge use of the ARCHER supercomputer through membership of the UK HPC Materials Chemistry Consortium, which was funded by EPSRC grant no. EP/L000202, and also by the Partnership for Advanced Computing in Europe (PRACE DECI-13 Panel - 13DECI0313), in the completion of this work. I also acknowledge computing support from the University of Bath Computing Services, which maintain the Balena HPC cluster and the local clusters from the WMD group.

Dedicated to my husband and son, Mario and Ary

Summary

Computer simulations of solids have become increasingly powerful and predictive, particularly, those based on first-principles approaches such as density functional theory (DFT). Lattice dynamics has also become an important theme related to materials science and is essential for understanding the thermal properties of crystalline solids at finite temperatures. This thesis focuses on understanding the nature of collective atomic vibrations (phonons) in solids and their role in structural phase transitions. First-principles lattice dynamics approaches - within the harmonic and quasi-harmonic approximations - are applied to describe phase transformations in the metal halide perovskite $CsSnI_3$ and the nature of the cubic to rhombohedral ferroelectric distortion in the semiconductor GeTe. The aim is therefore to demonstrate the advantages and shortcomings of quasi-harmonic approximations and to benchmark this method on these two challenging systems. Further approaches were applied to GeTe in order to evaluate the effect of the different levels of physical complexity regarding the nature of the transition, e.g. quasi-particle self-consistent GW (QSGW). In addition to the role of temperature, we also probe the effect of an external bias on phase stability taking the case of AB and AA bilayer graphene under an applied voltage.

Publications during the course of the PhD

8. Lattice Dynamics of the Rashba Effect in GeTe
   E. Lora da Silva, S. McKechnie, M. van Schilfgaarde, J. M. Skelton, S. C. Parker, and A. Walsh. In revision and to be submitted (2018).

7. Monitoring Photo-induced Population Dynamics in Metastable Linkage Isomer Crystals: A Crystallographic Kinetic Study of $[Pd(Bu_4dien)NO_2]BPh_4$
   L. E. Hatcher, J. M. Skelton, M. R. Warren, C. Stubbs, E. Lora da Silva and P. R. Raithby. Accepted in Phys. Chem. Chem. Phys. (2017), doi: 10.1039/C7CP05422J.

6. Spontaneous Octahedral Tilting in the Cubic Inorganic Caesium Halide Perovskites $CsSnX_3$ and $CsPbX_3$ (X = F, Cl, Br, I)
   R. X. Yang, J. M. Skelton, E. Lora da Silva, J. Frost, A. Walsh. J. Phys. Chem. Lett. 8 (19), 4720 (2017).

5. Bias polarization study of steam electrolysis by composite oxygen electrode Ba0.5Sr0.5Co0.8Fe0.2O3-δ/BaCe0.4Zr0.4Y0.2O3-δ
   Tao Yang, A. Shaula, D. Pukazhselvan, D. Ramasamy, J. Deng, E. L. da Silva, R. Duarte, J. A. Saraiva Appl. Surf. Sci. 424P1, 82 (2017).

4. Electronic structure of interstitial hydrogen in lutetium oxide from DFT+U calculations and comparison study with μSR spectroscopy
   E. Lora da Silva, A. G. Marinopoulos, R. B. L. Vieira, R. C. Vilão, H. V. Alberto, J. M. Gil, R. L. Lichti, P. W. Mengyan, and B. B. Baker. Phys. Rev. B 94, 014104 (2016).

3. Can core flows inferred from geomagnetic field models explain the Earth's dynamo?
   N. Schaeffer, E. Lora Silva, M.A. Pais. Geophys. J. Inter. 204, 868 (2016).

2. Phase stability and transformations in the halide perovskite $CsSnI_3$
   E. Lora da Silva, Jonathan M. Skelton, Stephen C. Parker, and Aron Walsh. Phys. Rev. B 91, 144107 (2015).

1. Electronic excitations in molecular solids: bridging theory and experiment
   Jonathan M. Skelton, E. Lora da Silva, Rachel Crespo-Otero, Lauren E. Hatcher, Paul R. Raithby, Stephen C. Parker and Aron Walsh. Faraday Discuss. 177, 181 (2015).

Contents

List of Figures

List of Tables

Chapter 1

Introduction

Nothing is permanent in this wicked world, not even our troubles
Charles Chaplin

Make-Measure-Model-Manipulate (M4) is a Research Council funded Programme, aimed to develop new types of switchable materials based on the generation and control of metastable states in molecular systems. It is based on an interdisciplinary collaboration between experimental and theoretical groups, where expertise in synthesis, characterisation, modelling, and device fabrication are brought together. My work within this project was to provide computational modelling support to the experimental work through the characterisation and understanding of excited- and transition-state features at the atomistic level, and therefore providing fundamental understanding to direct the optimisation of the metastable states for potential technological applications.

Density Functional Theory (DFT) is a well-established computational tool to study the structural and electronic properties on systems in thermodynamic equilibrium; however, interesting phenomena tend to occur for systems perturbed by external stimuli such as temperature, pressure, light, external bias (i.e. phase transitions). Therefore one should resort to other methodologies in order to probe the properties of phase-changing materials, and hence study the structural stability of the different phases, which can be metastable or transition-states.

Lattice dynamics is becoming increasingly important to study the structural stability of systems and results derived from such calculations explain many of the thermodynamic properties of solids by relating anomalous phonon behaviour to structural changes in solids. Moreover, lattice-dynamics calculations within the quasi-harmonic approximation (QHA) has been established as an inexpensive and powerful means to model the temperature dependence of properties on the density functional theory (DFT) free-energy surface.

For a given pressure p and temperature T the equilibrium state of the system presents

different microscopic properties (density, chemical composition, magnetisation) which are the characteristic of each phase of matter. When a change of phase occurs (phase transition), mostly due to application of an external perturbation, the microscopic properties change and these are related to the order of the transition.

According to Ehrenfest's classification scheme the order of a transition may be classified through the Gibbs thermodynamic potential [13]. When the first derivative of the potential is discontinuous across the phase boundary we have a first order phase transition. This implies that the volume V and the entropy S are also discontinuous[1]. Since the entropies between the phases are different, the system must absorb or release heat during the transition.

Continuous phase transitions involve a continuous change in entropy and volume, although show discontinuities in the second derivatives of the Gibbs potential, and therefore are also known as second order phase transitions. These phase transitions show discontinuities of the response functions (susceptibilities), such as the specific heat C_p, the isothermal compressibility κ_T and the volume expansivity β_P [2] [13].

$CsSnI_3$ is an interesting inorganic halide-perovskite system, with ABX_3 stoichiometry, exhibiting a number of phase changes, with two high-temperature phases and two ground-state phases [14, 15]. In order to bring new insight to the dynamical stability of these polymorphs, the effect of temperature is modelled by using lattice dynamics calculations, within the QHA. In particular focus was given to the temperature dependence of structural properties and the thermodynamic stability of the four phases. The contributions of the structural distortions from the high-symmetry cubic structure to the ground-state orthorhombic phase were also analysed by employing symmetry-mode analysis techniques [16].

Other appealing materials, lacking inversion symmetry, which have started to gain interest amongst the scientific community are the Ferroelectric Rashba Semi-Conductors (FERSC) [17, 18]. These materials combine directed polarisation (ferroelectricity) and spin-orbit coupling (SOC) effects. The resulting relativistic electronic structure can display a Rashba effect (momentum-dependent splitting of spin bands), with spin texture being controllable and switchable via an electric-bias. The best-known FERSC due to its structural simplicity, is the prototypical GeTe [17], exhibiting a high-temperature phase, which is an ideal rocksalt structure, and a ground-state ferroelectric rhombohedral phase. Not only the QHA was employed to study the dynamical stability of the two phases of GeTe, but also many-body perturbation theory has been applied (relativistic calculations using self-consistent methods, QSGW), in order to reproduce the Rashba electronic band structure of the ferroelectric phase. To analyse the macroscopic mechanism of the ferroelectric transition, and to model the material properties

[1] $\left(\frac{\partial G}{\partial T}\right)_p = -S, \qquad \left(\frac{\partial G}{\partial p}\right)_T = V$

[2] $-T\left(\frac{\partial^2 G}{\partial T^2}\right)_p = C_p, \qquad -\frac{1}{V}\left(\frac{\partial^2 G}{\partial p^2}\right)_T = \kappa_T, \qquad \frac{1}{V}\left(\frac{\partial^2 G}{\partial T \partial p}\right) = \beta_P$

through the phase transition, one also needs to apply phenomenological Landau theories. By employing this model, in conjunction with the DFT free-energy calculations, it was possible to calculate the evolution of the polarisation, from the centrosymmetric to the ferroelectric phase, and assess the hysteresis behaviour for this specific spin-orbit coupled system.

The last and also interesting project, is related to the bilayer graphene (BLG) system, which can coexist with different stacking environments: the Bernal (or AB) and the AA structure. The interest in BLG is mainly due to the possibility of inducing a semiconductor with a tunable band gap [19]. However, the most reliable structure for external tuning is observed for the Bernal-stacked BLG and this tuning has been evidenced through the application of an electric field normal to the layers. For this project the electronic structure of the two stacking environments of the bilayer system have been studied, in order to probe the widths of the band-gaps as a function of different voltage bias strengths, and also the respective scaling behaviour of the band dispersion. Spin-orbit coupling has been considered for the electronic properties and energy dispersions were compared against the bias intensities of the two systems. Moreover, lattice dynamics have been also considered to study the structural stabilities of the biased and unbiased AB and AA stacking BLG systems.

This thesis is structured into six main chapters. Following this first chapter, we present a second chapter that details the theoretical framework of the methods employed in the present work, describing density-functional theory, many-body perturbation theory and lattice-dynamics (the (quasi-)harmonic approximation). Moreover, in this chapter a theoretical overview regarding the required physical observables to analyse a ferroelectric system is also provided. Chapter three, four and five refer to the obtained results and respective discussions, mainly on: 3) the $CsSnI_3$ system that has been taken as a more complex case study for application of the QHA; 4) methodology applied to study the paraelectric-to-ferroelctric structural phase transition of GeTe; 5) effects of an applied external electric field on the electronic and phonon properties of the AB and AA systems of BLG. The sixth chapter provides the conclusions and a perspectives for future work, which can be followed as a continuation of the present work within the PhD project.

Chapter 2

Theoretical Framework

Art is the lie that enables us to see the truth
Pablo Picasso

2.1 The Many-Body Problem

In order to solve the many-body Schrödinger equation for a quantum system of N interacting fermions, several approximations can be employed, which are simplifications of the full problem of many electrons moving in an external potential field [20].

The many-body Schrödinger equation involves a set of N_e electrons and N_n atomic nuclei, of the form

$$\widehat{H}\Psi(\mathbf{R},\mathbf{r}) = E\Psi(\mathbf{R},\mathbf{r}), \tag{2.1}$$

where the wavefunction of the system depends on the $3N_n$ coordinates of the nuclei, $\mathbf{R}$, and the $3N_e$ coordinates of the electrons. This interacting system is usually described by the Hamiltonian, $\widehat{H}$, containing the kinetic and potential terms: [1]

$$\widehat{H} = -\frac{1}{2}\sum_{i}^{N_e}\nabla_i^2 - \sum_{\alpha}^{N_n}\frac{1}{2M_\alpha}\nabla_\alpha^2 + \frac{1}{2}\sum_{\substack{i,j=1\\ i\neq j}}^{N_e}\frac{1}{|\mathbf{r}_i-\mathbf{r}_j|} - \sum_{i,\alpha=1}^{N_e,N_n}\frac{Z_\alpha}{|\mathbf{r}_i-\mathbf{R}_\alpha|} + \frac{1}{2}\sum_{\substack{\alpha,\beta=1\\ \alpha\neq\beta}}^{N_n}\frac{Z_\alpha Z_\beta}{|\mathbf{R}_\alpha-\mathbf{R}_\beta|}, \tag{2.2}$$

where M_α, Z_α and $\mathbf{R}_\alpha$ represent the mass, charge and location of the α-th nucleus, and $\mathbf{r}_i$ the coordinate of the i-th electron. The total wavefunction is thus a function of N_n plus N_e coordinates (disregarding spin degrees of freedom), respectively [21], i.e.:

$$\Psi \equiv \Psi(\mathbf{r}_1,\ldots,\mathbf{r}_{N_e};\mathbf{R}_1,\ldots,\mathbf{R}_{N_n}). \tag{2.3}$$

[1] Quantities are expressed in atomic units, where the $\hbar$, the electron charge e, the electron mass m and the permittivity of vacuum $4\pi\epsilon_0$, are taken to be unity.

One of the first simplifications to solve the many-body problem was the Born-Oppenheimer approximation (1927) [22]. The first assumption of this approach considered that the Schrödinger equation describing the electronic system could be solved by the field of fixed nuclei, due to the mass of the nuclei being 2000 times bigger than the mass of the electrons [23]. The kinetic energy of the nuclei can therefore be neglected, since respective term is much smaller than the kinetic term of the electrons (second term of Eq. 2.2). Moreover, the repulsion term between nuclei can be considered a constant (last term of Eq. 2.2), and will only contribute with a constant shift to the eigenvalues.

Within this assumption, the wavefunction can thus be approximated by considering a fixed nuclear configuration of the form:

$$\Psi(\mathbf{r},\mathbf{R}) = \psi_{\mathrm{N}_e}(\mathbf{r},\mathbf{R})\phi_{\mathrm{N}_n}(\mathbf{R}) \tag{2.4}$$

where ψ_{N_e} and ϕ_{N_n} are separate electronic and nuclear wavefunctions, respectively (the electronic wavefunction depends on the nuclear positions, $\mathbf{R}$, parametrically). The electronic wavefunction is therefore solved for a given set of nuclear coordinates, written as

$$\begin{aligned} H_{\mathrm{N}_e}\psi_{\mathrm{N}_e}(\mathbf{r},\mathbf{R}) &= \left\{ -\frac{1}{2}\sum_{i}^{N_e}\nabla_i^2 + \frac{1}{2}\sum_{\substack{i,j=1\\ i\neq j}}^{N_e}\frac{1}{|\mathbf{r}_i-\mathbf{r}_j|} - \sum_{i,\alpha=1}^{N_e,N_n}\frac{Z_\alpha}{|\mathbf{r}_i-\mathbf{R}_\alpha|}\right\}\psi_{\mathrm{N}_e}(\mathbf{r},\mathbf{R}) \\ &= E_{\mathrm{N}_e}(\mathbf{R})\psi_{\mathrm{N}_e}(\mathbf{r},\mathbf{R}). \end{aligned} \tag{2.5}$$

The Coulomb interactions between electrons and nucleus are still considered, with the nuclei $\mathbf{R}$ varying at infinitesimally small positions in space (adiabatic approximation), and thus obtaining the electronic energy as a function of $\mathbf{R}$ (potential energy surface). For small displacements around a minimum, the potential energy surface can be approximated by a parabola thus leading to the Harmonic Approximation (Sec. 2.4.1) [23, 24].

The second assumption of the Born-Oppenheimer approximation is considering the nuclear kinetic term to compute the Schröodinger equation for the nuclear motions, with the nuclei moving in a averaged potential set up by the electronic coordinates. The electronic energy obtained by Eq. 2.5, will thus contribute with a potential term to the motion of the nuclei

$$\begin{aligned} H_{\mathrm{N}_n}\phi_{\mathrm{N}_n}(\mathbf{R}) &= \left\{ -\frac{1}{2}\sum_{\alpha}^{N_n}\frac{1}{2M_\alpha}\nabla_\alpha^2 + \sum_{\substack{\alpha,\beta=1\\ \alpha\neq\beta}}^{N_n}\frac{Z_\alpha Z_\beta}{|\mathbf{R}_\alpha-\mathbf{R}_\beta|}\right\}\psi_{\mathrm{N}_n}(\mathbf{R}) + E_{\mathrm{N}_e}(\mathbf{R}) \\ &= E_{\mathrm{tot}}\phi_{\mathrm{N}_n}(\mathbf{R}). \end{aligned} \tag{2.6}$$

where the nuclear wavefunction will account for the vibrational, translational, and rotational properties of the system (Sec. 2.4) [23].

The Born-Oppenheimer approximation fails when one cannot disregard the strong interaction between electrons and nuclei, as is the case for systems where electron-phonon coupling is significant, i.e. superconductors [21].

Hartree (1928) [25] attempted to replace the Coulomb interaction by an effective electron-electron potential, $U_{\mathrm{ee}}(\mathbf{r})$, in which each electron moves in a field produced by a sum over all the other electrons. This term was suggested to have the following form:

$$U_{\mathrm{ee}}(\mathbf{r}) = \int d\mathbf{r}' \frac{n(\mathbf{r}')}{|\mathbf{r} - \mathbf{r}'|}, \tag{2.7}$$

with n being the density of electrons at one point in space $\mathbf{r}$

$$n(\mathbf{r}) = \sum_j |\psi_j(\mathbf{r})|^2. \tag{2.8}$$

In this simple approximation, the electronic correlation is not accounted for, and therefore the many-body Schrödinger equation is decoupled into N_e one-electron equations. This results in the Hartree equation [26]

$$-\frac{1}{2}\nabla^2\psi_l + [U_{\mathrm{n}}(\mathbf{r}) + U_{\mathrm{ee}}(\mathbf{r})]\psi_l = \varepsilon_l\psi_l \tag{2.9}$$

where U_{n} is the potential defined by the nuclear-electron interaction.

Due to the nature of the one-electron Hartree equation, Eq. 2.9, the Pauli exclusion principle is not recognized: whenever two electrons with identical spin states occupy the same position, the true many-body wavefunction has to vanish. Later on, Fock and Slater (1930) suggested that due to the fermionic character of the electrons a space of antisymmetric wavefunctions would be required. The many-electron wavefunction would thus have the form of an antisymmetrised product of one-electron wavefunctions [20, 26].

The simplest possible type of antisymmetric wavefunction can be obtained by taking a collection of orthonormal one-particle wavefunctions

$$\int \psi_i^*(\mathbf{r})\psi_j(\mathbf{r})d\mathbf{r} = \delta_{ij} \tag{2.10}$$

and antisymmetrizing them, in the form of a Slater determinant:

$$\Psi(\mathbf{r}_1\sigma_1 \cdots \mathbf{r}_N\sigma_N) = \frac{1}{\sqrt{N!}} \sum_s (-1)^s \psi_{s_1}(\mathbf{r}_1\sigma_1) \cdots \psi_{s_N}(\mathbf{r}_N\sigma_N) \tag{2.11}$$

$$= \frac{1}{\sqrt{N!}} \begin{vmatrix} \psi_1(\mathbf{r}_1\sigma_1) & \psi_1(\mathbf{r}_2\sigma_2) & \cdots & \psi_1(\mathbf{r}_N\sigma_N) \\ \vdots & \vdots & \ddots & \vdots \\ \psi_n(\mathbf{r}_1\sigma_1) & \psi_n(\mathbf{r}_2\sigma_2) & \cdots & \psi_n(\mathbf{r}_N\sigma_N) \end{vmatrix} \tag{2.12}$$

where the sum is over all permutations s (the sign is $+1$ or -1 depending on whether the permutation can be written as a product of an even or odd number of pair interchanges).

Because this wavefunction is not a simple product, but a determinant, the Pauli principle induces correlations among particles, and therefore the spin index σ_i (taking values ± 1) is included in every wavefunction. The wavefunction can be written in the form

$$\psi_l(\mathbf{r}_i\sigma_i) = \psi_l(\mathbf{r}_i)\chi_l(\sigma_i) \tag{2.13}$$

with $\chi_l(\sigma_i)$ being the spin-function, satisfying [27]

$$\sum \chi_l^*(\sigma_i)\chi_k(\sigma_i) = \delta_{lk}. \tag{2.14}$$

The expectation value of the energy, is

$$E = \sum_l \langle \psi_l | h_l + \frac{1}{2}(J_l - K_l) | \psi_l \rangle, \tag{2.15}$$

where $\hat{h} = \sum_l h_l$ is the one-electron integral of the form

$$h_l = \frac{1}{2}\nabla_l^2 - \sum_n \frac{Z_n}{\mathbf{r}_l - \mathbf{R}_n}, \tag{2.16}$$

$\hat{J} = \sum_l J_l$ is the Coulomb operator (electron-electron repulsion term) and $\hat{K} = \sum_l K_l$ is the exchange operator (spin-correlation effects), with

$$J_l(\mathbf{r}) = \sum_k \int\int \psi_l(\mathbf{r})\psi_l^*(\mathbf{r})\frac{1}{|\mathbf{r} - \mathbf{r}'|}\psi_k(\mathbf{r}')\psi_k^*(\mathbf{r}')\, d\mathbf{r}\, d\mathbf{r}' \tag{2.17}$$

$$K_l(\mathbf{r}) = \sum_k \int\int \psi_l(\mathbf{r})\psi_k^*(\mathbf{r})\frac{1}{|\mathbf{r} - \mathbf{r}'|}\psi_k(\mathbf{r}')\psi_l^*(\mathbf{r}')\, d\mathbf{r}\, d\mathbf{r}'. \tag{2.18}$$

By minimizing 2.15 as a function of the spin-orbitals, ψ_l, composing the many-electron ground-state, this gives the Hartree-Fock equations:

$$\hat{F}\psi_l = \epsilon_l \psi_l, \tag{2.19}$$

where $\hat{F}$ is known as the Fock operator (the effective one-electron operator), defined as $\hat{F} = \hat{h} + \hat{J} - \hat{K}$.

Equation 2.19 is a Schrödinger-like equation, with ϵ_l being a Lagrange multiplier that has to be chosen such that it ensures orbital orthonormalization. These can be identified as the one-electron orbital energies.

Configuration interaction (CI) wavefunctions can provide very reliable results for potential energy surfaces, electronic excited states, etc. However, such wavefunctions are also difficult to evaluate due to their extreme computational cost, since these represent the exact solution of the electronic Schrödinger equation for a fixed one-particle basis set. For very large configuration spaces, the number of CI coupling coefficients becomes prohibitively large to store on disk; these coefficients must be evaluated as needed in a so-called direct CI procedure [20].

In the CI approach the many-body wavefunction is written as a linear combination of Slater determinants ψ of the form:

$$|\Psi_{\mathrm{CI}}\rangle = \sum_i c_j |\psi\rangle. \tag{2.20}$$

By inserting the expansion into the Schrödinger equation

$$\hat{H} \sum_i c_j |\psi\rangle = E \sum_i c_j |\psi\rangle \tag{2.21}$$

and multiplying with the determinants one obtains:

$$\sum_i H_{ij} c_j = E \sum_i S_{ij} c_j |\psi\rangle \tag{2.22}$$

where $H_{ij} = \langle \psi_i | \hat{H} | \psi_j \rangle$ and $S_{ij} = \langle \psi_i | \psi_j \rangle = \delta_{ij}$.

The full CI method is impossible to compute, and the best determinants which lead to the closest ground-state energy have hence to be chosen. This can be achieved from the Hartree-Fock method, by approximating the wavefunction by a single Slater determinant [20].

2.2 Density Functional Theory

2.2.1 The Kohn-Sham Equations

Density Functional Theory (DFT) is based on the work performed on electronic-structure methods by Hohenberg, Kohn and Sham in 1965 [28, 29], and is presently one of the most successful approaches to compute the ground-state properties of a system described by quantum mechanics.

Within this approach, the electron orbitals are obtained as solutions of a set of Schrödinger-like equations, referred to as the Kohn-Sham equations, in which potential terms depend solely on the electron density, $n(\mathbf{r})$, instead of a many-body function of $3N$ electronic degrees of freedom [30].

The ground state density is thus obtained through the solution of the Kohn-Sham equations,

which have the form of the single-particle Schrödinger equation:

$$\Big[-\frac{\nabla^2}{2} + v_{\mathrm{KS}}[n(\mathbf{r})] \Big] \varphi_i(\mathbf{r}) = \epsilon_i \varphi_i(\mathbf{r}), \tag{2.23}$$

where v_{KS} is the Kohn-Sham potential, a functional of the non-interacting electron density, n, which is itself defined in terms of the Kohn-Sham wave-functions and constructed by summing over occupied orbitals:

$$n(\mathbf{r}) = \sum_{i}^{occ} |\varphi_i(\mathbf{r})|^2. \tag{2.24}$$

The Kohn-Sham potential can be defined as the sum of three terms: the external potential, v_{ext}, which is the Coulomb attraction between the bare nuclei and the electrons; the Hartree term, v_{Hartree}, which represents the electrostatic energy of the electron in the field generated by the total electron density; and the exchange-correlation (xc) potential, v_{xc} [1]:

$$v_{\mathrm{KS}}[n(\mathbf{r})] = v_{\mathrm{ext}}(\mathbf{r}) + v_{\mathrm{Hartree}}[n(\mathbf{r})] + v_{\mathrm{xc}}[n(\mathbf{r})]. \tag{2.25}$$

The last term of Eq. 2.25, the xc potential, takes the form of a functional derivative over the density, such that:

$$v_{\mathrm{xc}}[n(\mathbf{r})] = \frac{\delta E_{\mathrm{xc}}[n(\mathbf{r})]}{\delta n(\mathbf{r})}. \tag{2.26}$$

The electron exchange term describes the exchange symmetry when two particles are exchanged. For any particle characterized by Fermi-Dirac statistics with half-integer spin (fermions), which includes electrons, this effect obeys the Pauli exclusion principle, preventing two parallel-spin particles from being found at the same point in space (i.e. orbital). The exchange term lowers the energy by keeping electrons of the same spin away from each other, thus reducing the Coulomb repulsion [31]. Correlation energy, on the other hand, result from the collective behaviour of electrons to screen and decrease the Coulombic interaction; correlations become more pronounced for opposite spins since they are more likely to occupy nearby locations [31, 32].

The exchange-correlation functional is constructed by employing approximations, with many different forms and developed for a wide variety of physical systems and applications.

2.2.2 Expansion of the Kohn-Sham Wave-functions

The Kohn-Sham wave-functions may be expanded using different numerical basis sets. The most natural method to treat periodic systems is an expansion in plane-waves, which takes

advantage of the periodicity of the crystal. The Kohn-Sham equations can then be solved in momentum space.

Application of Bloch's theorem ensures that the Kohn-Sham wave-functions takes the form of a travelling plane-wave modulated by a specific function in order to incorporate the translational periodicity of the system [33], such that:

$$\varphi_{\mathbf{k},n}(\mathbf{r}) = e^{\imath \mathbf{k}\cdot\mathbf{r}} \sum_{\mathbf{G}} c_{\mathbf{k},n}(\mathbf{G}) e^{\imath \mathbf{G}\cdot\mathbf{r}}, \tag{2.27}$$

where $\mathbf{k}$ is the crystal wave-vector restricted to the first Brillouin zone [2], n is the band index, and $\mathbf{G}$ are the reciprocal lattice vectors, related to the primitive vectors of reciprocal space, $\mathbf{b}_{i,j,k}$, of the form $\mathbf{G} = m_1\mathbf{b}_1 + m_2\mathbf{b}_2 + m_3\mathbf{b}_3$, with

$$\mathbf{b}_i = 2\pi \frac{\mathbf{a}_j \times \mathbf{a}_k}{|\mathbf{a}_i \cdot (\mathbf{a}_j \times \mathbf{a}_k)|}. \tag{2.28}$$

where $\mathbf{a}_{i,j,k}$ are the unit-cell vectors and the volume is formed by $V = |\mathbf{a}_i \cdot (\mathbf{a}_j \times \mathbf{a}_k)|$.

The electronic density is

$$n(\mathbf{r}) = \sum_{\mathbf{k},n} \sum_{\mathbf{G},\mathbf{G}'} f_{\mathbf{k},n} c^*_{\mathbf{k},n}(\mathbf{G}') c_{\mathbf{k},n}(\mathbf{G}) e^{\imath(\mathbf{G}-\mathbf{G}')\cdot\mathbf{r}} \tag{2.29}$$

where $f_{\mathbf{k},n}$ are the band occupation numbers. Fourier transformation gives:

$$n(\mathbf{G}) = \sum_{\mathbf{k},n} \sum_{\mathbf{G}'} f_{\mathbf{k},n} c^*_{\mathbf{k},n}(\mathbf{G}' - \mathbf{G}) c_{\mathbf{k},n}(\mathbf{G}'). \tag{2.30}$$

The sums over $\mathbf{k}$ must, in principle, be performed over all Brillouin-zone wave-vectors, but this can be reduced to sums over points in the irreducible Brillouin zone by taking advantage of the space group symmetry of the lattice.

Two technical convergence parameters need to be adjusted for periodic calculations. One of these is the Brillouin zone (BZ) sampling to replace the integration of the periodic functions over reciprocal space. To evaluate these integrals computationally, a weighted sum over a subset of $\mathbf{k}$-points is performed; by taking advantage of the space group symmetry of the lattice, these sums are reduced to the irreducible Brillouin zone [1], thus generating a finite set of representative reducible $\mathbf{k}$-vectors. The second convergence parameter is the cut-off radius set to truncate the sums over the reciprocal lattice vectors. The complete set of reciprocal lattice vectors $\mathbf{G}$ is infinite, and since the orbitals and densities tend to evidence smooth variations at small scales, the plane-wave components become negligible for large $\mathbf{G}$-vectors.

[2] The wave-vector $\mathbf{k}$ is related to the momentum $\mathbf{p}$ of the propagating wave as $\mathbf{k} = \hbar/\mathbf{p}$, where $\hbar$ is the Planck constant.

Therefore it is possible to set the **G**-vectors to a certain cut-off radius, defined in terms of corresponding kinetic energy: $E_{\text{cutoff}} = G_{max}^2/2$, where G_{max} is the radius of the sphere that contains all plane-waves up to the cut-off defined within a volume $V_{\text{sphere}} = (4\pi/3)G_{\text{max}}^3$.

When employing plane-wave basis sets the number of basis states will change discontinuously with cut-off energy. These discontinuities occur at different cut-offs when defining a different **k**-point sampling mesh. At a fixed cut-off energy, a change in the size or shape of the unit-cell will also cause discontinuities in the plane-wave basis set. This problem can be reduced by using a denser **k**-point set, so that the weight attached to the applied plane-wave basis state is reduced. However, the problem can still persist for dense **k**-point samplings and therefore a correction factor can be applied. The correction factor accounts for the difference between the number of states defined in a basis set with an infinitely large number of **k**-points and the number of basis states actually used in a particular calculation [34].

The plane-wave basis sets are complete and orthonormal, without any linear dependency and it is unbiased with respect to the atom positions. It is a simple method to evaluate forces, stresses and force-constants.

For finite systems such as molecules, clusters, surfaces, and other low-dimensional systems, it is also possible to use plane-wave basis sets by placing one finite system in a large enough cell to ensure sufficient space between non-interacting neighbouring images, to avoid spurious interactions between these. This increases the computational cost, since the electron density is concentrated in a small fraction of the total volume of the supercell, a very large number of plane-waves are required. Moreover, for charged systems and/or defect supercell, care needs to be taken to avoid artefacts from of long-range interactions between charged clusters and their periodic images. When the real-space lattice vectors are not large enough, spurious effects from defect- or charge-image coupling can be observed. Different methods exist to correct for the interactions induced by periodic boundary conditions in such structures [**?**, 35, 36].

Other, more efficient, basis sets to expand the Kohn-Sham orbitals exist to model finite systems, which impose the condition that the wave-functions go to zero at a distance far enough from the nuclei. One such type of basis, mostly implemented in quantum-chemistry codes, is the use of localised orbitals such as Gaussian basis sets. The accuracy is determined by the number of functions used and the suitability of the choice of these functions for the specific system. The disadvantage of employing Gaussian basis sets is related to non-orthogonality of the basis therefore giving rise to orbital overlap (Basis Set Superposition Error) and the linear dependency. Real space basis sets can also be employed, where basis functions are sampled on a uniform real-space mesh. In real space convergence of the results has to be checked against the grid size and spacing [1].

The potential diverges close to the nuclei, and the valence electrons feel a strong rapidly-oscillating spherically symmetric Coulomb potential in this region. However, in the interstitial region (far from the nuclei) the potential is weak and the symmetry of the crystal dominates [20].

In order to match the Bloch states of the rapid oscillations near the nuclei, a huge number of plane-waves would be required. Although plane-waves allow for efficient numerical implementations, the number of required plane-waves would be very high compared to other basis-sets. Therefore, plane-waves can only be used in practice after treating the rapid oscillations near the nuclei, using alternative techniques. These include the pseudopotential method and augmented methods.

Pseudopotentials

The Coulomb potential (external potential term of Eq. 2.25) can be treated in the form of an effective potential consisting of the inner core electrons and nucleus. These form an inert core region which interacts with the valence electrons [1], i.e. those which are mostly responsible for the chemical bonding between atoms.

The concept of a pseudopotential was first introduced by Fermi in 1934 [37], when he tried to describe the scattering of a free neutron by a nucleus. In 1935, Hellman [38] suggested a potential form for potassium, replacing the complicated effects of the core electrons with an effective potential (pseudopotential).

It was only in the late 50's that the concept of pseudopotential began to be extensively applied for metals and semiconductors, when Phillips and Kleinman [39] generalised an approximation to Hellmann's original pseudopotential form.

Based on this effective-potential idea, the Schrödinger equation now contains a modified effective-potential term instead of an explicit Coulombic potential for core electrons. The wave-function can thus be written as a sum of a smooth function (pseudo wave-function) plus an oscillating function, to maintain orthogonality between the valence and core electrons [1]:

$$|\psi_v\rangle = |\varphi_v\rangle + \sum_c \alpha_{\mathrm{cv}} |\psi_c\rangle, \tag{2.31}$$

where $\alpha_{\mathrm{cv}} = -\langle\psi_c|\varphi_v\rangle$, $|\psi_v\rangle$ and $|\psi_c\rangle$ are the exact solutions of the Schrödinger equation for the valence and the core electrons, respectively, and $|\varphi_v\rangle$ is the pseudo wave-function.

The Schrödinger equation for the smooth orbital, $|\varphi_v\rangle$, is thus written as

$$\widehat{H}|\varphi_v\rangle = E_v|\varphi_v\rangle + \sum_c (E_c - E_v)|\psi_c\rangle\langle\psi_c|\varphi_v\rangle. \tag{2.32}$$

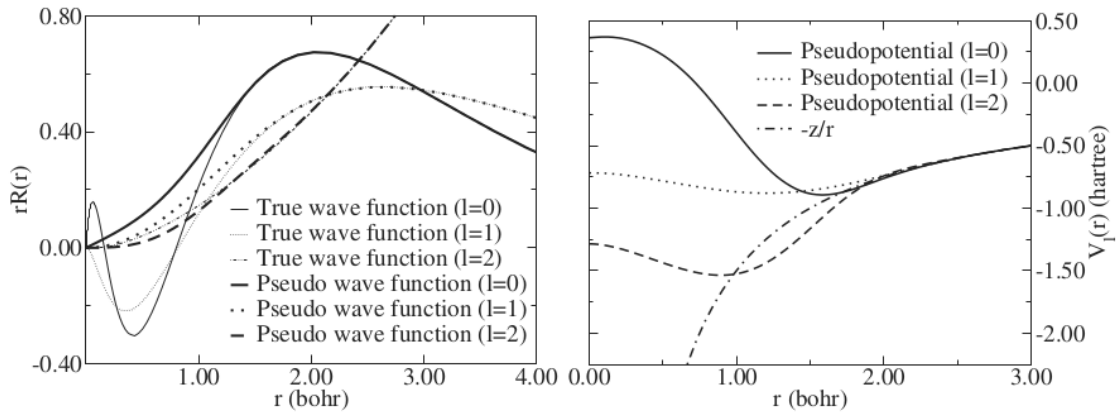

Figure 2-1: Hamann pseudopotential for Al, with $r_0 = 1.24$, $r_1 = 1.54$, and $r_2 = 1.40$ bohr. Comparison is made between the pseudo wave-functions and true wave-functions (left) and pseudopotentials with the Coulomb potential (right) (from Ref. [1]).

Currently, there are three main types of pseudopotentials for plane-wave electronic structure codes in widespread use: norm-conserving, ultrasoft and projector augmented-wave (PAW) pseudopotentials.

Norm-conserving pseudopotentials, first introduced by Hamann, Sclüter and Chiang [40], are constructed using an *ab-initio* procedure and require that the pseudo and all-electron valence eigenstates have the same energies, amplitudes, and charge densities outside the cut-off radius, r_l (Fig. 2-1). The integrated charge inside the cut-off radius for each wave-function must agree (norm-conservation), so that the total charge in the core region is correct and the normalized pseudo-orbital equals the true orbital beyond r_l [24], therefore requiring that the pseudo wave-function has the same norm as the true valence wave-function [1]. The norm-conserving condition is written mathematically as:

$$\begin{aligned} R_l^{\mathrm{PS}}(\mathbf{r}) &= R_{nl}^{\mathrm{AE}}(\mathbf{r}), & \text{if } r > r_l \\ \int_0^{r_l} |R_l^{\mathrm{PS}}(\mathbf{r})|^2 \, r^2 \, dr &= \int_0^{r_l} |R_{nl}^{\mathrm{AE}}(\mathbf{r})|^2 \, r^2 \, dr, & \text{if } r < r_l \end{aligned} \tag{2.33}$$

where $R_l(\mathbf{r})$ is the radial part of the wave-function with angular momentum l, and the superscript PS and AE define the pseudo and all-electron wave-function, respectively.

The cut-off radius can influence the accuracy and the ability of the calculations to reproduce realistic electronic structures in different environments (transferability), this being a measure of the quality of the pseudopotential. The minimum value for the cut-off radius is determined by the location of the outermost nodal surface of the true wave-function. If r_l is close to this minimum, the pseudopotential can reproduce the electronic structure more accurately (a *hard* pseudopotential). If, on the other hand, a very large cut-off radius is chosen, the pseudopo-

tential will be smooth and almost angular-momentum independent (a *softer* pseudopotential), and may not be transferable between widely different systems. A soft potential leads to a fast convergence of the cut-off in plane-wave calculations, and so the choice of the cut-off radius is a balance between basis-set size and pseudopotential accuracy.

Ultrasoft pseudopotentials, where norm-conservation is not enforced, are constructed to describe a particular atomic environment [1], and are therefore often inherently less transferable, but computationally more efficient. The best known approach to constructing ultrasoft pseudopotentials was introduced by Vanderbilt [41] and is quite widely employed, in particular for 3d transition metals where a large plane-wave basis-set is frequently necessary to treat strongly-localized orbitals.

Blöchl [42] further developed the ultrasoft pseudopotential concept by generalizing the pseudopotential and linear augmented plane-wave (LAPW) methods into the projector augmented-wave (PAW) method [42, 43]. This method introduces a linear transformation from the pseudo wave-function to the all-electron wave-function (Kohn-Sham single particle wave-function), operating directly on the full valence and core wave-functions. Similarly to the LAPW method, PAW can be used to treat first-row and transition-metal elements with affordable basis-sets while providing access to the full all-electron wave-function, and thus to a higher accuracy for a given level of optimization. The PAW potentials are generally more accurate than the ultrasoft pseudopotentials, not only because the radial cut-offs are smaller than those defined for the ultrasoft pseudopotentials, but also because the PAW potentials reconstruct the exact valence wave-function with all nodes in the core region [43].

The concept of augmented-wave methods is to divide the wave-function into two parts, namely, a partial-wave expansion within an atom-centred sphere and envelope functions outside the spheres. The envelope function is expanded into plane-waves or other types of basis functions (i.e. Hankel functions). Envelope function and partial-wave expansions (and respective derivatives) are then matched at the sphere boundary radius [42].

In practice the PAW formalism transforms the true wave-functions, $\psi(\mathbf{r})$, onto numerically convenient pseudo (PS) wave-functions, $\varphi(\mathbf{r})$, in order to generate smooth wave-functions with rapidly convergent plane-wave expansion. The transformation is done by considering a transformation operator $\mathcal{T}$ which maps the pseudo- onto the all-electron (AE) wave-functions:

$$|\psi(\mathbf{r})\rangle = \mathcal{T}|\varphi(\mathbf{r})\rangle \tag{2.34}$$

The PS wave-functions will be identified with the envelope functions of the linear methods or the wave-functions of the pseudopotential approach, whereas the AE wave-function is a full one-electron Kohn-Sham wave-function [2].

The total energy will thus be expressed through the PS wave-functions as

$$E[\psi(\mathbf{r})] = E[\mathcal{T}\varphi(\mathbf{r})] \tag{2.35}$$

The transformation operator $\mathcal{T}$ has to modify the smooth PS wave-function in each atomic region, so that the resulting wave-function has the correct nodal structure. Therefore, the operator will be written as the identity with the sum of atomic contributions S_R:

$$\mathcal{T} = 1 + \sum_R S_R \tag{2.36}$$

where R is the atomic site. For every atom, S_R will add the difference between the all-electron and the PS wave-function. Each local contribution, S_R, acts only within some augmentation region enclosing the atom, implying that the all-electron and PS wave-functions will coincide outside the augmentation regions. The equivalent of the augmentation region in the linear methods is the muffin-tin or the atomic sphere (more details in the following subsection). In the pseudopotential method the augmentation region will correspond to the core region [42].

By applying a linear transformation of the form:

$$|\psi\rangle = |\varphi\rangle + \sum_i (|\phi_i\rangle - |\tilde{\phi}_i\rangle)\langle\tilde{p}_i|\varphi\rangle \tag{2.37}$$

the AE wave-function can thus be obtained from the PS wave-function, for each atomic site R represented by the index i. The local terms S_R are defined for each augmentation region by specifying a target function $|\phi\rangle$ (AE partial-waves) of the transformation for a set of initial functions $|\tilde{\phi}\rangle$ (PS partial-waves) which are orthogonal to the core states and satisfy the completeness relations in the augmentation region, such that

$$|\phi_i\rangle = (1 + S_R)|\tilde{\phi}_i\rangle \tag{2.38}$$

The AE partial-waves are solutions to the radial Schrödinger equation. The functions $\langle\tilde{p}|$ are the projector functions, which probe the character of the wave-function and, for exactly each PS partial-wave these must satisfy the orthogonality and completeness condition $\sum_i |\tilde{\phi}_i\rangle\langle\tilde{p}_i| = 1$ within the augmentation sphere, so that the one-centre expansion is identical to the PS wave-function

$$\sum_i |\tilde{\phi}_i\rangle\langle\tilde{p}_i|\varphi\rangle \equiv |\varphi\rangle, \qquad \langle\tilde{p}_i|\tilde{\phi}_j\rangle = \delta_{ij} \tag{2.39}$$

The partial-waves are functions on a radial grid, multiplied with spherical harmonics. The

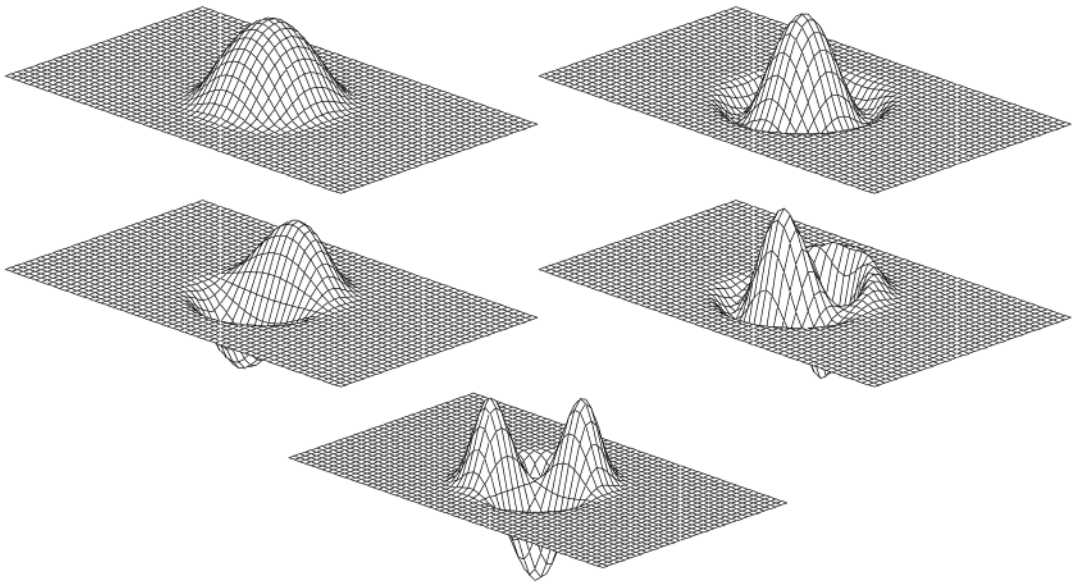

Figure 2-2: Projector functions of the Cl atom for two s-type partial-waves (top), p-type (middle) and d-type (bottom) (from Ref. [2]).

PS wave-functions can be expanded into plane-waves, but other choices are also possible [2].

Augmented Plane-Wave Methods

Augmented-wave methods, originally introduced by Slater (1937) [44], partition space into two different regions: non-overlapping spheres around each nuclei, where the potential is a spherically-symmetric muffin-tin potential; and an interstitial region between atoms, where the potential is smooth and constant [45, 46].

APW methods have the advantage of correctly treating both highly localised atomic-like states (core states), using atomic-like spherical functions, and delocalised valence states, by employing delocalised plane-waves. The disadvantage of the method is the difficulty of matching the functions and solving the resulting non-linear equations [46].

Outside the muffin-tin (MT) spheres, the basis functions are simply defined by plane-waves, $e^{i\mathbf{k}\cdot\mathbf{r}}$, whereas inside the spheres, the basis functions are linear combinations of solutions to the radial Schrödinger equation [24, 20], written as:

$$\sum_{l=0}^{\infty}\sum_{m=-l}^{l} A_{lm}\mathcal{R}_l(r)Y_{lm}(\theta,\phi) \tag{2.40}$$

with $\mathcal{R}_l(r)$ being the solutions to the radial Schrödinger equation[3], the $Y_{lm}(\theta, \phi)$ are the spherical harmonics [47], and the coefficients A_{lm} are found by matching the solution inside the muffin-tin spheres to the plane-wave outside the spheres.

The APW basis functions are formed by basis containing solutions of the radial Schrödinger equation inside each MT sphere and a Bloch wave in the interstitial region, for which the boundary condition needs to match the plane-wave in value. It is possible to match the amplitude of the wave-function across the MT sphere boundary by expanding the plane-wave in spherical harmonics [20]

$$\exp\left(i\mathbf{k}\cdot\mathbf{r}\right) = 4\pi \sum_{l=0}^{l_{max}} \sum_{m=-l}^{l} i^l j_l(kr) Y_{lm}^*(\tilde{k}) Y_{lm}(\tilde{r}) \tag{2.41}$$

where $j_l(kr)$ are the spherical Bessel functions of order l; $\tilde{k}$ and $\tilde{r}$ are the abbreviated notation to refer to the polar angles of vectors $\mathbf{k}$ and $\mathbf{r}$, respectively. The expansions in l and m are defined up to a finite cut-off value l_{max}.

The required matching condition implies that the coefficients of $Y_{lm}(\tilde{r})$ must be equal for both parts of the basis functions, Eqs. 2.40 and 2.41, since $Y_{lm}(\tilde{r})$ form an orthogonal set over the spherical coordinates, therefore fixing the coefficients A_{lm}. We hence obtain the APW basis-function inside the sphere [20]:

$$\psi_{\mathbf{k}}^{\mathrm{APW}}(\mathbf{r}) = 4\pi \sum_{l=0}^{l_{max}} \sum_{m=-l}^{l} i^l \left[\frac{j_l(kr)}{\mathcal{R}_l(R)}\right] \mathcal{R}_l(r) Y_{lm}^*(\tilde{k}) Y_{lm}(\tilde{r}) \tag{2.42}$$

where R is the radius of the sphere.

Within the APW method, the wave-function is approximated in the interstitial region by plane-waves, whereas in the core region the rapid oscillations are incorporated by the direct integration of the Schrödinger equation. The basis functions are continuous at the sphere boundaries, but the expansion functions have discontinuous first derivatives at the surface of the sphere, $r = R$ [33]. The APW functions are not exact solutions of the Schrödinger equation, but they are appropriate basis functions for expanding the wave-function as:

$$\psi_{\mathbf{k}}(\mathbf{r}) = \sum_{\mathbf{G}} C_{\mathbf{G}} \psi_{\mathbf{k}+\mathbf{G}}^{\mathrm{APW}}(\mathbf{r}) \tag{2.43}$$

where the sum runs over all the reciprocal lattice vectors, $\mathbf{G}$.

The APW wave-functions are all evaluated at the same energy value, and the coefficients

[3] $-\frac{1}{2r^2}\frac{d}{dr}\left[r^2\frac{d\mathcal{R}_l(r)}{dr}\right] + \left[\frac{l(l+1)}{2r^2} + V(r)\right]\mathcal{R}_l(r) = E\mathcal{R}_l(r)$

$C_{\mathbf{G}}$ are given by the lowest energy solution of the generalised eigenvalue equation [46] [4].

The APW wave-functions are expanded in energy-dependent basis, where the matrix elements of the Hamiltonian will depend on the energy. Due to this non-linear energy dependency, straightforward application of the matrix methods for the generalised eigenvalue problem is complicated [20].

Linearised methods, introduced by O. K. Andersen in 1975 [48], recover the augmented methods into more useful forms [46]. In the Linear Augmented Plane-Wave (LAPW) method an energy-independent Hamiltonian is employed. A range of energies around a reference value of energy of interest (pivot energy, E_p) [20] are chosen accordingly, for which both the solution of the radial Schrödinger equation and its energy derivative are taken into account when constructing the basis-sets inside the muffin-tins. The radial basis functions can hence be expanded up to first order, and have the form:

$$\mathcal{R}_l(r, E) = \mathcal{R}_l(r, E_p) + (E - E_p)\frac{\partial}{\partial E}\mathcal{R}_l(r, E_p) \tag{2.44}$$

The energy derivatives of the radial solution are employed together with the radial solutions within the muffin-tin spheres to have a continuous match to the plane-waves outside the spheres, whereas within the APW method the first-derivative is discontinuous at the boundary [33, 46]. The APW Hamiltonian depends on the energy only via the radial solutions, $\mathcal{R}_l(r)$, and therefore by taking the energy derivatives at a fixed energy into account, the energy dependence from the Hamiltonian disappears [20]. The expansion of the wave-function thus has the form:

$$\psi_{\mathbf{k}+\mathbf{G}}(\mathbf{r}) = \sum_{l=0}^{l_{max}} \sum_{m=-l}^{l} \left[A_{lm}\mathcal{R}_l(r, E_p) + B_{lm}\frac{\partial}{\partial E}\mathcal{R}_l(r, E_p) \right] Y_{lm}(\theta, \phi) \tag{2.45}$$

where the coefficients A_{lm} and B_{lm} are fixed by the matching condition. The wave-functions are energy-independent and smooth across the sphere boundary. We thus obtain a generalised eigenvalue problem with energy-independent Hamiltonian matrix [20].

The linear method can be extended through the use of local orbitals (LO), a technique termed LAPW+LO, where a third radial function is added to the basis. This inclusion extends the energy range over the eigenvalues to be calculated [45]. The addition of the LO helps treat atoms for which the semicore states extend beyond the sphere radius.

The LAPW+LO basis, inside the sphere, is therefore written as:

$$\psi_{\mathbf{k}}^{LO} = \sum_{l=0}^{l_{max}} \sum_{m=-l}^{l} \left[A_{lm}\mathcal{R}_l(r, E_1) + B_{lm}\frac{\partial}{\partial E}\mathcal{R}_l(r, E_1) + C_{lm}\mathcal{R}_l(r, E_2) \right] Y_{lm}(\theta, \phi) \tag{2.46}$$

[4] $\mathbf{HC} = E\mathbf{SC}$, with $\mathbf{S}$ being the overlap matrix, with elements given by $S_{pq} = \langle \chi_p | \chi_q \rangle$. When the basis consists of non-orthonormal basis functions, it is necessary to reformulate the eigenvalue problem $\mathbf{HC} = E\mathbf{C}$, and include the overlap matrix $\mathbf{S}$.

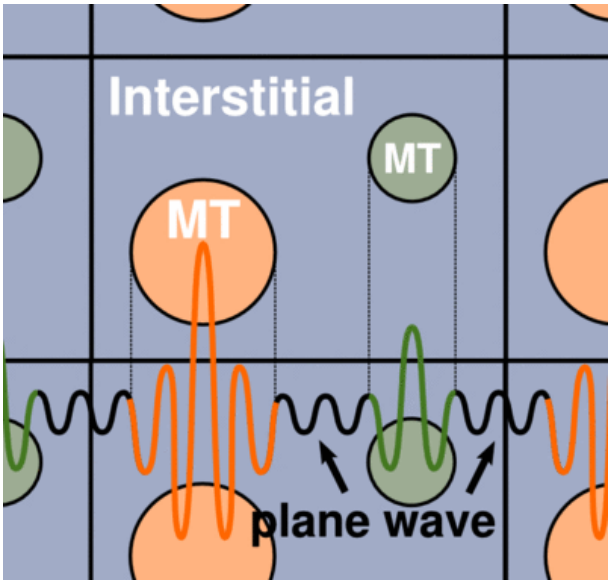

Figure 2-3: Schematic illustration of LAPW basis functions, which consist of a plane-wave, in the interstitial region, augmented by linear combinations of atomic-like functions in the muffin-tin spheres. These are chosen in such as way that the resulting function is continuous across the sphere boundaries (from Ref. [3]).

where the three coefficents are determined by the requirement that the LO should have zero value and energy derivative at the sphere boundary. The reference energy parameters, E_1 and E_2 are chosen based on the valence and semicore position, respectively [49].

Muffin-Tin Orbitals

Muffin-Tin Orbitals (MTO) form a basis of localised augmented orbitals, with the electronic states being described by a small number of functions forming the minimal basis [46]. The localised basis functions are continuous in value and derivative at the sphere boundary. Inside the sphere the orbital is energy-dependent and combines with the wave-function outside the sphere.

O. K. Anderson [50] developed a new set of functions by separating the dependency of κ, the decay constant that characterises the envelope function[5], on r. Inside the sphere the basis function is:

$$\psi_{\mathbf{k}}^{\mathrm{MTO}}(\mathbf{r}, E, \kappa) = i^l \left[\phi_l(E, r) + \kappa \cot\left(\eta_l(E)\right) j_l(\kappa r)\right] Y_{lm}(\theta, \phi) \tag{2.47}$$

[5]In the LAPW and PAW methods, plane-waves are used for envelope functions due to their ability to converge to the basis.

where j_l and η_l are spherical Bessel and Neumann functions, respectively [46]. For negative energies, the Neumann functions are replaced by Hankel functions with asymptotic form $i^{-l}e^{-|\kappa|r}/|\kappa|r$, as $r \to 0$ [46, 51].

Outside the sphere the basis has the form:

$$\psi_{\mathbf{k}}^{\mathrm{MTO}}(\mathbf{r}, E, \kappa) = i^l \kappa \eta_l(\kappa r) Y_{lm}(\theta, \phi) \tag{2.48}$$

Eqs. 2.47 and 2.48 lead to an envelope function (outside the sphere) with the property that each MTO basis-function is well defined both inside the sphere, because $j_l(\kappa r)$ is regular at the origin, and outside the sphere, as $\eta_l(\kappa r)$ is regular at ∞. Within this approach the states will be normalised for all negative energies for any κ.

The linear-MTO method is based on the MTO properties of energy, E, and the decay constant of the envelope function, κ. For a fixed value of κ, a LMTO basis-function inside the sphere is defined as a linear combination of $\phi(E, r)$ and $\dot{\phi}(E, r)$ calculated around a reference energy E_p. The form of the LMTO basis-function inside the sphere is defined by

$$\psi^{\mathrm{LMTO}}(\mathbf{r}, E, \kappa) = i^l \left[\phi_l(E, r) + \kappa \cot\left(\eta_l(E)\right) J_l(\kappa r)\right] Y_{lm}(\theta, \phi) \tag{2.49}$$

and outside the sphere it has the form:

$$\psi^{\mathrm{LMTO}}(\mathbf{r}, E, \kappa) = i^l \kappa N_l(\kappa r) Y_{lm}(\theta, \phi). \tag{2.50}$$

J_l and N_l are similar to the Bessel and Neumann functions, but are fixed by the requirement that the energy derivative of the wave-function vanishes at $E = E_p$. Thus, one obtains an energy-independent LMTO basis-function with $E = E_p$, similar to the basis of the LAPW method.

The LMTO method is well suited to dense solids, but less efficient for open structures such as molecular crystals where atom-centred basis functions are not always adequate for describing the wave-function in large interstitial regions. Very satisfactory results can be obtained for closed packed structures using LMTO basis sets when local orbitals are included to treat the semicore states. LMTO can be more efficient than LAPW, mostly when treating localised states, i.e.: d-states in transition-metals, since LMTOs are localised real-space envelope functions [52]. On the other hand, the LMTO method may be less robust because there is no natural way to converge the basis to completeness.

Plus Muffin-Tin Orbitals

In 2008, Kotani and van Schilfegaarde [52] further developed a method which integrates atom-centred and plane-wave envelope functions in order to increase the flexibility of the basis.

The combination of smooth Hankel functions and APWs is known as the Plus Muffin-Tin (PMT) basis-set. Since MTOs efficiently describe low-energy and localised states, the mixed basis is more efficient than the LAPW method for a given tolerance [52].

The envelope functions of the PMT basis are smoothed versions of Hankel functions, normally adopted for LMTO basis, which consist of a convolution of a Gaussian function with a Hankel function. The smoothness of the function is controlled by an extra degree of freedom, which is the gaussian width or smoothing radius [45]. Unlike the ordinary Hankel functions, which diverge at the origin, PMTs resemble Gaussian functions for small r, and are smooth everywhere. For large r the functions behave like ordinary Hankel functions, and are thus better approximations to the wave-function than Gaussian orbitals [45, 52].

2.2.3 The Exchange-Correlation Potential

The exchange-correlation potential is a functional derivative of the exchange-correlation energy (Eq. 2.26) with respect to the density. To ensure that the Kohn-Sham formulation remains exact, the xc energy is defined as:

$$E_{\mathrm{xc}}[n(\mathbf{r})] = T[n(\mathbf{r})] - T_{\mathbf{S}}[n(\mathbf{r})] + E_{\mathrm{ee}}[n(\mathbf{r})] - E_{\mathrm{Hartree}}[n(\mathbf{r})] \tag{2.51}$$

where $T[n(\mathbf{r})]$ and $E_{\mathrm{ee}}[n(\mathbf{r})]$ are the exact kinetic and electron-electron interaction energies, respectively, and $T_{\mathbf{S}}[n(\mathbf{r})]$ is the Kohn-Sham kinetic energy:

$$T_{\mathbf{S}}[n(\mathbf{r})] = \sum_{i=1} \int \psi_i^*(\mathbf{r}) \Big(-\frac{1}{2}\nabla^2 \Big) \psi_i(\mathbf{r})\, dr \tag{2.52}$$

and E_{Hartree} is the classical Hartree energy of the electrons given by:

$$E_{\mathrm{Hartree}}[n(\mathbf{r})] = \frac{1}{2} \int \int \frac{n(\mathbf{r}) n(\mathbf{r}')}{|\mathbf{r} - \mathbf{r}'|}\, dr dr'. \tag{2.53}$$

The two terms that are not known exactly, the kinetic and electron-electron interaction terms, are grouped into a universal functional, which reproduces the all-electron kinetic and interaction energies and is independent of the external potential, of the form:

$$F_{\mathrm{HK}}[n(\mathbf{r})] = T[n(\mathbf{r})] + E_{\mathrm{ee}}[n(\mathbf{r})] \tag{2.54}$$

where the subscript HK refers to the Hohenberg-Kohn theory, from which the functional is derived. Thus, E_{xc} can be written in terms of Hohenberg-Kohn functional as:

$$E_{\mathrm{xc}}[n(\mathbf{r})] = F_{\mathrm{HK}}[n(\mathbf{r})] - (T_{\mathbf{S}}[n(\mathbf{r})] + E_{\mathrm{Hartree}}[n(\mathbf{r})]). \tag{2.55}$$

The simplest approximation to the exchange-correlation potential is the Local-Density Approximation (LDA). Here, the potential depends solely on the value of the density at the point $\mathbf{r}$, and has the form [1]:

$$E_{\mathrm{xc}}^{\mathrm{LDA}}[n] = \int \varepsilon_{\mathrm{xc}}^{\mathrm{HEG}}[n(\mathbf{r})]\, d^3r \tag{2.56}$$

$$v_{\mathrm{xc}}^{\mathrm{LDA}} = \frac{d}{dn}\varepsilon_{\mathrm{xc}}^{\mathrm{HEG}}[n(\mathbf{r})], \tag{2.57}$$

where $\varepsilon_{\mathrm{xc}}^{\mathrm{HEG}}(n)$ is the xc energy per unit volume of the homogeneous electron gas (HEG) at density n. The spin-polarised version, the Local Spin-Density Approximation (LSDA), is written as

$$E_{\mathrm{xc}}^{\mathrm{LSDA}}[n_\uparrow, n_\downarrow] = \int \varepsilon_{\mathrm{xc}}[n_\uparrow(\mathbf{r}), n_\downarrow(\mathbf{r})]\, d^3r, \tag{2.58}$$

with $\varepsilon_{\mathrm{xc}}(n_\uparrow(\mathbf{r}), n_\downarrow(\mathbf{r}))$ being the exchange-correlation energy per unit volume for an electron gas of uniform spin densities $n_\uparrow$ and $n_\downarrow$.

The exchange energy of the HEG can be analytically calculated from the expression [31]:

$$E_{\mathrm{x}}^{\mathrm{LDA}}[n] = -\frac{3}{4}\left(\frac{3}{\pi}\right)^{1/3} \int n(\mathbf{r})^{4/3}\, dr. \tag{2.59}$$

The correlation energy of the HEG is obtained by parametrizing the results for several densities originally obtained using Monte Carlo methods by Ceperley and Alder [53]. Currently, there exist several parametrized forms for this functional, e.g. PZ81 [54], PW92 [55].

The generalized-gradient approximation (GGA) is a simple extension of the LSDA (Eq. 2.58), and can be seen as an improvement in accuracy, since it attempts to incorporate into ε the effects of inhomogeneities by including the gradient of the electron density ∇n (making it a *semi-local* method)

$$E_{\mathrm{xc}}^{\mathrm{GGA}}[n_\uparrow, n_\downarrow] = \int f(n_\uparrow, n_\downarrow, \nabla n_\uparrow, \nabla n_\downarrow)\, d^3r. \tag{2.60}$$

Some results obtained within the L(S)DA approximation are found to be in very good agreement with experimental data, including in some cases molecular properties such as equilibrium structures, harmonic stretch frequencies, and charge moments [32]. Although successful for some systems, however, this approach can also fail, for example, by incorrectly predicting negative ions to be unstable, underestimating the fundamental energy gaps of semiconductors and insulators, and overestimating the length of hydrogen bonds. Similar to the LDA, GGA also

fails to describe energy band-gaps, which are a crucial physical quantity if one intends to study, e.g. the impurity levels in doped semiconductors. Another common deficiency of (semi-)local approximations is their incorrect description of long-range correlation, in particular van-der-Waals (vdW) interactions. Also, strongly localized $d-$ and $f-$states are incorrectly described as being delocalised, thus resulting in metallic states instead of being insulating as observed in experiment [56]. Despite these failures, the GGA functional can provide reasonably accurate forces, charge-densities and energy barriers.

The earliest semi-local (GGA) functionals had a tendency to overestimate the equilibrium volume, and therefore a revised semi-local functional was constructed for solids - the Perdew-Burke-Ernzerhof parametrization revised for solids (PBEsol) - which has been successful in improving the description of equilibrium properties of densely-packed solids and their surfaces [57, 58], albeit at the expense of less accurate cohesive energies [59].

Most of the problems mentioned above, which result from using the (semi-)local functionals, arise mostly because the correct asymptotic behaviour of the density is not obeyed [60, 61]. In regions that are spatially far away from the system, the density (and its derivatives) decays exponentially to zero [60].

The band-gap, E_{gap}, can be obtained as the difference between the the electron affinity, A, and the ionization potential, I [60, 5], such that:

$$\begin{aligned} A &= E_N - E_{N+1} \equiv -\varepsilon_{\text{LUCO}} \\ I &= E_{N-1} - E_N \equiv -\varepsilon_{\text{HOCO}} \\ E_{\text{gap}} &= I - A = \varepsilon_{\text{LUCO}} - \varepsilon_{\text{HOCO}} \end{aligned} \tag{2.61}$$

where the HOCO and LUCO are the highest occupied and lowest unoccupied crystalline orbitals, respectively.

In DFT, the fundamental gap is not obtained solely as the difference between the Kohn-Sham LUCO, $\varepsilon^{\text{KS}}_{\text{LUCO}}$, and HOCO, $\varepsilon^{\text{KS}}_{\text{HOCO}}$, eigenvalues, but instead has the form [60]:

$$E_{\text{gap}} = \varepsilon^{\text{KS}}_{\text{LUCO}} - \varepsilon^{\text{KS}}_{\text{HOCO}} + \Delta_{\text{xc}} \tag{2.62}$$

where Δ_{xc} is the derivative discontinuity with respect to the number of electrons in the system, N. When a fraction of an electron is added to the system, the Kohn-Sham potential shifts uniformly by a factor of Δ_{xc}. LDA and many GGA functionals do not provide this extra term, since the derivative discontinuity is zero. This problem is responsible for the underestimation of the Kohn-Sham gap when compared to experimental band-gaps [60].

Since Δ_{xc} measures the non-analytical behaviour of the xc energy functional, it can be seen

as being a finite variation of $v_{\mathrm{xc}}(\mathbf{r})$, due to an infinitesimal variation of $n(\mathbf{r})$ [5], i.e.:

$$\Delta_{\mathrm{xc}} = \left(\left.\frac{\partial E_{\mathrm{xc}}[n]}{\partial n(\mathbf{r})}\right|_{N+1} - \left.\frac{\partial E_{\mathrm{xc}}[n]}{\partial n(\mathbf{r})}\right|_{N} \right) + \mathcal{O}\left(\frac{1}{N}\right). \tag{2.63}$$

New approaches to xc functionals have been implemented to try and correct for the asymptotic behaviour, although many modern functionals still do not solve this problem [60]. Improved exchange-correlation functionals have been formulated since the more traditional (semi-)local functionals, and have been grouped into five rungs in a sequence of chemical accuracy, known as the Jacob's ladder of density functional approximations (Fig. 2-4) [30]. As the ladder is ascended, the functionals incorporate higher levels of theory with increasingly complex parameters. These stretch out from the Hartree world (neglecting exchange as well as correlation [25]) up to the heaven of chemical accuracy, such that [4, 30]:

1. The LDA, which constitutes the lowest and most basic rung, using only $n_{\uparrow}(\mathbf{r})$ and $n_{\downarrow}(\mathbf{r})$ as its main parameter.

2. The generalized gradient approximation adds the gradients of the density, $\nabla n_{\uparrow}(\mathbf{r})$ and $\nabla n_{\downarrow}(\mathbf{r})$

3. The meta-GGA approximation which adds the Laplacian of the density $\nabla^2 n_{\uparrow}(\mathbf{r})$ and $\nabla^2 n_{\downarrow}(\mathbf{r})$ and the kinetic energy density, $\tau_{\uparrow}$, and $\tau_{\downarrow}$, making them fully nonlocal functionals of the density. It should be noted, however that the Tao, Perdew, Staroverov, and Scuseria (TPSS) functional does not incorporate the Laplacian of the density, thus avoiding singularities of these Laplacians at the nucleus [62].

4. The hyper-GGA incorporate the exact-exchange energy density, and are fully nonlocal functionals of the occupied Kohn-Sham orbitals (more commonly called hybrid functionals).

5. The exact-exchange can be combined with exact-partial correlation by using both occupied and unoccupied Kohn-Sham orbitals. An example is the random-phase approximation (RPA), which accounts for, dynamical screening effects, and short- and long-range dispersive forces, without the need to resort to empirical corrections [63, 64].

2.3 Many-Body Perturbation Theory

Many-body perturbation theory (MBPT) is a method which accounts for electron correlation by treating it as a small perturbation to the Hamiltonian of the system. Many-body perturbation can therefore treat the many-body correlations as if these were composed by

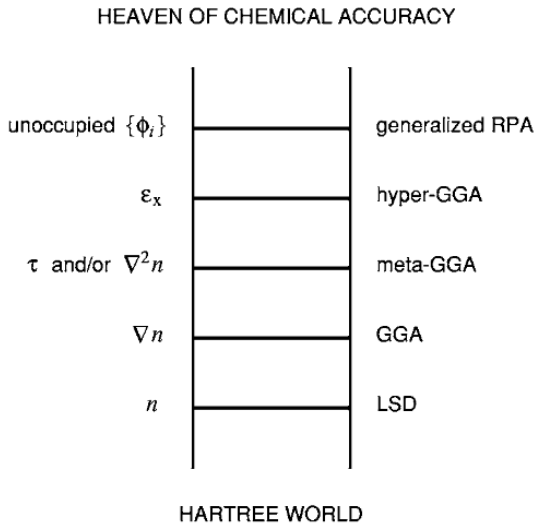

Figure 2-4: Jacob's ladder of density functional approximations to the exchange-correlation energy (from Ref. [4]).

weakly interacting particles, i.e. quasiparticles and collective excitations. In order to calculate the properties of these particles one can resort to quantum field theoretical quantities such as the Green's functions, also known as propagators [65].

The conceptual tool of *GW* is the one-particle Green's function. Knowledge of the Green's function of a system provides the most important physical information such as the ground-state energy and other thermodynamic functions, the energy and lifetime of excited states, and the linear response to external perturbations [66].

The *GW* approximation (GWA) is an alternative to DFT for calculating the electronic properties of materials from first-principles, and can improve on the band-gaps of insulators and semiconductors, hence correcting the systematic DFT underestimation. The name derives from the mathematical form of the self-energy which takes the product the Green's function G and the dynamically screened interaction W, $\Sigma = iGW$ (Fig. 2-6) [6]. In *GW*, the self-energy is given by the Hartree term and Fock term, which is supplemented by the screened Coulomb interaction, W, instead of the bare Coulomb interaction, V[6] (standard Hartree term of Fig. 2-6, single wiggly line). W is calculated within the random phase approximation (RPA), in which the screening is given by the interaction with independent electron-hole pairs [6]. Fig. 2-7 shows the Feynman diagram of the screening interaction: the interaction between two electrons is mediated via a virtual electron-hole pair (Green's function bubble) which causes a dynamical charge redistribution - electrons only *perceive* each other through a screened in-

[6] $V(\mathbf{r}_1, \mathbf{r}_2) = e^2 |\mathbf{r}_1 - \mathbf{r}_2|^{-1}$

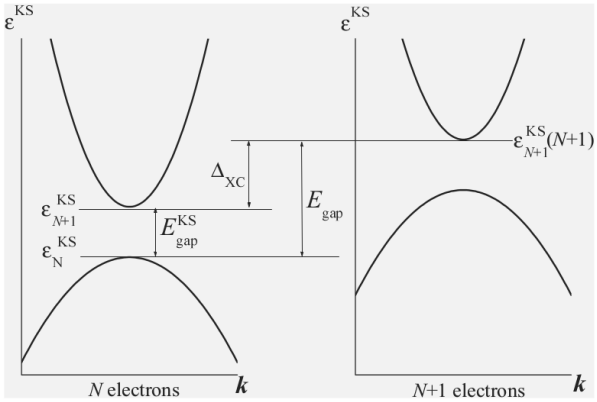

Figure 2-5: Kohn-Sham band-structure of a semiconductor (left). After adding an electron, which occupies the empty conduction band (right), the xc potential and the band-structure shift by an amount of Δ_{xc} (from Ref. [5]).

teraction [6]. The electron correlations included in *GW* can be understood by analysing the diagrams in Fig. 2-8, where by incorporating the screened interaction and the RPA expansion we obtain electronic correlations that go beyond the Hartree-Fock approximation. These include quasiparticle renormalizations, finite quasiparticle lifetimes, band-gap renormalizations [6]. Since the electronic correlations are restricted to only the second line (Fig. 2-8), *GW* is only valid for weakly-correlated systems, mainly for semiconductors; *GW* is not suitable for describing Hubbard side bands, Mott-Hubbard metal-insulator transitions, transition metals oxides, or *f*-electron systems [6].

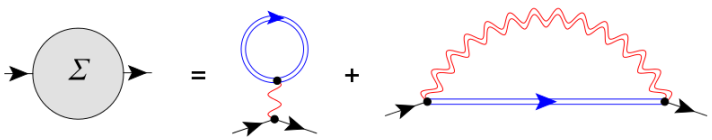

Figure 2-6: The self-energy, Σ, is given by the Hartree term and a Fock-like term, represented by the screened Coulomb interaction W (double wiggly line), instead of the bare Coulomb interaction, V (single wiggled line). The interacting Green's function, G, is represented by a double straight line (from Ref. [6]).

2.3.1 From Hedin's Equations to *GW*

The *GW* method is an approximation to the self-energy which attempts to account for the complicated correlation effects in a many-body system. The simplest approximation re-

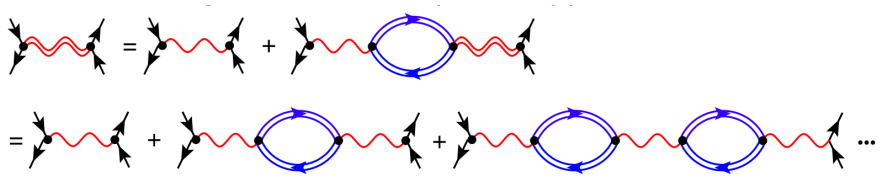

Figure 2-7: The screened Coulomb interaction W (double wiggly line) is calculated from the bare Coulomb interaction, V (single wiggled line) and corrections which describe the screening processes. The screening is calculated from the RPA. Only the bubble diagrams in a geometric series are considered (second line). The geometric series is generated from a single bubble connected to the screeened interaction (first line). Starting with $W = V$ (RHS of the first line), one generates the second term of the second line, and by further iterations one may obtain the whole series (from Ref. [6]).

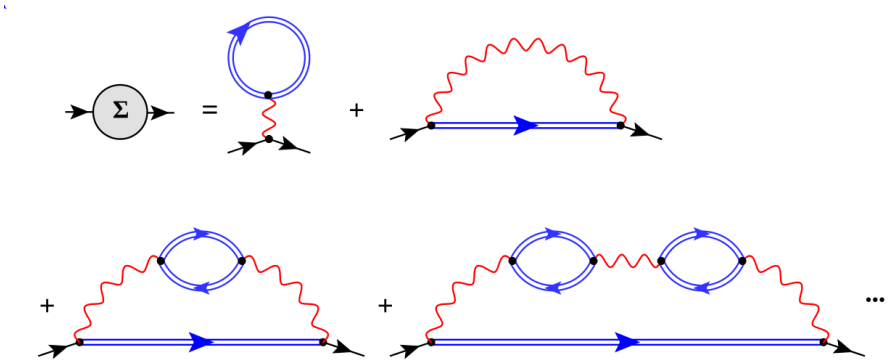

Figure 2-8: By replacing the screened interaction (Fig. 2-7) into the self-energy (Fig. 2-6), the Hartree and Fock terms are generated (first line), together with the electronic correlations that go beyond the Hartree-Fock term (second line) (from Ref. [6]).

sults from the expansion of Hedin's equations [67], which stem from five coupled equations: the Schwinger-Dyson equation, the screened interaction, the polarisation vector, the standard relations between irreducible and reducible vertex, and the self-energy [67, 6].

The formal way to represent the one-particle Green's function is by defining

$$G(12) \quad = \quad -i\langle T(\Psi(1)\Psi^{\dagger}(2))\rangle \tag{2.64}$$

where the script 1 and 2 represent the space-time coordinates, i.e. $1 = (\mathbf{r}_1, t_1)$. T is the Dyson time-ordering operator and Ψ is the field operator in the Heisenberg representation [67]. The averaging is done with respect to the exact ground state, rather than the noninteracting ground state of the system.

For a one-body Hamiltonian, H^0 has the form [52]

$$H^0 = -\frac{\nabla^2}{2m} + V^{\text{eff}}(\mathbf{r}_1, \mathbf{r}_2) \tag{2.65}$$

where V^{eff} is the effective potential. The potential is static and Hermitian and can be non-local, although if V^{eff} is generated by the Kohn-Sham relations it becomes local, such that $V^{\text{eff}}(\mathbf{r}_1, \mathbf{r}_2) = V^{\text{eff}}(\mathbf{r}_1)\delta(\mathbf{r}_1 - \mathbf{r}_2)$

The noninteracting Green's function, G^0, is then constructed from the eigenvalues, ε_s, and eigenfunctions, $\Psi_s(\mathbf{r})$, determined by H^0. From the definition of Eq. 2.64, G^0 is thus [7]:

$$G^0(\mathbf{r}_1, \mathbf{r}_2, \omega) = \sum_s \frac{\Psi_s(\mathbf{r}_1)\Psi_s^*(\mathbf{r}_2)}{\omega - \varepsilon_s} \tag{2.66}$$

where

$$\begin{aligned} \Psi_s(\mathbf{r}_1) &= \langle N, 0|\Psi(\mathbf{r}_1)|N+1, s\rangle \\ &\quad \varepsilon_s = E_{N+1,s} - E_{N,0} - i\delta \quad \text{when} \quad \varepsilon_s \geq \mu \end{aligned} \tag{2.67}$$

$$\begin{aligned} \Psi_s(\mathbf{r}_1) &= \langle N-1, s|\Psi(\mathbf{r}_1)|N, 0\rangle \\ &\quad \varepsilon_s = E_{N,0} - E_{N-1,s} + i\delta \quad \text{when} \quad \varepsilon_s < \mu \end{aligned} \tag{2.68}$$

where $\mu = E_{N+1,0} - E_{N,0}$ is the chemical potential (or the electron affinity, $-A$), $|N, 0\rangle$ is the ground-state determined by H^0 and the sum runs over all states of the $N+1$ and $N-1$ systems [67].

The self-energy is related to the Green's function through:

$$G(12) = G^0(12) + \int d[34]\, G^0(13)\Sigma(34)G(42) \tag{2.69}$$

with G and G^0 representing the interacting and non-interacting ($V = 0$) Green's functions, respectively. Eq. 2.69 describes the propagation of a particle from $(\mathbf{r}_2, t_2)$ to $(\mathbf{r}_1, t_1)$.

Based on Hedin's equation, the screened interaction, W, can be related to the polarisation operator, Π. In addition to the bare interaction, more complicated interactions involving additional electrons are also accounted for [6]. W is given by:

$$W(12) = \int [d3]\, \epsilon^{-1}(13)V(32) \tag{2.70}$$

[7] Fourier transformation allows one to change to a frequency-domain Green's function $G(\mathbf{r}_1, \mathbf{r}_2, \omega) = \int d(t_1 - t_2)\, G(\mathbf{r}_1 t_1, \mathbf{r}_2 t_2) \exp[i\omega(t_1 - t_2)]$

where ϵ is the dielectric function, which is the term related to Π as

$$\epsilon(13) = \delta(13) - \int d[4]\ V(14)\Pi(43) \tag{2.71}$$

with $\delta(13)$ coming from the definition of the inverse Green's function as [67]

$$\delta(13) = \int d[4]\ G(14)G^{-1}(43)$$

$W(12)$ gives the potential at point 1 due to the presence of a test charge at point 2, and includes the effect of the electron polarisation. Therefore W would represent the dynamically screened interaction between electrons in a general medium [67] and, can be re-written as:

$$W(12) = V(12) + \int [d34]\ V(13)\Pi(34)W(42) \tag{2.72}$$

The most basic approximation, is to remove the second term of the RHS of Eq. 2.72, and merely consider the bare Coulomb potential to obtain the self-energy: $\Sigma(12) = iG(12)V(12)$ (Hartree-Fock approximation).

The polarisation operator, Π, is the standard relation between two particle Green's functions (response functions), and forms another of Hedin's equations:

$$\Pi(12) = -i \int d[34]\ G(13)G(41)\Gamma(342) \tag{2.73}$$

with Γ being the vertex function, described by:

$$\Gamma(123) = \delta(12)\delta(13) + \int d[4567]\frac{\delta\Sigma(12)}{\delta G(45)}G(46)G(57)\Gamma(673) \tag{2.74}$$

in which the self-energy, Σ, is written as a functional derivative of the Green's function.

We finally arrive at the last of Hedin's equation, which defines the self-energy Σ:

$$\Sigma(12) = i \int d[34]G(13)W(14)\Gamma(423) \tag{2.75}$$

The simplest approximation is to neglect the vertex corrections of Eq. 2.74 [68], by removing the last term of the RHS. This results in rewriting Π as

$$\Pi(12) = -iG(12)G(21) \tag{2.76}$$

which is simply the RPA. Σ also changes to:

$$\Sigma(12) = -iG(12)W(12) \tag{2.77}$$

thus obtaining the GWA.

Since GW is an approximation to the exact theory, the one-body effective Hamiltonian, $H(\omega)$, determines the time evolution of the one-body amplitude for the many-body system and is written as:

$$H(\mathbf{r}_1, \mathbf{r}_2, \omega) = -\frac{\nabla^2}{2m} + V^{\text{ext}}(\mathbf{r}_1, \mathbf{r}_2) + V^{\text{H}}(\mathbf{r}_1, \mathbf{r}_2) + \Sigma(\mathbf{r}_1, \mathbf{r}_2, \omega) \tag{2.78}$$

with $H(\mathbf{r}_1, \mathbf{r}_2, \omega)$ being a functional of V^{eff} and V^{ext} the external potential from the nuclei. The Hartree potential, V^{H} is obtained from the electron density as [68, 7]:

$$V^{\text{H}}(\mathbf{r}_1, \mathbf{r}_2) = \int d\mathbf{r}_2 \; V(\mathbf{r}_1, \mathbf{r}_2) n(\mathbf{r}_2) \tag{2.79}$$

with n being the electron density.

By summing up the potential terms we obtain the ω-dependent one-body effective potential:

$$V^{\text{GW}}(\mathbf{r}_1, \mathbf{r}_2, \omega) = V^{\text{ext}}(\mathbf{r}_1, \mathbf{r}_2) + V^{\text{H}}(\mathbf{r}_1, \mathbf{r}_2) + \Sigma(\mathbf{r}_1, \mathbf{r}_2, \omega) \tag{2.80}$$

Thus, one obtains a perturbative correction to the one-particle potential, $V^{\text{eff}}(\mathbf{r}_1)$ [69]:

$$\Delta V(\mathbf{r}_1, \mathbf{r}_2, \omega) = V^{\text{GW}}(\mathbf{r}_1, \mathbf{r}_2, \omega) - V^{\text{eff}}(\mathbf{r}_1) \tag{2.81}$$

In the one-shot GW, H^0 is typically generated by LDA-DFT, and hence $V^{\text{eff}}(\mathbf{r}_1)$ is the Kohn-Sham Hamiltonian. Considering only the diagonal terms, the quasiparticle (QP) energy is: [69]

$$E_{\mathbf{k}n} \quad = \quad \varepsilon_{\mathbf{k}n} + Z_{\mathbf{k}n}[\langle \Psi_{\mathbf{k}n} | \Sigma(\mathbf{r}_1, \mathbf{r}_2, \varepsilon_{\mathbf{k}n}) | \Psi_{\mathbf{k}n} \rangle] - [\langle \Psi_{\mathbf{k}n} | V_{\text{xc}}^{\text{LDA}}(\mathbf{r}_1) | \Psi_{\mathbf{k}n} \rangle] \tag{2.82}$$

with $\mathbf{k}$ being the wave-vector and n the band index. $Z_{\mathbf{k}n}$ is the QP renormalization factor, and for simplicity this value is taken to be unity [69].

2.3.2 Quasiparticle Self-Consistent *GW*

Quasiparticle self-consistent *GW* (QSGW) is an *ab-initio* method that determines the non-interacting Hamiltonian in a self-consistent manner and does not depend on LDA-DFT.

In QSGW it is more complicated to calculate the QP energies, since the off-diagonal terms of Eq. 2.82 are required [69]. Based on Landau's QP picture, there are fundamental one-particle like excitations around the Fermi energy, E_{F}, which are characterised by *dressed* QPs.

The QP energies, $E_{\rm s}$, and eigenfunctions, $\Phi_{\rm s}(\mathbf{r}_1)$, are of the form

$$\left[\frac{-\nabla^2}{2m} + V^{\rm ext} + V^{\rm H} + {\rm Re}[\Sigma(E_s)] - E_s\right]|\Phi_s\rangle = 0 \tag{2.83}$$

where only the real part of the self-energy is considered [69]. Within the one-particle picture described by H^0, the QP energies, ε_s, and eigenfunctions, Ψ_s, are *bare* QPs. The bare QPs interact with each other *via* the bare Coulomb interaction and evolve into the dressed QPs when the interaction $\hat{H} - \hat{H}^0$ is turned on adiabatically. $\hat{H}$ is the total Hamiltonian, written as a sum of three terms:

$$\hat{H} = \hat{H}^k + \hat{V}^{\rm ee} + \hat{V}^{\rm ext} \tag{2.84}$$

with

$$\hat{H}^k = \sum_\sigma \int d\mathbf{r}_1 \; \hat{\psi}^\dagger_\sigma(\mathbf{r}_1)\left(-\frac{\nabla^2}{2m}\right)\hat{\psi}_\sigma(\mathbf{r}_1), \tag{2.85}$$

$$\hat{V}^{\rm ee} = \frac{1}{2}\sum_{\sigma\sigma'}\int d\mathbf{r}_1 d\mathbf{r}_2 \; \upsilon(\mathbf{r}_1,\mathbf{r}_2)\hat{\psi}^\dagger_\sigma(\mathbf{r}_1)\hat{\psi}^\dagger_{\sigma'}(\mathbf{r}_2)\hat{\psi}_{\sigma'}(\mathbf{r}_2)\hat{\psi}_\sigma(\mathbf{r}_1), \tag{2.86}$$

$$\hat{V}^{\rm ext} = \sum_\sigma \int d\mathbf{r}_1 \; \hat{V}^{\rm ext}_\sigma(\mathbf{r}_1)\hat{n}_\sigma(\mathbf{r}_1) \tag{2.87}$$

where $\hat{\psi}_{\sigma'}(\mathbf{r}_1)$ are the field operators, σ the spin index and $\hat{V}^{\rm ext}_\sigma(\mathbf{r}_1)$ is the external potential.

Similar to the GWA, the dressed QPs consist of the central bare QP and an induced polarisation cloud of other bare QPs.

In order to determine the optimal H^0, the effective potential, $V^{\rm eff}$, has to be chosen based on a self-consistent perturbation theory, where the time evolution determined by H^0 is as close as possible to that of $H(\omega)$ [7]. By introducing a norm M to measure the difference $\Delta V(\omega) = H(\omega) - H^0$, the optimum $V^{\rm eff}$ will thus be a potential which minimises M. An exact minimization of the norm is not possible and therefore approximate solutions have to be found. A trivial minimum can be found at $V^{\rm eff} = V^{\rm ext} + V^{\rm H} + V^{\rm xc}$, where $V^{\rm xc} = \sum_{ij}|\psi_i\rangle\sum(\varepsilon_j)_{ij}\langle\psi_j|$, $\sum(\varepsilon_j)_{ij} = \langle\psi_i|\sum(\varepsilon_i)|\psi_j\rangle$, and ψ and ε are the eigenfunctions and eigenvectors of H^0, respectively [7]. The averaging of the hermitian parts results in:

$$V^{\rm xc} = \frac{1}{2}\sum_{ij}|\psi_i\rangle\left\{{\rm Re}\left[\sum(\varepsilon_i)\right]_{ij} + {\rm Re}\left[\sum(\varepsilon_j)\right]_{ij}\right\}\langle\psi_j|. \tag{2.88}$$

The total energy is then calculated based on the adiabatic connection formalism [69], where the one-body Hamiltonian, H^0, evolves into the total Hamiltonian, $\hat{H}$, of Eq. 2.84. A smooth path of adiabatic connection can thus be parametrised by defining λ, which is set from $\lambda = 0$ to $\lambda = 1$, corresponding to the bare QP to the dressed QP, respectivly [69].

2.3.3 Band-Gaps and Quasiparticles

Most computationally affordable GW calculations employ the LDA eigenfunctions, as the starting point, to generate the self-energy $\Sigma \approx iG_0W_0$: from the LDA polarisation (or dielectric constant) one obtains the screened interaction W_0 which in turn is used to determine the self-energy with the Green function G_0 [6].

When employing G_0W_0, it has been demonstrated that the fundamental band-gaps in sp^3 covalent materials show an improvement over LDA [70]. Inspite this, the one-shot GW band-gaps are still underestimated, when compared to experimental, even for weakly correlated semiconductors [7] (Fig. 2-9). One-shot GW approaches are rather unsatisfactory, since the QP levels are closely related to the quality of the ground-state wave-functions (DFT exchange-correlation functional).

By applying a self-consistent calculation for the self-energy (Hedin's equation), and by constructing the screened interaction W within the random-phase approximation [71], it has been observed that the QP band-width of the homogeneous electron gas is increased in weight when compared with non-self-consistent calculations [71]. This feature is also observed for calculations with partial self-consistency using a fixed W [71]. Since results based on self-consistent calculations also present inaccuracies when compared to experimental evidences, suggestions are therefore drawn that non-self-consistent results are to be preferred, unless vertex corrections are included [71].

Since QSGW applies an Hamiltonian that is found by optimisation (minimising the perturbation to H^0) it is expected that calculations will predict more reliable ground- and excited-states properties for a large number of weakly and moderately correlated materials [7]. Calculations result in reliable QP levels for a wide range of materials: not only in the description of the fundamental gaps in semiconductors but also for the majority of the energy levels. Even in strongly correlated d- and f-electron systems, errors are somewhat larger than experimental evidences, but these are still systematic [8].

Although the increase of accuracy of QSGW, this method tends to slightly overestimate semiconductor band-gaps and underestimate dielectric constants [69]. The reason for this is because W does not include electron-hole correlation within RPA; the inclusion of the correlation energy would effectively reduce the pair excitation energy in its intermediate states [69], which can be accounted for *via* vertex corrections in W [8] (Fig. 2-10).

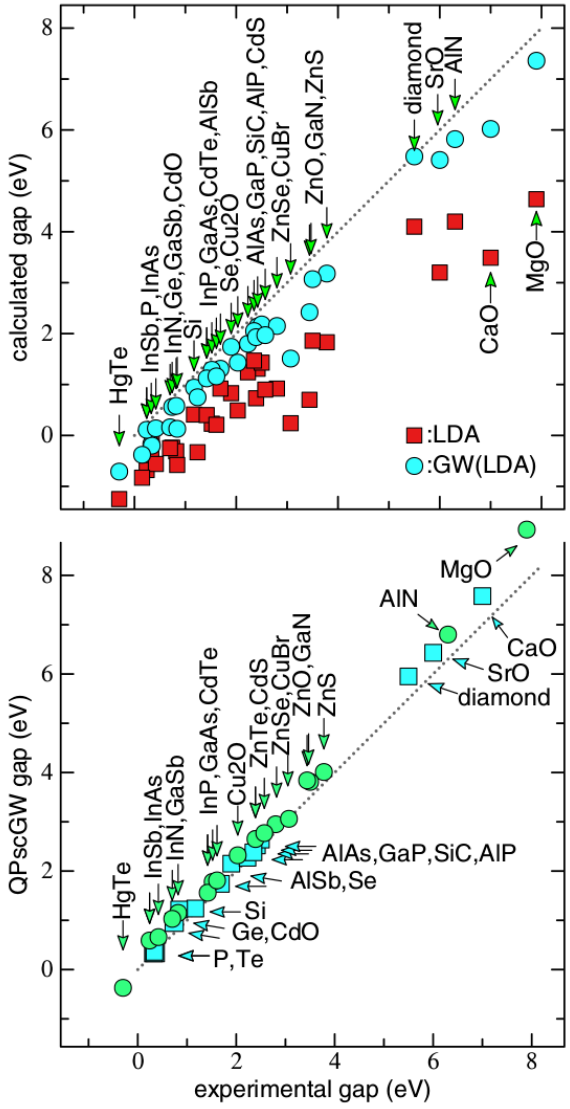

Figure 2-9: Fundamental gaps of *sp* compounds from LDA (squares) and the one-shot approximation (G_0W_0) (circles) (top panel), and from $QSGW$ (bottom panel). The G_0W_0 gaps improve over the LDA, but these are still underestimated (from Ref. [7]).

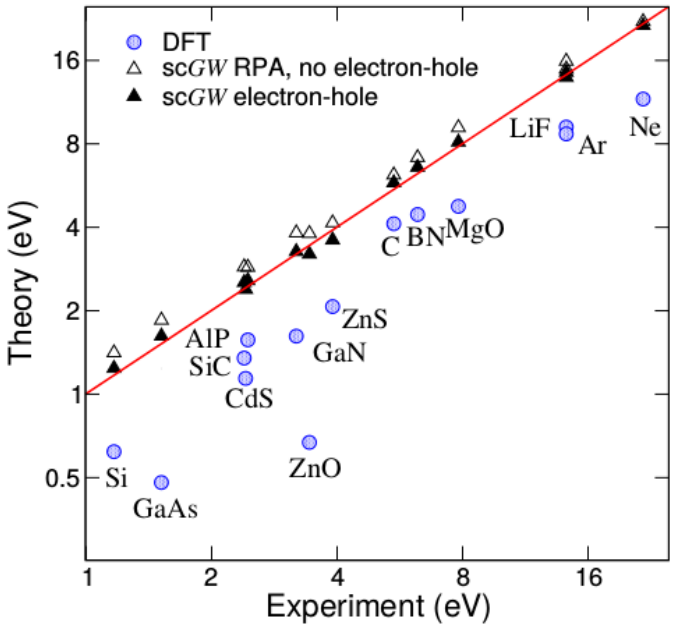

Figure 2-10: Theoretical and experimental band-gaps of several compounds. Theoretical results are provided by calculations from DFT, self-consistent GW (scGW) within RPA and, by including vertex corrections (electron-hole ladder diagrams, represented with filled triangles) (from Refs. [6] and [8]).

2.4 Lattice Dynamics

Materials modelling generally focuses on systems in thermodynamic equilibrium; however, when systems are perturbed by external stimuli, such as temperature, interesting phenomena tend to occur, e.g. phase transitions. For the majority of materials the main origin of entropy is due to thermal vibration, and these cannot be accounted for if dynamics is neglected: if the thermodynamic temperature is zero, entropy is effectively neglected. The study of the temperature dependence of the properties of materials requires accounting for nuclear motion, because the nuclei vibrate around their equilibrium positions, and the dynamic and thermodynamic properties of solids will therefore depend upon the lattice vibrations.

2.4.1 The Harmonic Approximation

The normal modes of vibration in a solid can be thought of as particle-like and are known as phonons. The energy of a phonon is given by the product of the quantum of action, the Planck's constant, $\hbar$, and the angular frequency, ω. Due to fluctuations in the ground state characteristic of the harmonic oscillator, the zero-point energy of a phonon mode is [72]:

$$E_0 = \frac{1}{2}\hbar\omega \tag{2.89}$$

which corresponds to motions at $T = 0$ K known as zero-point vibrations. The mean energy of each vibrational mode, ν, with wave-vector, $\mathbf{q}$, is given by:

$$E(q) = \hbar\omega(q)\left[\frac{1}{2} + n(q)\right] \tag{2.90}$$

where $q = (\mathbf{q}, \nu)$, $n(q)$ is the phonon occupation number for each mode obtained from the Bose-Einstein distribution with characteristic oscillator frequency ω. The phonon ocupation number can be related to temperature, T, by:

$$n(q) = n(\omega, T) = \left[\frac{1}{\exp\left(\hbar\omega(q)/k_{\mathrm{B}}T\right) - 1}\right] \tag{2.91}$$

where k_{B} is Boltzmann's constant.

The thermodynamic properties of a solid are directly related to its phonon structure. The entire set of phonons described by the phonon dispersion relations define the phonon density of states, which determines the heat capacity of the crystal.

Considering a phonon, with wave-vector $\mathbf{q}$ and band index ν (with $q = (\mathbf{q}, \nu)$), the dis-

placement of any atom j with mass m in the unit-cell l will be given by:

$$\mathbf{u}(jl) = \frac{1}{\sqrt{Nm_j}} \sum_q \mathbf{e}(jq) \exp\left[i\mathbf{q} \cdot \mathbf{r}(jl)\right] Q(q) \tag{2.92}$$

where $\mathbf{r}$ is the atom position, N is the number of unit-cells, $\mathbf{e}(q)$ is the mode eigenvector (also known as the displacement vector or polarisation vector) which gives the direction of the movement of the atom; and $Q(q)$ is the normal mode coordinate, which gives the amplitude and the time dependence.

The vibrational modes are called the normal modes of the system, and these are given by travelling waves with a characteristic frequency. From Eq. 2.92, one obtains [73]:

$$Q(q) = \frac{1}{\sqrt{N}} \sum_{j,l} \sqrt{m_j} \exp\left[-i\mathbf{q} \cdot \mathbf{r}(jl)\right] \mathbf{e}^*(jq) \cdot \mathbf{u}(jl) \tag{2.93}$$

where each normal mode follows the orthogonality relation:

$$\sum_j \mathbf{e}(j, \mathbf{q}, \nu) \cdot \mathbf{e}(j, -\mathbf{q}, \nu') = \delta_{\nu,\nu'} \tag{2.94}$$

By considering the potential energy of phonon system, as a function of the atomic positions, $V[\mathbf{u}(j_1, l_1), \cdots \mathbf{u}(j_n, l_n)]$ [73], and since the atoms vibrate around their equilibrium position, determined by the minimum of the energy surface, the potential energy can be Taylor-expanded as a function of the atomic displacements from equilibrium [74]:

$$\begin{aligned} \phi = V_0 \quad &+ \quad \frac{1}{2} \sum_{\substack{j\,,j' \\ l\,,l'}} \frac{\partial^2 V}{\partial \mathbf{u}_{j,l} \partial \mathbf{u}_{j',l'}} \mathbf{u}_{j,l} \mathbf{u}_{j',l'} + \cdots \\ &+ \quad \frac{1}{n!} \sum_{\substack{j,\cdots,j^{(n)} \\ l,\cdots,l^{(n)}}} \frac{\partial^n V}{\partial \mathbf{u}_{j,l} \cdots \partial \mathbf{u}_{j^{(n)},l^{(n)}}} \mathbf{u}_{j,l} \cdots \mathbf{u}_{j^{(n)},l^{(n)}} \end{aligned} \tag{2.95}$$

where V_0 is the potential energy with all atoms at rest. There is no first-order term in the expansion because by definition at equilibrium the residual forces are zero.

The simplest model to study lattice dynamics is the harmonic approximation (HA) in which the Taylor-expansion of the potential (Eq. 2.95) is truncated to second order. The successive terms in the series expansion of the crystal potential energy (higher order terms) are the anharmonic terms, from which one can obtain the physical effects of anharmonicity such as thermal expansion, changes in normal mode frequencies with temperature, and thermal resistivity [72].

The assumption of the harmonic approximation is that atomic displacements have to be small so that energy can be described as a harmonic function of the relative displacements of the neighbouring atoms.

The harmonic phonon energy can be re-written in terms of Eqs. 2.90 and 2.91 as [75, 13]:

$$E(q) = \sum_q \hbar\omega(q) \left[\frac{1}{2} + \frac{1}{\exp\left(\hbar\omega(q)/k_\mathrm{B}T\right) - 1}\right] \tag{2.96}$$

The constant-volume heat capacity can be obtained through the relation:

$$\begin{aligned} C_V &= \left(\frac{\partial E}{\partial T}\right)_V = \sum_q \hbar\omega(q) \left[\frac{\partial n(\omega, T)}{\partial T}\right] \\ &= \sum_q k_\mathrm{B} \left[\frac{\hbar\omega(q)}{k_\mathrm{B}T}\right]^2 \frac{\exp\left(\hbar\omega/k_\mathrm{B}T\right)}{\left[\exp\left(\hbar\omega\right)/k_\mathrm{B}T) - 1\right]^2} \end{aligned} \tag{2.97}$$

The Helmoltz free energy, F, can be defined in terms of the canonical partition function, Z, by [75]:

$$F = -k_\mathrm{B}T \ln Z \tag{2.98}$$

where Z defines the partitioning of energy among the energy levels associated with the degrees of freedom of the system [76, 13, 77], and for a crystal is given by:

$$Z(T) = \exp\left(-\phi/k_\mathrm{B}T\right) \prod_q \frac{\exp\left[-\hbar\omega(q)/2k_\mathrm{B}T\right]}{1 - \exp\left[-\hbar\omega(q)/k_\mathrm{B}T\right]} \tag{2.99}$$

where ϕ is the potential energy of the crystal, and the product runs over vibrational modes ν and reciprocal-space wave-vectors $\mathbf{q}$ [78, 13, 77].

The temperature-dependent Helmoltz free energy is hence given by [79, 75, 13, 77]:

$$F(T) = \phi + \frac{1}{2}\sum_q \hbar\omega(q) + k_\mathrm{B}T \sum_q \ln\left[1 - \exp\left[-\hbar\omega(q/k_\mathrm{B}T)\right]\right] \tag{2.100}$$

The second term is a sum of the modal contributions to the zero-point vibrational energy, and the third term is the contribution of each mode to the internal energy due to thermal occupation of the phonon energy levels.

The entropy is readily obtained by defining:

$$S(T) = -\left(\frac{\partial F}{\partial T}\right)_V = -k_{\rm B}\sum_q \ln\left[1-\exp\left[-\hbar\omega(q/k_{\rm B}T)\right]\right] - \frac{1}{T}\sum_q \hbar\omega(q)n(\omega,T) \quad (2.101)$$

The thermal properties of solids at constant volume can be evaluated from their phonon density of states, $g(\omega)$, which counts the number of modes with angular frequencies between ω and $\omega + d\omega$. The harmonic phonon energy can thus be written in the form:

$$E = \int \hbar\omega g(\omega)\Big[\frac{1}{2} + n(\omega,T)\Big]d\omega \quad (2.102)$$

Phonon frequencies are derived from the restoring force in response to the displacement of ions by a small amplitude from their equilibrium positions. The interatomic force constants (IFCs) can either be computed from the linear response method (e.g. density-functional perturbation theory, DFPT), or the direct method. The former considers that the force constant matrix (or dynamical matrix) is computed in terms of the inverse dielectric matrix describing the response of the valence electron density to a periodic lattice perturbation [80]. The direct method (or finite-displacement method) consists of employing the forces calculated via the Hellmann-Feynman theorem in the total energy calculations, to derive the force constant matrices. The Parlinski-Li-Kawazoe supercell approach is commonly employed [80, 81] and the method manages to capture the long-range contributions to the IFCs between atoms in different crystallographic unit-cells, which are needed to accurately calculate the frequencies of short-wavelength phonon modes [78]. In practice one has to perform force calculations on a series of symmetry-inequivalent displaced structures and fit the force/displacement curves to a harmonic function. A force on an atom is the first derivative of the potential energy with respect to an atomic position

$$F_{j,l} = \frac{\partial V}{\partial \mathbf{u}_{j,l}} \quad (2.103)$$

and the second-order force constant is hence

$$\phi_{j,l;j',l'} = \frac{\partial^2 V}{\partial \mathbf{u}_{j,l}\partial \mathbf{u}_{j',l'}} \quad (2.104)$$

In the finite displacement method the force constant equation is approximated as [81]

$$\phi_{j,l;j',l'} \simeq -\frac{F_{j',l';\Delta\mathbf{u}_{j,l}} - F_{j',l'}}{\Delta\mathbf{u}_{j,l}} \quad (2.105)$$

where $F_{j',l';\Delta\mathbf{u}_{j,l}}$ are the forces of the atoms displaced by $\Delta\mathbf{u}_{j,l}$.

2.4.2 The Quasi-Harmonic Approximation

In the harmonic model, the equilibrium positions are independent of temperature. The anharmonic effects needed to account for thermal expansion can be introduced by the quasi-harmonic approximation (QHA), in which the thermal expansion of the crystal lattice is obtained from the volume dependence of the phonon frequencies. The evaluation of the equilibrium volume and Gibbs free energy at a temperature T is obtained by minimising the function $G(T,p)$ for a given (constant) pressure p [76, 79]:

$$G(T,p) = \min_V \left[\phi(V) + F(V,T) + pV\right] \tag{2.106}$$

where $\min_V$ means that for each value of T and p, the function is minimized with respect to the volume.

The heat capacity at constant-pressure is then derived from $G(T,p)$ by:

$$\begin{aligned} C_p(T,p) &= -T\left[\frac{\partial^2 G(T,p)}{\partial T^2}\right]_P \\ &= C_V + T\left[\frac{\partial V(T,p)}{\partial T}\right]_p \left[\frac{\partial S(T,V)}{\partial V}\right]_T \end{aligned} \tag{2.107}$$

with $V(T,p)$ being the equilibrium volume at T and p [79, 13].

To perform a QHA calculation, the phonon frequencies are computed for a range of expansions and compressions about the equilibrium volume (which corresponds to T=0 K). All the new expanded and compressed volumes are relaxed (ion relaxation without allowing change of the cell shape) and the free energies are then computed for all these volumes. From this approach, the equilibrium volume, bulk modulus and Gibbs free energy can thus be obtained at arbitrary temperatures by fitting the free energies as a function of volume to an equation of state [82, 83]. The temperature effect is thus included into the total energy of electronic structure through the Helmholtz free energy at constant volume. By increasing temperature, the volume dependence of the free energy changes, hence the equilibrium volume for diferent temperature values also changes. The temperature dependence of various derived properties, e.g. volumetric expansion coefficients and the mean Grüneisen parameter, are then readily obtained.

The mode Grüneisen paramaters, $\gamma(q)$, quantify the change in each phonon frequency with

volume V through [84, 73]:

$$\gamma(q) \quad = \quad -\frac{V}{\omega(q)}\frac{\partial\omega(q)}{\partial V} = -\frac{\partial \ln \omega(q)}{\partial \ln V} \tag{2.108}$$

These are related to the temperature-dependent mean Grüneisen parameter by:

$$\gamma \quad = \quad \sum_q \frac{C(q)\gamma(q)}{C_{\mathrm{V}}} \tag{2.109}$$

where C_{V} is the constant-volume heat capacity at volume V, and $C(q)$ are the contributions from individual modes:

$$C(q) \quad = \quad \hbar\omega(q)\frac{\partial n(T,\omega(q))}{\partial T}. \tag{2.110}$$

Within the QHA, the mean Grüneisen parameter is related to the volumetric thermal expansion coefficient, α_{V}, according to:

$$\alpha_{\mathrm{V}} \quad = \quad \frac{\partial \ln V}{\partial T} = \frac{1}{BV}\sum_q C(q)\gamma(q) \tag{2.111}$$

where B is the (temperature-dependent) bulk modulus.

When the mean Grüneisen parameter, γ, is negative, α_{V} will likewise be negative, indicating negative thermal expansion (NTE), i.e. a reduction in volume upon heating [84, 85, 86]. NTE behaviour in bulk systems has been linked to a number of microscopic mechanisms, including, among others, ferroelectric, magnetostrictive and displacive phase transitions, low-frequency phonon modes and rigid-unit modes [85].

2.4.3 Soft-Mode Theory

The energy associated with the lattice vibrations of a crystal is expressed in terms of an Hamiltonian written as a series expansion of the crystal energy in normal mode coordinates, Q [72] [8]:

$$\begin{aligned}\mathcal{H} \quad &= \quad \frac{1}{2}\sum_q \dot{Q}(q)\dot{Q}(-q) + \frac{1}{2}\sum_q \omega(q)^2 Q(q)Q(-q) + \frac{1}{4}\sum_q\sum_{q'}\alpha(q,q')\eta^2 Q(q)Q(-q) \\ &= \quad \frac{1}{2}\sum_q \dot{Q}(q)\dot{Q}(-q) + \frac{1}{2}\sum_q \left[\omega(q)^2 + \frac{1}{2}\sum_{q'}\alpha(q,q')\eta^2\right] Q(q)Q(-q)\end{aligned} \tag{2.112}$$

[8] It is possible to write the Hamiltonian in quantised form by replacing the normal mode coordinates, Q and $\dot{Q}$, by appropriate operators, $\hat{Q}$ and $\hat{P}$, respectively [72].

The first term of Eq. 2.112 refers to the kinetic energy. The second term is the normal harmonic energy, where ω is the harmonic frequency, which denotes all vibrational modes ν with vector $\mathbf{q}$, with the exception of the soft-mode. The third term refers to the anharmonic interaction, which is the fourth-order term of the series expansion (in practice it is the dominant term within the soft-mode theory and therefore will be the only anharmonic term considered) [9]. The coefficient α refers to the anharmonic coupling of the order parameter which measures the degree of order of a phase transition and thus characterises the transition, η, with any mode in the crystal [9], including the soft-mode denoted by q'.

The time derivative of Q, which defines the kinetic energy term of Eq. 2.112, has the form of:

$$\dot{Q}(q) = -i\omega(q)Q(q) \tag{2.113}$$

For an atom in a unit-cell, there are $3N$ branches in the dispersion (N is the number of atoms contained in the unit-cell), corresponding to $3N$ modes of motion. At small wave-vectors ($\mathbf{q} \to 0$) there are three modes, where all atoms move in phase and are termed the acoustic modes. The remaining modes are optical, and are characterised by atoms moving out of phase, and their frequencies are non-zero at $\mathbf{q} \to 0$ [72].

When a static distortion occurs, the frequencies are modified as [9, 72]:

$$\tilde{\omega}(q)^2 = \omega(q)^2 + \frac{1}{2}\sum_{q'} \alpha(q, q')\eta^2 \tag{2.114}$$

where $\tilde{\omega}$ is the frequency taking account both of the harmonic and anharmonic interactions.

The temperature dependence of the order parameter can be defined through thermal averaging as:

$$\eta^2 = \langle Q(q')Q(-q')\rangle$$

for which, and by obeying the conservation of crystal momentum, it is required that $\langle Q(q')Q(-q')\rangle \neq 0$ if $q' = -q$. The thermal average maybe given by the relation [9]:

$$\langle Q(q)Q(-q)\rangle = \frac{\hbar}{\tilde{\omega}(q')}\left[\frac{1}{2} + n(\tilde{\omega}_{q'}, T)\right] \approx \frac{k_{\mathrm{B}}T}{\tilde{\omega}(q')^2} \qquad \text{when} \qquad k_{\mathrm{B}}T \geq \hbar\tilde{\omega}(q') \tag{2.115}$$

In the high-temperature limit Eq. 2.114 can therefore be written as [9]:

$$\tilde{\omega}(q)^2 \quad = \quad \omega(q)^2 + \frac{k_{\mathrm{B}}T}{2}\sum_{q'} \frac{\alpha(q, q')}{\tilde{\omega}(q')^2} \tag{2.116}$$

Eq. 2.116 defines the relation of a set frequencies $\tilde{\omega}(q)^2$ called the renormalised phonon frequencies, which have an explicit temperature dependence [9].

By performing lattice dynamics calculations on a high-temperature phase, at least one imaginary harmonic frequency [9] will be evidenced. The imaginary frequency is expressed as a normal mode coordinate, in which the harmonic term of $\tilde{\omega}(q)^2 Q(q)Q(-q)$ must have a maximum energy when Q has a value of zero. This is only possible if $\omega^2(q) < 0$, meaning that $\tilde{\omega}(q)$ is imaginary [9]. The potential energy of the high-temperature phase is at the maximum with respect to the distortion mode that accompanies the phase transition [72] and which characterises a specific atomic displacement [72, 9].

A stable phase exists at lower temperatures and will correspond to a lower symmetry distorted structure. When the temperature is increased, the high-symmetry structure stabilises, and therefore the corresponding mode will increase in value and become positive (real). The temperature at which the mode reaches zero is the transition temperature (T_c) [9]. The value of the frequency will be determined by the restoring forces in response to a set of atomic displacements about their equilibrium positions.

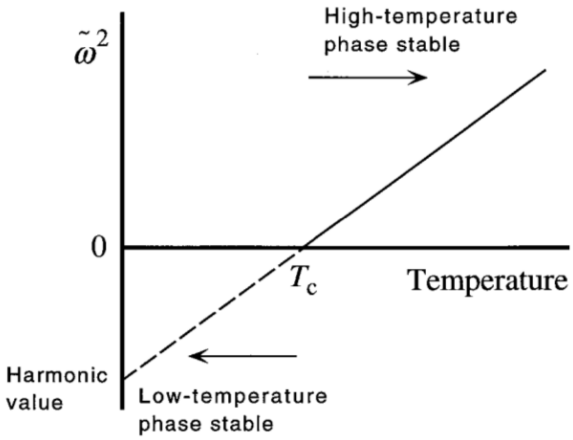

Figure 2-11: Representation of the behaviour of the soft mode. At low temperatures ($T \leq T_c$) the soft mode is unstable, which is represented by $\tilde{\omega}$. Thus the structure of the high-temperature phase is unstable. On heating, the anharmonic interactions contribute positively to the value of $\tilde{\omega}$, until the frequency reaches zero at the transition temperature (T_c). Above this temperature the soft-mode frequency has a real value, and thus the high-temperature phase is stable (from Ref. [9]).

If the transition involves small symmetry-breaking displacements, this transition is considered to be of displacive nature, and occurs when temperature or pressure is applied to the system [72]. Taking as an example, the perovskite structure, in its high-symmetry phase (usually cubic in symmetry) the small displacements are produced by rotations of the octahedral

cages around the cation. The symmetry of the lattice will thus be lowered and there will be a change in the description of the volume of the unit-cell.

Ferroelectric transitions occur when the system undergoes the breaking of the centre-of-symmetry, giving rise to a net dipole moment in the unit-cell, thus producing a macroscopic dielectric polarisation of the crystal [73]. The idea of soft-mode in a ferroelectric phase-transition is implicit in the relation between the longitudinal optic (LO) and transverse optic (TO) modes at the zone-centre of ionic structures since the long-range fields at $\mathbf{q} \to 0$ are not equivalent. This relation is known as the Lyddane-Sachs-Teller (LST) relation and relates the limiting values of the LO and TO frequencies to the dielectric constants for oscillating electric fields of zero (static) and infinite (high) frequencies through the ratio:

$$\frac{\epsilon(\omega = 0)}{\epsilon(\omega = \infty)} = \frac{\omega_{LO}^2}{\omega_{TO}^2} \tag{2.117}$$

Since a ferroelectric phase transition is characterised by presenting a divergence of the static dielectric constant, at the phase transition, the LST relation implies that $\omega_{TO}^2 \to 0$ (softening of the TO mode at $\mathbf{q} \to 0$).

Other types of phase transitions exist, which involve soft-modes with wave-vectors at the Brillouin zone boundaries: zone-boundary (antiferroelectric) phase transitions. In these cases the soft-modes can either be acoustic or optic. A zone boundary phase transition implies that the unit-cell of the low-temperature phase is doubled in one or more directions. Examples exist where the neighbouring unit-cells of the high-temperature phase develop dipole moments, but since these are in opposite directions, the unit-cell at low temperature has no net moment [72].

The soft-modes considered in ferroeleastic phase transitions involve the softening of an acoustic mode. Although, and since at $\mathbf{q} = 0$ the frequency is already zero, the softening involves the slope of the acoustic mode falling to zero, which corresponds to a softening of the elastic constants. The gradient of the soft acoustic mode as $\mathbf{q} \to 0$ gives the velocity of sound, square of which provides information regarding one of the elastic constants [72].

2.5 Macroscopic Polarisation for Ferroelectric Phase Transitions

Macroscopic polarisation is a vector quantity that quantifies the electric dipole moment per unit vector. Spontaneous macroscopic polarisation is when a finite polarisation persists even in the absence of an external perturbation and defines the equilibrium properties of a ferroelectric material [87].

Ferroelectric materials are insulting solids that at equilibrium display a broken-symmetry (non-centrosymmetric) structure [10, 88]. Long-range electrostatic forces favour a polar struc-

ture, and therefore tend to drive polar instabilities. However, it has recently been suggested that metals can also show spontaneous polarisation due to certain local bonding preferences which persist even in the presence of screening by charge carriers [89].

If the centre-of-symmetry is broken, the crystal may have one or more polar axes. Crystals with a unique polar axis[9] are ferroelectric and possess spontaneous electric polarisation. Crystals with more than one polar axis, are piezoelectric, and manifest an electric polarisation in response to the application of elastic stress [10, 88].

The surface of a ferroelectric crystal attracts free charges from its environment to neutralise the effective surface charge resulting from the polarisation discontinuity. Screening effects are pronounced in ultra-thin ferroelectric films, where the internal electric fields generated by the ferroelectric dipoles are sufficiently large to produce electronic and ionic currents.

There are different groups of ferroelectric material, among which are proper and improper, hyperferroelectrics and Ferroelectric Rashba Semi-Conductors (FERSC). These classifications are mostly based on symmetry rules, on the dynamics of the phase transition from the high-temperature centrosymmetric to lower-temperature polar phase, and on the characterisation of the soft-mode instabilities.

1. A proper-ferroelectric (conventional ferroelectric) is characterised by a reference, non-polar, structure; due to a polar distortion, the symmetry is lowered to a polarised ground-state phase. From a microscopic point-of-view, the reason for this structural instability is due to the existence of unstable optic modes (imaginary modes) at the zone-center of the BZ (Γ-$\mathbf{q}$ point) [90, 91, 92], more specifically unstable transverse optic modes. Since in very thin films (> 10 nm) there are very large depolarisation fields due to the surface charge accumulation, strong electric fields may counteract the polar displacements, with the possibility that these depolarisation fields may suppress completely the ferroelectric distortion. Examples of proper-ferroelectrics are conventional perovskite materials, such as $PbTiO_3$ and $BaTiO_3$.

2. Improper-ferroelectrics do not have an unstable polar distortion in their high-symmetry structure; instead, these may have one or more unstable non-polar distortions [91]. Since the primary distortion is non-polar, the depolarisation field is too weak and therefore thin films do not experience the same problems as in proper-ferroelectrics; respective slabs may develop a finite polarisation normal to the surface [91]. While for a proper-ferroelectric the polar distortion acts as the primary order-parameter in the phase transition, for improper-ferroelectrics the polarisation emerges due to another, non-polar, order parameter of different physical origin. Depending on the material these can be the rotation/tilts of the perovskite cages, magnetic ordering, etc. The polarisation develops

[9] A polar axis is defined by the orientation of the dipole moment.

as a by-product of some other complex lattice distortion.

3. A hyperferroelectric has the ability to spontaneously polarise even in the presence of an unscreened depolarisation field, which gives these materials an advantage over proper-ferroelectrics, since they are less sensitive to surface and low-dimensional confinement effects. This feature arises not only because of the instability of the TO mode (similar to the one in proper-ferroelectrics), but also due to an additional instability of a longitudinal optic (LO) mode [92]. Unlike insulating ferroelectrics, which possess a wide energy band-gap, large Born-effective charges and small dielectric constants, hyperferroelectics exhibit low effective charges and large dielectric constants, as a consequence of a small gap [92].

4. FERSC materials evidence the combined properties of directed polarisation (ferroelectricity) and spin-orbit coupling (SOC) effects. These effects can be evidenced in small band-gap materials, such as chalcogenides (the most well knwon FERSC is GeTe). The advantage of FERSC materials is the possibility of controlling the spin-texture via a switchable electric bias, instead of magnetic fields, as a potential alternative to spintronic devices [17].

The changes in polarisation are rigorously defined and can be calculated through *ab initio* electronic structure methods [93] through the evaluation of the Berry phase expressions of the *Modern theory of polarization* [94]. Macroscopic polarisation is an experimentally measurable observable [93]. A typical measurement can be performed through polarisation reversal, where a hysteresis cycle can be traced which corresponds to the integrated macroscopic current flowing through the sample [87]. Therefore changes in polarisation are quantities that can be directly measured and calculated [95].

2.5.1 The Berry Phase Expressions

Within the independent-particle approximation, all physical quantities can be calculated through integration over filled electronic bands in the BZ, by taking advantage of the periodicity of $\mathbf{k}$ space. The change in polarisation can be found when a parameter of the Hamiltonian λ, i.e. potential, changes adiabatically with time [95].

From the definition that a change in polarisation can be determined from the polarisation current that flows through the bulk, the macroscopic current density, $\mathbf{j}$, we have [87]

$$\frac{d\mathbf{P}(t)}{dt} = \mathbf{j}(t) \tag{2.118}$$

therefore implying

$$\Delta\mathbf{P} = \mathbf{P}(\Delta t) - \mathbf{P}(0) = \int_0^{\Delta t} dt\, \mathbf{j}(t) \tag{2.119}$$

In the adiabatic limit, $\mathbf{j} \to 0$ and $\Delta t \to \infty$. By replacing t by the parameter λ, a dimensionless adiabatic time varying continuously from $\lambda = 0$ (initial system) to $\lambda = 1$ (final system), we have

$$\Delta \mathbf{P} = \int_0^1 d\lambda \, \frac{\partial \mathbf{P}}{\partial \lambda} \tag{2.120}$$

$\lambda = 0$ refers to the reference centrosymmetric structure, and $\lambda = 1$ is the polarised structure, and $\Delta \mathbf{P}$ corresponds to the spontaneous polarisation [87]. The macroscopic electric field is required to vanish for any value of the parameter λ [87, 95].

Integrating Eq. 2.120 with respect to λ, the effective polarisation is:

$$\Delta \mathbf{P} = \Delta \mathbf{P}_{\text{ion}} + [\mathbf{P}_{\text{el}}(1) - \mathbf{P}_{\text{el}}(0)] \tag{2.121}$$

where $\mathbf{P}_{\text{ion}}$ refers to the nuclear contribution.

The eigenfunctions obey both the Bloch relation: $\psi_{n\mathbf{k}}(\mathbf{r}) = e^{i\mathbf{k}.\mathbf{r}} u_{n\mathbf{k}}(\mathbf{r})$, where $u_{n\mathbf{k}}(\mathbf{r}) = e^{i\mathbf{G}\cdot\mathbf{r}} u_{n,\mathbf{k}+\mathbf{G}}(\mathbf{r})$ is lattice-periodic for all reciprocal lattice vectors $\mathbf{G}$ and n is the band index; and the Schrödinger equation: $H_{\mathbf{k},\lambda}|u_{n\mathbf{k}}\rangle = E_{n\mathbf{k}}|u_{n\mathbf{k}}\rangle$, where $H_{\mathbf{k},\lambda} = (\mathbf{p} + \mathbf{k})^2/2m + V_{\text{KS},\lambda}$. These quantities depend on λ, which changes slowly in time, such that the wave-functions acquire a first-order perturbation correction [94].

The corresponding first-order current is then

$$\mathbf{j}_n = \frac{\partial \mathbf{P}_n}{\partial t} = \frac{ie\dot{\lambda}}{(2\pi)^3} \sum_{m \neq n} \int d\mathbf{k} \, \frac{\langle \psi_{n\mathbf{k}}|\mathbf{p}|\psi_{m\mathbf{k}}\rangle \langle \psi_{m\mathbf{k}}|\frac{\partial V_{\text{KS}}}{\partial \lambda}|\psi_{n\mathbf{k}}\rangle}{E_{n\mathbf{k}} - E_{m\mathbf{k}}} + c.c. \tag{2.122}$$

where m are the unoccupied bands, e is the electron charge, and $c.c.$ is the complex conjugate. Since

$$\frac{\partial \mathbf{P}_n}{\partial t} = \frac{\partial \lambda}{\partial t} \Longleftrightarrow \frac{\partial \mathbf{P}_n}{\partial \lambda} = \frac{\partial t}{\partial t}$$

we can remove t and rewrite the matrix elements as cell-periodic functions, where the expectation values in terms of the commutators follow from the definition of $H_{\mathbf{k},\lambda}$ [95]:

$$\langle \psi_{n\mathbf{k}}|\mathbf{p}|\psi_{m\mathbf{k}}\rangle = \left\langle u_{n\mathbf{k}} \middle| \left[\frac{\partial}{\partial \mathbf{k}}, H_{\mathbf{k},\lambda} \right] \middle| u_{m\mathbf{k}} \right\rangle \tag{2.123}$$

and

$$\left\langle \psi_{n\mathbf{k}} \middle| \frac{\partial V_{\mathbf{k},\lambda}}{\partial \lambda} \middle| \psi_{m\mathbf{k}} \right\rangle = \left\langle u_{n\mathbf{k}} \middle| \left[\frac{\partial}{\partial \lambda}, H_{\mathbf{k},\lambda} \right] \middle| u_{m\mathbf{k}} \right\rangle \tag{2.124}$$

Therefore, substituting Eqs. 2.123 and 2.124 into Eq. 2.122, we obtain:

$$\frac{\partial \mathbf{P}_n}{\partial \lambda} = \frac{ie}{(2\pi)^3} \int d\mathbf{k} \left\langle \frac{\partial u_{n\mathbf{k}}}{\partial \mathbf{k}} \mid \frac{\partial u_{n\mathbf{k}}}{\partial \lambda} \right\rangle + c.c. \tag{2.125}$$

The sum over unoccupied bands m disappears, which indicates the polarisation to be a ground-state property.

By using Eq. 2.121 in Eq. 2.125, summing over the occupied bands and integrating by parts with respect to λ, we hence obtain the spontaneous polarisation [87, 94]

$$\Delta \mathbf{P}_{\text{el}} = \frac{ie}{(2\pi)^3} \sum_n \int d\mathbf{k} \left\{ \left[\left\langle u_{n\mathbf{k}} \left| \frac{\partial}{\partial \mathbf{k}} \right| u_{n\mathbf{k}} \right\rangle \right]_0^1 - \int_0^1 d\lambda \, \frac{\partial}{\partial \mathbf{k}} \left\langle u_{n\mathbf{k}} \left| \frac{\partial}{\partial \lambda} \right| u_{n\mathbf{k}} \right\rangle \right\} \tag{2.126}$$

Since the last term of Eq. 2.126 is periodic in $\mathbf{k}$, the gradient of this quantity integrated over the BZ is zero[10]. Therefore, we arrive at:

$$\mathbf{P}_{\text{el}}(\lambda) = \frac{ie}{(2\pi)^3} \sum_n \int d\mathbf{k} \left\langle u_{n\mathbf{k}} \left| \frac{\partial}{\partial \mathbf{k}} \right| u_{n\mathbf{k}} \right\rangle \tag{2.127}$$

The term $A(\mathbf{k}) = i \left\langle u_{n\mathbf{k}} \left| \frac{\partial}{\partial \mathbf{k}} \right| u_{n\mathbf{k}} \right\rangle = i \left\langle u_{n\mathbf{k}} \left| \nabla_{\mathbf{k}} \right| u_{n\mathbf{k}} \right\rangle$ is the Berry connection, also known as the gauge potential. The Berry phase is therefore the integration over a closed manifold, which in the present context is the Brillouin zone [96, 87]. The result will only depend on the end-points and ignore the path defined by the parameter space.

The total polarisation is finally obtained by adding the ionic contribution to Eq. 2.127 [87], $\mathbf{P} = \mathbf{P}_{\text{el}} + \mathbf{P}_{\text{ion}}$. Therefore:

$$\mathbf{P} = \underbrace{\frac{ie}{(2\pi)^3} \sum_n \int d\mathbf{k} \left\langle u_{n\mathbf{k}} \left| \frac{\partial}{\partial \mathbf{k}} \right| u_{n\mathbf{k}} \right\rangle}_{\mathbf{P}_{\text{el}}} + \underbrace{\frac{e}{\Omega} \sum_s Z_s^{\text{ion}} \mathbf{r}_s}_{\mathbf{P}_{\text{ion}}} \tag{2.128}$$

where Ω is the volume of the unit-cell, Z_s^{ion} are the bare nuclear charges located at the atomic positions $\mathbf{r}_s$, and the band index n runs over all bands [11] [87].

The formal polarisation obtained in Eq. 2.128 is a well-defined modulo $e\mathbf{R}/\Omega$ ($\mathbf{R}$ is any lattice vector). For a given adiabatic path, defined in Eq. 2.120, the change in polarisation is given by a single-value vector quantity that is perfectly well defined. Since the integrated adiabatic current flow is $\Delta \mathbf{P} = (\mathbf{P}_{\lambda=1} - \mathbf{P}_{\lambda=0}) + e\mathbf{R}/\Omega$ [87], this last term will represent the quanta of polarisation which is obtained in integer multiples of 2π [95]. The geometric phase

[10] From Gauss's theorem (surface integral) $\int_V (\nabla \cdot \mathbf{A}) d\tau = \oint_S \mathbf{A} \cdot d\mathbf{s}$, and $\mathbf{A} \to 0$ everywhere on the surface of an arbitrarily large enclosure.

[11] When performing a pseudopotential calculation, n runs only over the valence bands and Z^{ion} is the net positive charge of the nucleus and the core electrons.

is non-zero only if the periodic functions, $u_{n\mathbf{k}}$, are complex. This only occurs when there is no center of inversion, which is the condition under which spontaneous polarisation emerges. The change in macroscopic polarisation between two different insulating states can therefore be seen as a measure of phase differences between the initial and final wave-functions [95].

2.5.2 Born-Effective Charges

The definition of Born-effective charge (BEC), Z^*, is the induced polarisation of the bulk along direction i due to a unit displacement direction j of equivalent ions [93] in zero macroscopic electric field [87]:

$$Z^*_{ij} = \frac{\Omega}{e}\frac{\delta P_i}{\delta d_j} \tag{2.129}$$

The BEC tensors, Z^*_{ij}, measure the coupling of a macroscopic field with relative sub-lattice displacements (zone-centre phonons) [87].

The change in polarisation due to ionic displacements is thus determined by the effective charge times the displacement

$$\partial P_i = \frac{e}{\Omega} Z^*_{ij} \delta d_j \tag{2.130}$$

The total polarisation is then obtained by summing over the contributions from the displacements of all ions [93].

In highly polarisable ferroelectrics, small electric fields generate large forces on the ions, which are mediated by the anomalously large BECs. The force induced on an ion by a uniform macroscopic electric field E at direction j, is given by:

$$Z^*_{ij} = -e\frac{\delta F_i}{\delta E_j} \tag{2.131}$$

It is possible to calculate the BEC tensors either with linear-response approximations (e.g. density-functional perturbation theory - DFPT) or using the Berry phase relations, where the derivative of 2.129 is approximated using finite-differences, i.e.:

$$\frac{\partial P^z}{\partial d_z} \approx \frac{P^z(+\delta z) - P^z(-\delta z)}{2\delta} \tag{2.132}$$

where $P^z(\pm\delta z)$ is the polarisation induced along the positive/negative z-direction when an ion is displaced by a small amount, δ.

The BECs are useful for analysing ferroelectric materials, where anomalously large values

of the BEC are typically characteristic of these physical phenomena [97]. These charges are also essential in defining the LO-TO optical phonon splitting in polar crystals.

2.5.3 Landau Theory of Ferroelectrics

Landau theory serves as a bridge between microscopic models and macroscopic phenomena. The theory assumes spatial averaging of local fluctuations, and is therefore well suited to studying systems with long-range interactions, such as ferroelectrics [88].

Since Landau theory is a symmetry-based analysis of equilibrium behaviour near a transition, it is possible to use this theory to describe a phase transition. Phase-transitions may be first-order, when a discontinuous change in the structure and entropy is observed, and hence latent heat at the transition temperature is evidenced; or second-order, where the structure of the low-temperature phase varies continuously to the high-temperature phase and only a discontinuity in the derivative of the entropy is observed [9].

Landau theory can be seen as a Taylor expansion of the free energy in terms of an order parameter. The order parameter describes the change in symmetry through the phase transition, and is defined as zero for the high-symmetry (ordered) phase, and changes continuously to a finite value as the symmetry lowers. For the example of a paraelectric-to-ferroelectric phase transition, the polarisation, P, is typically chosen to be the order parameter [88]. At the vicinity of the transition, the free energy, $\mathcal{F}$, is expanded as a power series of P:

$$\mathcal{F}(T) = \frac{1}{2}a(T)P^2 + \frac{1}{4}b(T)P^4 + \frac{1}{6}c(T)P^6 + \cdots - EP \tag{2.133}$$

where a, b and c are temperature-dependent coefficients, E is the electric field and P the polarisation. The equilibrium configuration is determined by minimizing $\mathcal{F}$ with respect to P:

$$\frac{\partial \mathcal{F}}{\partial P} = 0 \tag{2.134}$$

If the coefficients are all positive, the free energy has a minimum at the origin (Fig. 2-12.a). Ignoring the higher-order terms and considering only terms up to the second order (assuming that the values of the higher-order coefficients are relatively small), the polarisation induced by an electric field is calculated by [10]

$$\frac{\partial \mathcal{F}}{\partial P} = aP - E = 0 \tag{2.135}$$

and thus one obtains the dielectric susceptibility

$$\chi = \frac{P}{E} = \frac{1}{a} \tag{2.136}$$

If the coefficients were chosen such that $a < 0$, while $b > 0$ and $c > 0$, then $\mathcal{F}$ would resemble Fig. 2-12.b, with a minimum located at a finite polarisation, P. The ground-state would thus have a spontaneous polarisation and would therefore be ferroelectric [88]. If one assumes that $a(T)$ varies linearly with temperature (changing sign at the transition temperature, T_0), a ferroelectric transition would occur.

On the other hand, when $b < 0$, and $c > 0$, we obtain a first-order phase transition, since the quartic coefficient is negative, and hence $T > T_0$, and $\mathcal{F}$ has a minimum at $P \neq 0$. As a is reduced, the temperature is lowered, and the minimum will decrease in energy to below the unpolarised state, and hence will be the thermodynamically favourable phase. The temperature at which this effect occurs is the Curie temperature, T_c, which exceeds T_0. At temperatures between T_c and T_0, the unpolarised phase exists as a local minimum (Fig. 2-13).

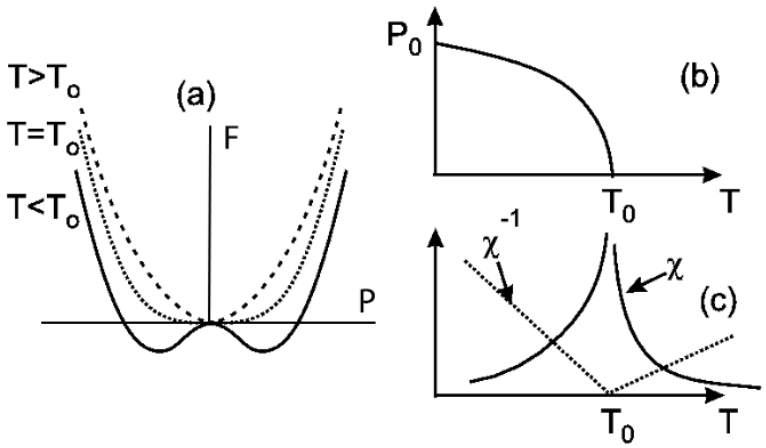

Figure 2-12: Squematics of second-order phase transitions. a) Free energy as a function of polarisation for temperature ranges above and below the transition temperature. b) Spontaneous polarisation $P_0(T)$ as a function of temperature; P vanishes smoothly at the transition temperature $T_c = T_0$. c) Dielectric susceptibility χ as a function of T (from Ref. [10]).

2.6 Methodology Overview and Applications

Several methodologies have been discussed throughout the present chapter and the aim was intended to provide an overview of existing methodologies to study the electronic and phonon properties of bulk materials and clarify the technical capabilities of respective methods. Density-Functional Theory, by applying plane-wave basis sets and PAW pseudopotentials, has been used for all the studied systems. The goal was to compute the optimized structures and respective *ab initio* equilibrium properties (lattice parameters, bulk modulii) and the

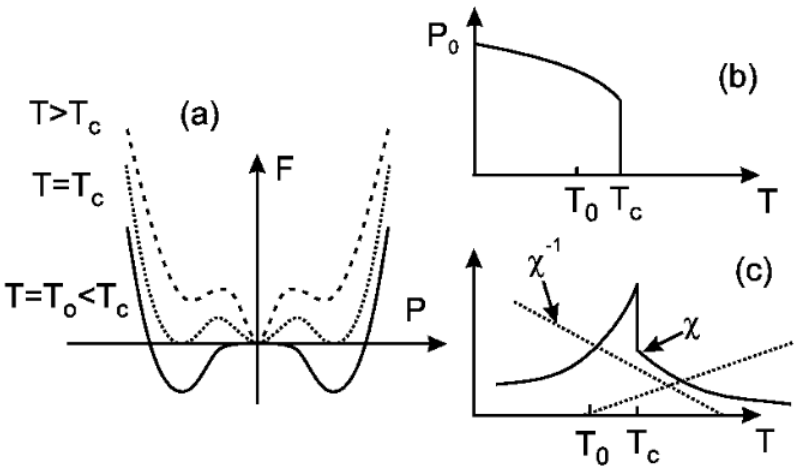

Figure 2-13: Schematics of a first-order phase transition. a) Free energy as a function of polarisation for temperature ranges above and below the transition. b) Spontaneous polarisation $P_0(T)$ as a function of temperature; the order parameter jumps discontinuously to zero at $T = T_c$. c) Dielectric susceptibility χ as a function of T (from Ref. [10]).

force-constants, required for lattice dynamics calculations. Moreover, for the bilayer graphene the electronic band structures were computed within the DFT framework. Lattice dynamics calculations were carried out for the three projects to compute the thermal properties and phonon dispersions of the systems under interest. For the $CsSnI_3$ and GeTe structures the quasi-harmonic approximation was employed in order to model the temperature dependence of the material properties on the DFT free-energy surface, whereas for the bilayer graphene system only the harmonic approximation was used to compute the phonon dispersion as a function of the applied perturbation. While for the perovskite $CsSnI_3$ system, a more complete analysis of the temperature dependant properties was performed (Gibbs free energy, thermal expansion, temperature-dependant bulk modulus, Grüneisen parameter, etc), for the GeTe system the quasi-harmonic approach was mostly employed to analyse the phonon dipsersion as a function of temperature in order to probe the dynamical stability of the two phases of GeTe.

Moreover further analysis was required to study the specific nature of each of the systems under interest, reason why other methodologies were also applied.

For the $CsSnI_3$ structure interest lay in decomposing the structural distortion into contributions from lattice modes with different symmetries, and investigate the physical mechanisms which stabilise the *Pnma* phase. For such purpose the AMPLIMODES code was required.

Many-body perturbation theory (self-consistent method) was chosen to compute the quasi-particle electronic band structure of the ferroelectric phase of GeTe and therefore obtain a more accurate description of the Rashba-spin splitting. The code used to carry out such calculations

was an all-electron code which makes use of Plus Muffin-Tin Orbitals to expand the Kohn-Sham wavefunctions, integrating both atom-centered and plane-wave envelope functions.

To analyse the macroscopic mechanism of the ferroelectric transition, and to model respective properties through the phase transition, one also needs to utilise phenomenological Landau theories. We have applied this model, in conjunction with our DFT free-energy calculations, to calculate the evolution of the polarisation, from the centrosymmetric to the ferroelectric phase, and therefore assessing the hysteresis behavior for this specific system. Since one of the input parameters required to evaluate the Landau free energy are the dielectric constants, and since these are dependant on the band-gap width of the material, hybrid functionals (HSE06) was used. The semi-local functional, PBEsol, underestimates the width of the gap providing a metallic description of the high-symmetry phase of GeTe and therefore widely overestimating the dielectric constant. The non-local HSE06 functional provides a better quantitative description of the band-gap and hence more accurate values of the dielectric constants. Since the spoantanoues polarisation was also required as input for the Free energy, the Berry phase calculations were perfomred and therefore obtaining the polarisation difference between the low-symmetry and high-symmetry structures.

To analyse the bilayer graphene systems convergence of the **k**-points against a very dense sampling mesh was essencial in order to obtain a reliable description of the electronic band-structures at the vicinity of the Fermi energy. This feature was mainly observed for the AA-stacking environment for which the crossing of the bands occur away from a high-symmetry **k**-point. For such, band-structures computed with tight-binding methods were used for comparative purposes when studying the acuraccy and convergence of the electronic band-structures reproduced by DFT-LDA.

Chapter 3

Cesium Tin Iodide ($CsSnI_3$)

Paths are made by walking
Franz Kafka

The ground-state phases of most fluoride and halide perovskites are paraelectric (typically a non-polar *Pnma* phase), exhibit a ferroelectric instability in their higher-symmetry tetragonal phases. This feature is also commonly observed in oxide perovskites. Nevertheless, while in oxide perovskites ferroelectric instabilities may be induced through pressure or strain, this may not be the case for instabilities originating from geometric effects (e.g. ionic radii in fluoride or halide perovskites) [98]. Exceptions to this rule do exist, for example $NaMnF_3$ [98], where coherent heteroepitaxy destabilizes the *Pnma* structure, leading to a ferroelectric (and, indeed multiferroic) ground state with an unusual polarisation/strain response.

$CsSnI_3$ is an interesting inorganic halide-perovskite system which exhibits three different perovskite phases [99, 16, 100], *viz.* two high-temperature and two ground-state forms. In the present work, by employing the finite-displacement technique with density-functional theory, we obtained the full phonon band structures and densities of states (DoSs) of all these phases. As found in other literature [16, 100], we observed imaginary modes in the cubic $Pm\bar{3}m$ and tetragonal $P4/mbm$ phases. This indicates that the tetragonal phase is dynamically unstable, with the phonon dispersion displaying imaginary optic modes at the high-symmetry wavevectors in the Brillouin zone. Soft modes were also observed at the zone centre, indicating the existence of a ferroelectric instability. The main contribution to the imaginary modes were found to be the "rattling" motion of the caesium atom inside the perovskite cage. The cubic structure also displays a zone-boundary instability, which is associated with motions of the Sn-I cage framework.

We have also employed symmetry-mode analysis to decompose the structural distortions into contributions from lattice modes with different symmetries. These are characterised by the irreducible representations of the "aristotype" cubic structure [101]. The relations between

the displacement patterns of the soft phonon modes and the phase transitions between the high-symmetry $Pm\bar{3}m$ and the low-symmetry $Pnma$ phases will be discussed in detail for the $CsSnI_3$ perovskite system.

3.1 Phase Stability and Transformations in the Halide Perovskite $CsSnI_3$

The following paper summarises the work carried out during the first year of the PhD programme by carrying out a complete study (electronic and vibrational) of the three different phases of the halide perovskite $CsSnI_3$. Within the present study, personal contributions implied applying the acquired knowledge of DFT electronic structure calculations (plane-wave expansion of the Kohn-Sham wavefunctions and PAW pseudopotentials), and learning the necessary theoretical background to carry out lattice dynamics calculations within the harmonic and the quasi-harmonic approximations.

The following version is published as Da Silva, EL, Skelton, JM, Parker, SC & Walsh, A 2015, 'Phase stability and transformations in the halide perovskite CsSnI3', Physical Review B, vol. 91, no. 14, 144107 available online via: https://doi.org/10.1103/PhysRevB.91.144107 (C) American Physical Society, 2015.

Phase stability and transformations in the halide perovskite $CsSnI_3$

E. Lora da Silva, Jonathan M. Skelton, Stephen C. Parker, and Aron Walsh*
Department of Chemistry, University of Bath, Bath, United Kingdom
(Received 27 February 2015; published 17 April 2015)

We employ the quasiharmonic approximation to study the temperature-dependent lattice dynamics of the four different phases of cesium tin iodide ($CsSnI_3$). Within this framework, we obtain the temperature dependence of a number of structural properties, including the cell volume, bulk modulus, and Grüneisen parameter. The Gibbs free energy of each phase is compared against the temperature-dependent Helmholtz energy obtained from the equilibrium structure within the harmonic approximation. We find that the black tetragonal perovskite phase is not dynamically stable up to at least 500 K, with the phonon dispersion displaying negative optic modes, which pass through all of the high-symmetry wave vectors in the Brillouin zone. The main contributions to the negative modes are found to be motions of the Cs atom inside the perovskite cage. The black cubic perovskite structure shows a zone-boundary instability, indicated by soft modes at the special **q** points M and R. These modes are present in calculations at the equilibrium (0 K) lattice constant, while at finite temperature additional negative modes develop at the zone center, indicating a ferroelectric instability. The yellow crystal, composed of one-dimensional $(SnI_6)_n$ double chains, has the same heat of formation as the orthorhombic perovskite phase at 0 K, but becomes less energetically favorable at higher temperatures, due to its higher free energy.

DOI: 10.1103/PhysRevB.91.144107 PACS number(s): 63.20.D−, 63.20.Ry, 63.70.+h

I. INTRODUCTION

$CsSnI_3$ belongs to the perovskite family of materials with the chemical formula ABX_3 (A = Cs, B = Sn, and X = I). This material undergoes a number of temperature-dependent phase changes [1], corresponding mostly to rotations and distortions of the perovskite octahedral cage formed by the Sn-I bonding environment. Such distortions include bond angle changes and the displacement of the caged cation [2].

There are two orthorhombic structures, which coexist at room temperature, belonging to the $Pnma$ space group. One of these structures is an edge-connected one-dimensional (1D) double-chain crystal (Y), which is yellow in color and has an indirect band gap of 2.6 eV. The other structure is a corner-linked 3D perovskite (Bγ), discovered by Yamada *et al.* [3] in 1991, which is black in color and has p-type conductivity with a direct band gap of 1.3 eV. When exposed to air or organic solvents, the Bγ phase undergoes a reconstructive phase transition to the Y phase under ambient conditions.

Above room temperature, two higher-symmetry structures are observed. When heated above 425 K, the Y phase transforms to a black cubic Bα phase, with the $Pm\bar{3}m$ space group. It was demonstrated by thermal analysis and x-ray diffraction (XRD) that during cooling the Bα structure deforms to a tetragonal (Bβ) structure ($P4/mbm$ space group) at 426 K [4]. On further cooling, the Bβ converts back to the Bγ phase at 351 K [1,3]. The crystal structures of the four phases are shown in Fig. 1.

The majority of the low-symmetry perovskite phases can be derived from the high-symmetry cubic structure (known as aristotypes) [5] by rigid tilting of the octahedral units around one or more of their symmetry axes, maintaining both the regularity of the octahedra and their corner connectivity [5]. Hence, the equilibrium position of the Cs atom can be thought of as being determined by the position and tilting of the SnI_6 octahedra for a given set of bond angles [2]. The tilting of the octahedra can be interpreted in terms of lattice-vibrational modes, with those giving rise to obvious tilt systems corresponding to some of the most important modes associated with the phase transitions in the system [6]. Based on a group-theoretical analysis employing Glazer's notation [6] and the Landau theory of phase transitions, Howard and Stokes [5] defined the group-subgroup relationships among the 15 possible space groups resulting from octahedral tilting. The order of the phase transition was identified by expressing the order parameter as a linear combination of basis functions defining a particular tilt system.

Based on this work, the $Pm\bar{3}m \rightarrow P4/mbm$ space group transition (which will correspond to the B$\alpha \rightarrow$ Bβ transition in the present study) was identified as being a continuous second-order transition, in which one rotation occurs about the c axis [5,7]. The $P4/mbm \rightarrow Pnma$ transition (corresponding to the B$\beta \rightarrow$ Bγ transition) was similarly characterized as being second order.

The unusual properties of the various $CsSnI_3$ phases, in particular the low-temperature Bγ polymorph, have attracted interest for a variety of applications. Its optical properties make it useful for light-emitting diodes, particularly as it is soluble in certain organic solvents, and can therefore be deposited on substrates or inside porous structures by solution processing [8]. Also, its strong luminescence and large optical absorption coefficient at shorter wavelengths make it suitable for photovoltaics, and high efficiency has been observed for solar-cell applications [1,8]. It is a viable Pb-free alternative to the hybrid halide perovskite $CH_3NH_3PbI_3$ [9–14]. In addition, its high hole mobility, due to the small hole effective mass, make it an excellent solid-state replacement for the electrolyte in dye-sensitized solar cells [15]. The cubic phase of $CsSnI_3$ also has interesting structural and optical properties, with high absorption coefficients at infrared, visible, and ultraviolet wavelengths, making it useful for optical and optoelectronic applications working within this range of the electromagnetic spectrum [16].

*a.walsh@bath.ac.uk

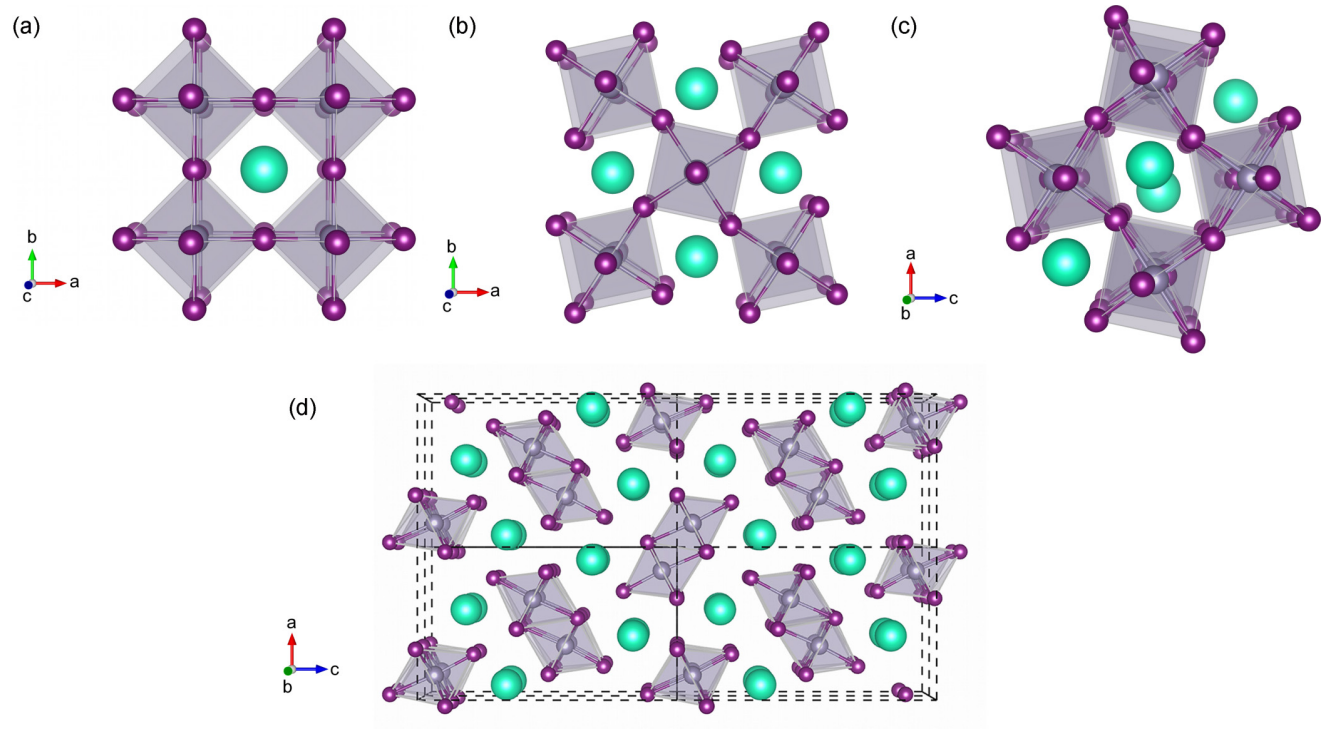

FIG. 1. (Color online) The four polymorphs of $CsSnI_3$. On the top row, the three black perovskite structures are shown: (a) cubic Bα, (b) tetragonal Bβ, and (c) orthorhombic Bγ. The bottom row shows the yellow crystal where the tin halide octahedral networks are fragmented into one-dimensional chains (d). In all four images, the green spheres represent the Cs atom, while the purple polyhedra represent the octahedral perovskite cage formed by the bonding of the Sn (steel blue) and I (dark purple) atoms.

By exploring the Cs position offsets and lattice expansion [2], it has been predicted that the Bα structure is never an energy minimum, and can be deformed to the Bβ state without any energy barriers [2]. The structural transition between the Bβ and Bγ phases is also expected to be reversible with temperature [2]. However, the Bα and Bβ phases are both high-temperature structures, and, according to Ref. [7], the phase transitions are related to soft-mode displacements. The temperature dependence of the phonon frequencies of the four structures, and the corresponding effect on the crystal entropy and free energy, are thus likely to play an important role in defining the phase equilibria; these effects are not taken into account through the internal lattice energies of the system obtained from athermal electronic-structure calculations.

Over the past year, many studies have been carried out on $CsSnI_3$, focusing mainly on characterizing the phase transitions between the black and yellow forms. In particular, recent work carried out by Huang and Lambrecht [7] has provided a more fundamental view of the phase equilibria in $CsSnI_3$, identifying the soft phonon modes which underpin the transformations between them.

In the present work, we perform quasiharmonic lattice-dynamics calculations to characterize the temperature dependence of the properties of the four phases of $CsSnI_3$, focusing in particular on the form of the phonon dispersions and the relative Gibbs free energy. When mapping out the free energy as a function of temperature based on the 0 K equilibrium structure, the lattice vibrations are modeled as independent harmonic oscillators, and the constant-volume (Helmholtz) free energy is defined as a sum of the lattice energy and the (temperature-dependent) vibrational contribution from the population of the phonon energy levels [17]. However, variation in the lattice volume due to thermal expansion/contraction leads to changes in both the lattice energy and the phonon frequencies, which causes a temperature dependence of the thermodynamic potentials. These anharmonic effects, which are taken into account in the quasiharmonic approximation (QHA), may be required to reproduce the subtleties of the free-energy landscape. The calculations also yield structural properties as a function of temperature, giving a first-principles estimate of the temperature dependence of the lattice volume, thermal-expansion coefficient, and other thermoelastic properties.

II. QUASIHARMONIC APPROXIMATION

In statistical physics, the Helmoltz free energy, F, is defined in terms of the canonical partition function, Z, by the so-called bridge relation:

$$F = -k_B T \ln Z, \tag{1}$$

where k_B is the Boltzmann constant and T the temperature. Z defines the partitioning of energy among the energy levels associated with the degrees of freedom of the system [17,18], and for a solid is given by:

$$Z(T) = \exp\left(-\phi/k_B T\right) \prod_{\mathbf{q},\nu} \frac{\exp\left[-\hbar\omega(\mathbf{q},\nu)/2k_B T\right]}{1-\exp\left[-\hbar\omega(\mathbf{q},\nu)/k_B T\right]}, \tag{2}$$

where ϕ is the potential energy of the system, and the product runs over vibrational modes ν and reciprocal-space

wave vectors $\mathbf{q}$, with the phonon occupation number for each mode obtained from a Bose-Einstein distribution using the characteristic oscillator frequency ω. [18,19]

The temperature-dependent Helmoltz free energy is hence given by [20]:

$$F(V,T) = \phi + \frac{1}{2}\sum_{\mathbf{q},\nu}\hbar\omega(\mathbf{q},\nu) + k_{\mathrm{B}}T\sum_{\mathbf{q},\nu}\ln\{1-\exp[-\hbar\omega(\mathbf{q},\nu/k_{\mathrm{B}}T)]\} \quad (3)$$

with $\hbar$ being the reduced Planck constant. The second term is a sum of the modal contributions to the zero-point vibrational energy, and the third term is the contribution of each mode to the free energy due to thermal occupation of the phonon energy levels.

Phonon frequencies are derived from the restoring force in response to the displacement of ions by a small amplitude from their equilibrium positions. The interatomic force constants (IFCs) can either be computed from perturbation theory (e.g., density-functional perturbation theory), or by performing force calculations on a series of symmetry-inequivalent displaced structures and fitting the force/displacement curves to a harmonic function. In the latter finite-displacement (direct) method, the Parlinski-Li-Kawazoe supercell approach is commonly employed [21,22] to capture the long-range contributions to the IFCs between atoms in different crystallographic unit cells, which are needed to accurately calculate the frequencies of short-wavelength phonon modes [19].

In the harmonic model, the equilibrium distance between atoms is independent of temperature. The anharmonic effects needed to account for thermal expansion can be introduced by the QHA, in which the thermal expansion of the crystal lattice is obtained from the volume dependence of the phonon frequencies. The evaluation of the equilibrium volume and Gibbs free energy at a temperature T is obtained by minimising the function $F(V,T)$ for a given (constant) pressure p [17,20]:

$$G(T,p) = \min_{V}[F(V,T) + pV], \quad (4)$$

where $\min_{V}$ means that for each value of T and p, the function is minimized with respect to volume.

To perform a QHA calculation, the phonon frequencies are computed for a range of expansions and compressions about the 0 K equilibrium volume, and the constant-volume free energy for each calculation is evaluated as a function of temperature. From this approach, the equilibrium volume, bulk modulus, and Gibbs free energy can be obtained at arbitrary temperatures by fitting the free energy as a function of volume to an equation of state [23,24]. The temperature dependence of various derived properties, e.g., volumetric expansion coefficients and the mean Grüneisen parameter, are then readily obtained.

The mode Grüneisen paramaters, $\gamma_{\mathbf{q},\nu}$, quantify the change in each phonon frequency with volume V through [25,26]:

$$\gamma_{\mathbf{q},\nu} = -\frac{V}{\omega_{\mathbf{q},\nu}}\frac{\partial\omega_{\mathbf{q},\nu}}{\partial V} = -\frac{\partial\ln\omega_{\mathbf{q},\nu}}{\partial\ln V}. \quad (5)$$

These are related to the temperature-dependent mean Grüneisen parameter by:

$$\gamma = \sum_{\mathbf{q},\nu}\frac{C_{\mathbf{q},\nu}\gamma_{\mathbf{q},\nu}}{C_{\mathrm{V}}}, \quad (6)$$

where C_{V} is the constant-volume heat capacity, and $C_{\mathbf{q},\nu}$ are the contributions from individual modes:

$$C_{\mathbf{q},\nu} = \hbar\omega_{\mathbf{q},\nu}\frac{\partial n(T,\omega_{\mathbf{q},\nu})}{\partial T} \quad (7)$$

with $n(T,\omega_{\mathbf{q},\nu})$ being the phonon occupation number.

Within the QHA, the mode Grüneisen parameter [and, by Eq. (6), the mean Grüneisen parameter] is related to the volumetric thermal expansion coefficient, α_{V}, according to:

$$\alpha_{\mathrm{V}} = \frac{\partial\ln V}{\partial T} = \frac{1}{BV}\sum_{\mathbf{q},\nu}C_{\mathbf{q},\nu}\gamma_{\mathbf{q},\nu}, \quad (8)$$

where B is the (temperature-dependent) bulk modulus.

When the mean Grüneisen parameter γ is negative, α_{V} will likewise be negative, indicating negative thermal expansion (NTE), i.e., a reduction in volume upon heating [25,27,28]. NTE behavior in bulk systems has been linked to a number of microscopic mechanisms, including, among others, ferroelectric, magnetostrictive, and displacive phase transitions, low-frequency phonon modes and rigid-unit modes [27].

III. COMPUTATIONAL METHODOLOGY

Electronic-structure calculations were performed within the density-functional theory (DFT) [29,30] framework, as implemented in the Vienna *Ab initio* Simulation Package (VASP) code [31–33]. The semilocal generalized-gradient approximation functional with the Perdew-Burke-Ernzerhof parametrization revised for solids (PBEsol) [34,35] was employed for all the calculations. Projector augmented-wave (PAW) [36,37] pseudopotentials were used to treat semi-core electronic states, with the Cs[$5s^25p^66s^1$], I[$5s^25p^5$] and Sn[$5s^25p^2$] electrons being treated as valence states.

The starting point for our calculations was a full structural relaxation of the four phases, performed with a plane-wave kinetic-energy cutoff of 800 eV. Such a high cutoff was found necessary to converge the phonon dispersion curves (see Appendix A). The Brillouin zone (BZ) was sampled with Γ-centered Monkhorst-Pack meshes [38] with subdivisions of Bα: 8×8×8; Bβ: 8×8×9; Bγ: 6×5×6; and Y: 4×6×3.

Equilibrium volumes, lattice parameters, and bulk moduli were determined by fitting energy-volume curves to the Birch-Murnaghan equation of state [23,39] (Table I). The lattice parameters obtained in the present calculations are slightly underestimated with respect to the experimental data, which, assuming positive thermal expansion, is expected, given that these are 0 K values, whereas the experimental parameters are recorded at finite temperature [19]. The Sn-I and Cs-I bond lengths in the optimized structures are tabulated in Table II.

We also calculated the heats of formation of the four phases of $CsSnI_3$ with respect to the constituent elements in their standard states Table III; additional electronic-structure calculations were therefore carried out on the published crystal structures of Cs (Im$\bar{3}$m), Sn ($I4_1/amd$), and I (*Cmca*) [40],

TABLE I. Equilibrium volumes, lattice parameters, and bulk moduli of the four different polymorphs of $CsSnI_3$, determined by fitting to the Birch-Murnaghan equation of state [23,39]. Experimental values obtained from Ref. [1] are given in parentheses. Experimental measurements of B_0 were not available for the Bα, Bβ, and Y phases for comparison.

	V (Å^3)	a_0, b_0, c_0 (Å)	B_0 (GPa)
Bα	230.39	$a_0 = 6.13$	18.33
		($a_0 = 6.21$, $T = 500$ K)	
Bβ	453.03	$a_0 = 8.61$, $c_0 = 6.11$	17.45
		($a_0 = 8.72$ $c_0 = 6.19$, $T = 380$ K)	
Bγ	897.84	$a_0 = 8.59$, $b_0 = 12.24$, $c_0 = 8.54$	15.92
		($a_0 = 8.69$, $b_0 = 12.38$, $c_0 = 8.64$, $T = 300$ K)	(19.84, $T = 300$ K)
Y	854.65	$a_0 = 10.28$, $b_0 = 4.73$, $c_0 = 17.57$	13.07
		($a_0 = 10.35$, $b_0 = 4.76$, $c_0 = 17.68$, $T = 300$ K)	

using the same pseudopotentials and plane-wave cutoff as in the $CsSnI_3$ calculations, in order to obtain reference total energies. **k**-point convergence tests were performed for all three systems, which indicated Γ-centered meshes with 26×26×26, 32×32×34, and 16×14×16 subdivisions for Cs, Sn, and I, respectively, to be suitable.

Lattice-dynamics calculations were carried out using the supercell finite-displacement method implemented in the PHONOPY package [41,42], with VASP used as the force-constant calculator [22]. Force evaluations were performed on 2×2×2 supercells using reduced **k**-point sampling meshes of 4×4×4, 4×4×5, 3×2×3, and 2×4×2 for the Bα, Bβ, Bγ, and Y phases, respectively. The phonon frequencies were sampled on an interpolated 48×48×48 **q**-point mesh for the two high-temperature phases; due to the lower symmetries and larger primitive cells of the orthorhombic structures, the phonon frequencies for these were sampled on a 24×24×24 **q**-point mesh.

In order to correct for the long-range Coulomb interaction, which leads to a frequency splitting of the longitudinal and transverse optic modes at the zone center (LO-TO splitting), a nonanalytical correction, based on the Born effective-charge tensors and the electronic-polarization component of the macroscopic static dielectric tensor, was applied when computing the phonon band dispersions [43]. These quantities were obtained by employing the density-functional perturbation theory routines implemented in VASP [44], with calculations being performed on single unit cells of the four structures. Convergence of these quantities required increasing the **k**-point mesh to 16×16×16, 10×10×11, 10×9×10, and 6×8×5 for the Bα, Bβ, Bγ, and Y phases, respectively.

TABLE II. Unique bond lengths in the 0 K equilibrium structures of the four different phases of $CsSnI_3$. Values are given in Å.

	Sn-I	Cs-I
Bα	3.065	4.334
Bβ	3.088, 3.103	3.909, 4.272, 4.801
Bγ	3.115, 3.100, 3.107	3.847, 3.869, 3.930
		4.075, 4.084
Y	3.165, 3.008, 3.199	3.908, 4.133, 3.969
	3.326, 5.347, 5.249	3.834, 3.926, 3.855

IV. RESULTS AND DISCUSSION

A. Phase stability

To assess the relative enthalpic stabilities of the four phases, we calculated the heat of formation of $CsSnI_3$ with respect to the constituent elements according to the following:

$$\Delta H_f = E_{\text{tot}}^{\text{CsSnI}_3} - \left[E_{\text{tot/atom}}^{\text{Cs}} + E_{\text{tot/atom}}^{\text{Sn}} + 3E_{\text{tot/atom}}^{\text{I}}\right], \quad (9)$$

where $E_{\text{tot}}^{\text{CsSnI}_3}$ is the total energy (per formula unit) of the different polymorphs of $CsSnI_3$, and $E_{\text{tot/atom}}^{\text{Cs/Sn/I}}$ is the total energy per atom of the pure components in their standard states. The calculated heats of formation are tabulated in Table III; we note that neither experimental nor theoretical data was available for comparison, and thus we were unable to compare our values with other results.

The data in Table III suggest that the Y phase is enthalpically the most stable, followed closely by the Bγ and then the Bβ phases, whereas the cubic Bα phase is the least stable. This trend is consistent with the temperature ordering of the phases, and can be interpreted in terms of the relative sizes of the ions. When the ionic radii do not allow for optimal cation-halide bond lengths, it becomes energetically more favorable to displace the caged ions from their cubic positions, leading to the different distorted perovskite structures [45].

The Goldschmidt tolerance factor, t [46], for $CsSnI_3$ has been calculated to be 0.9 [7]. t is an indicator for the stability and distortion of crystal structures based on Shannon ionic radii [47], and since $t < 1$, it is expected that rotations would occur in order to stabilize the A cations in the interstitial environment, since the Sn-I cages are too big to accommodate the Cs atoms with optimal bonding. This trend is consistent with that found among the oxide perovskites, where the systems undergo transitions to the *Pnma* space group [7].

TABLE III. Heats of formation of the four polymorphs of $CsSnI_3$, calculated from the 0 K equilibrium structures. Values are given in eV per $CsSnI_3$ unit.

Phase	ΔH_f
Bα	−15.054
Bβ	−15.089
Bγ	−15.107
Y	−15.108

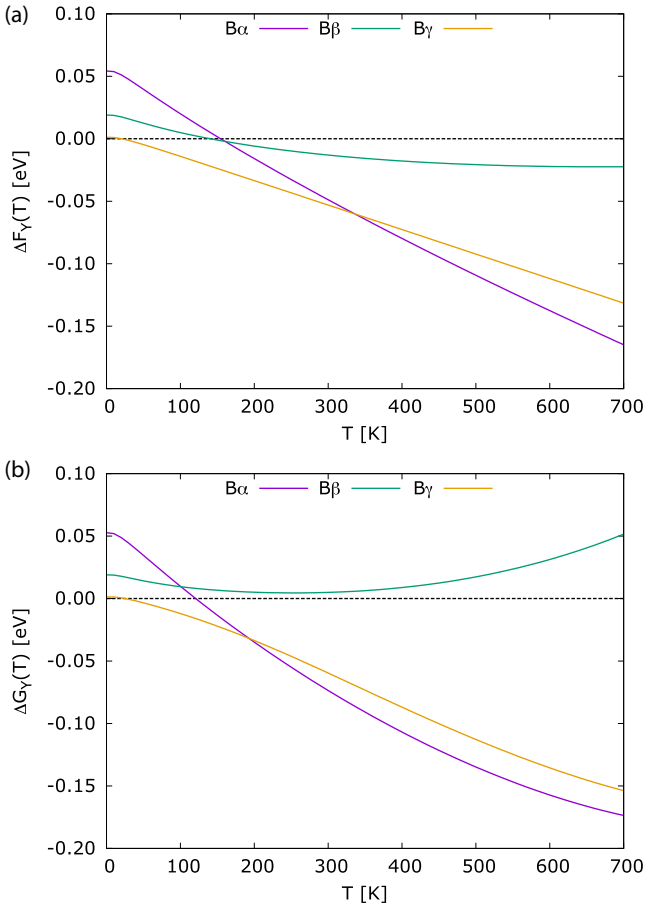

FIG. 2. (Color online) Free energy as a function of temperature for the three black $CsSnI_3$ polymorphs relative to the Y phase, which is the lowest-energy structure at 0 K. Plots (a) and (b) show the Helmoltz and Gibbs free energies, respectively. Energies are given per $CsSnI_3$ formula unit.

Within the harmonic approximation, the (Helmholtz) free energy as a function of temperature can be obtained from the phonon frequencies and lattice energy of the equilibrium structure [Eq. (3)]. By accounting for changes in the phonon frequencies due to variation in the lattice volume, the QHA calculations yield the Gibbs free energy [Eq. (4)], which is arguably more experimentally relevant. The temperature dependence of the relative (equilibrium) Helmholtz and Gibbs free energies of the four phases is compared in Fig. 2.

Both sets of data show a similar trend. At 0 K, the 1D network (Y phase) is the most stable structure, with the Bγ phase becoming favored at around 10 K. At 0 K, the cubic structure has the highest energy of the perovskite phases, and the Bγ the lowest; the energy of the Bβ phase is pinned between these competing phases. The equilibrium Helmholtz energies predict the cubic Bα phase to become stable at 300 K, transitioning directly from the Bγ phase. The corresponding transition temperature obtained from the Gibbs free energies is shifted to 200 K, but the stability trend is similar, with the Bγ structure remaining energetically close to the Bα phase up to high temperatures. These results disagree qualitatively with the electronic-structure calculations carried out by Yu *et al.* [2], which suggested that the Bα structure can be deformed to the Bβ state without any energy barrier. This highlights the importance of taking into account contributions beyond the lattice internal energy when assessing polymorph stability.

According to our results, the Bβ phase is never more stable than the competing phases within the QHA. From the Helmholtz free energy [Fig. 2(a)], there is energetic competition between the Bα, Bβ, and Y structures around 200 K, at which the Bγ structure is the most stable. Above this temperature, the Bα phase lowers and the 1D crystal increases in energy with respect to the tetragonal phase. On the other hand, the Gibbs free energy [Fig. 2(b)] predicts that the tetragonal phase is always higher in energy than the Y phase, and is consistently higher in energy than all three competing phases above 100 K.

B. Temperature dependence of structural properties

The structural properties, as a function of temperature, obtained from the QHA are shown for each phase in Fig. 3. These include the mean Grüneisen parameter, $\gamma(T)$, the volumetric thermal-expansion coefficient, $\alpha_V(T)$, the temperature-dependent bulk modulus, $B(T)$, and the temperature-dependent volume (per formula unit), $V(T)$.

The thermal expansion of all three black phases shows a similar trend [Fig. 3(b)], whereby the expansion coefficients increase from 0 K before peaking at a low temperature and then decreasing. The expansion of the Bγ and Bβ phases both peak around 150 K, and remain positive at higher temperatures. On the other hand, the Grüneisen parameter [Fig. 3(a)] of the Bα phase shows a very sharp peak at low temperature and then a notable decrease at high temperatures, becoming negative at around 200 K; this correlates with a negative volumetric thermal-expansion coefficient.

The temperature-induced volume changes in the black perovskites are dependent on the stretching of the Sn-I bonds and the tilting of the SnI_6 octahedra. As all three structures have a similar SnI_6 octahedral framework, one may infer that the octahedral cages remain largely ideal (i.e., undistorted), and so the thermal expansion is accommodated primarily by changes in the volume of the cage [48]. The thermal expansion of the cubic phase is found to be smaller than that of the lower-symmetry phases, which is consistent with theoretical analysis performed on other centrosymmetric perovskites [48].

In contrast, the lower-dimensional Y crystal exhibits a markedly different thermal-expansion trend to the black perovskite structures [Fig. 3(b)]. We interpret this as being due to the composition of the Y phase being better described by the formula $Cs_2Sn_2I_6$, where the edge-sharing octahedra condense to form infinite one-dimensional double chains of $Sn_2I_6^{2-}$, separated by the Cs cations, leading to a denser structure [1].

Figure 3(c) shows the temperature-dependent bulk moduli of the four phases of $CsSnI_3$. The bulk modulus of the cubic phase shows an apparently remarkable increase with temperature, yielding a very large value at 500 K when compared to that obtained at the 0 K equilibrium volume [$B(500K) = 418.90$ GPa and $B_0 = 18.33$ GPa, respectively; Tables I and V]. This is clearly a spurious result, and, on investigation, appears to be an artifact of the fitting of the free-energy versus volume curves to the Vinet-Rose equation of state [24] for this phase [see Appendix C, Fig. 8(a)]. There

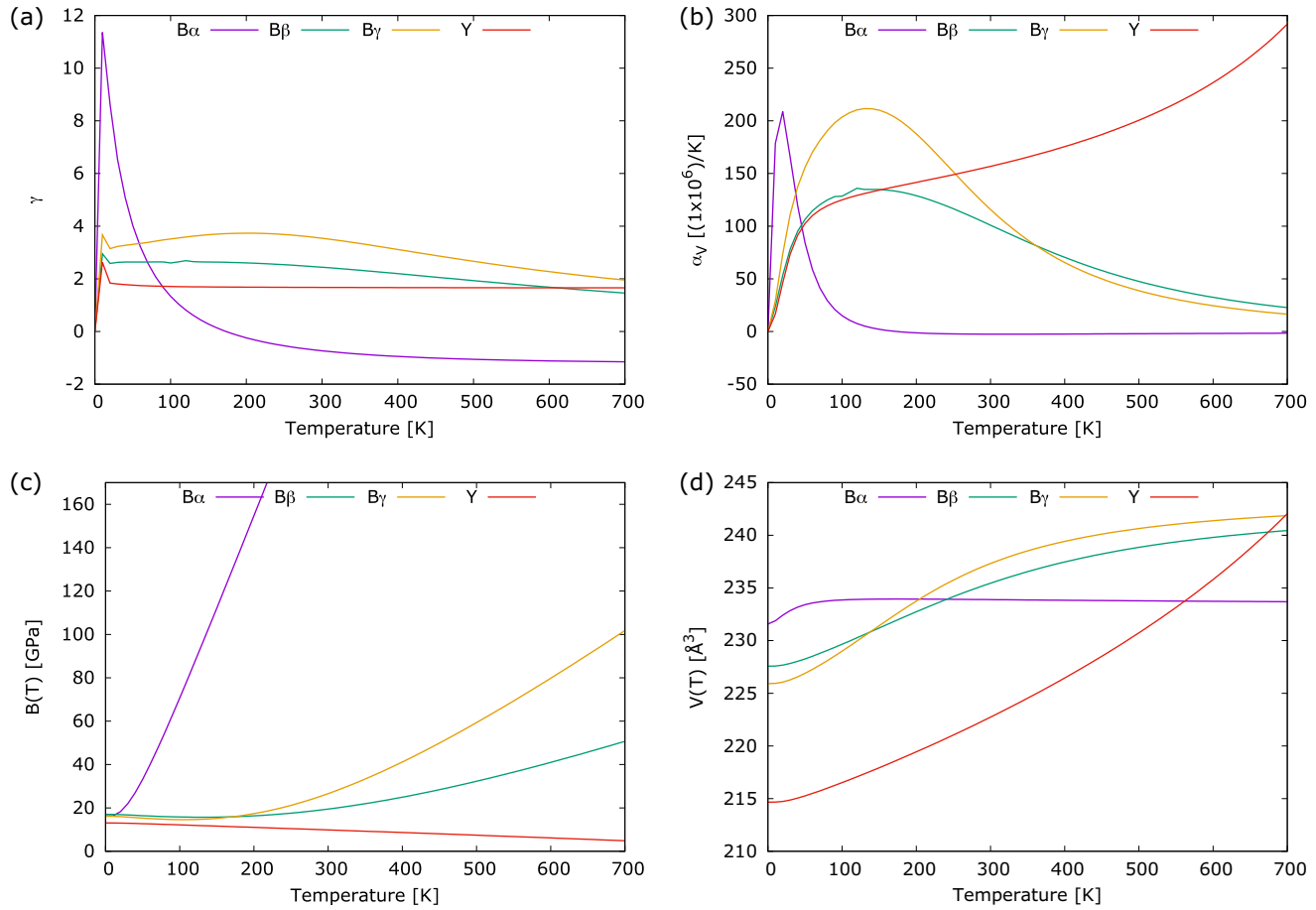

FIG. 3. (Color online) Structural properties of the four phases of $CsSnI_3$ as a function of temperature within the quasiharmonic approximation. (a) Grüneisen parameter, γ(T); (b) volumetric-expansion coefficient, α_V(T); (c) bulk modulus, $B(T)$; and (d) volume per formula unit, $V(T)$.

is a disproportionate distortion of the high-temperature free energy of the expanded structures due to the presence of the imaginary modes in the phonon density of states (see Sec. IV C).

The Bβ and Bγ phases have similar bulk moduli up to ~180 K, above which the bulk modulus of the Bγ phase increases above that of the tetragonal structure. The Y structure has the lowest bulk modulus throughout the temperature range studied. This low value is consistent with the large number of degrees of freedom, which make it a highly compressible structure. This is likewise also reflected in the volume expansion [Fig. 3(d)] when the temperature is increased.

Table IV gives the calculated properties of the four structures of $CsSnI_3$ at the temperatures quoted in Ref. [1]. The lattice parameters are compared to values obtained from this experimental study, and are notably closer to experiment than those obtained from the 0 K equilibrium-volume calculations (Table I). We note that this is despite the apparent errors in the high-temperature bulk moduli of the cubic (Bα) phase noted previously.

TABLE IV. Structural properties of the different phases of $CsSnI_3$ at the temperatures quoted in Ref. [1] (values are shown in parentheses), calculated within the quasiharmonic approximation. γ refers to the Grüneisen parameter, and α_V is the volumetric thermal expansion coefficient.

	V (Å^3)	a_0, b_0, c_0 (Å)	B_T (GPa)	γ	α_V (10^6/K)
Bα (500 K)	233.78	$a_0 = 6.16$	418.90	−1.06	−2.12
		($a_0 = 6.21$, $T = 500$ K)			
Bβ (380 K)	474.24	$a_0 = 8.74$, $c_0 = 6.21$	23.68	2.25	75.99
		($a_0 = 8.72$, $c_0 = 6.19$, $T = 380$ K)			
Bγ (300 K)	949.29	$a_0 = 8.89$, $b_0 = 12.41$, $c_0 = 8.60$	26.59	3.54	115.81
		($a_0 = 8.69$, $b_0 = 12.38$, $c_0 = 8.64$,, $T = 300$ K)	(19.84, $T = 300$ K)		
Y (300 K)	890.93	$a_0 = 10.42$, $b_0 = 4.80$, $c_0 = 17.57$	9.85	1.67	156.78
		($a_0 = 10.35$, $b_0 = 4.76$, $c_0 = 17.68$, $T = 300$ K)			

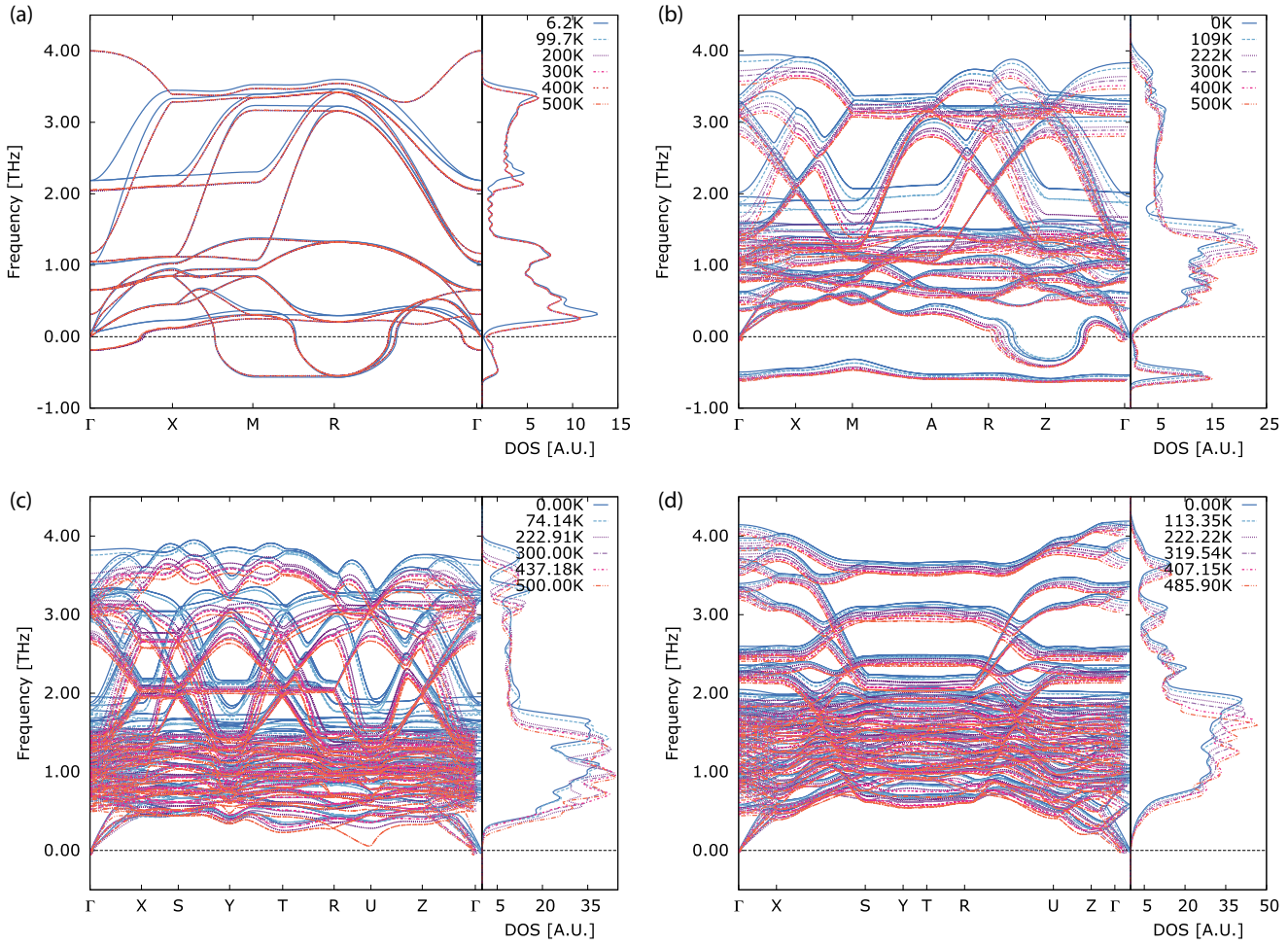

FIG. 4. (Color online) Phonon dispersions and densities of states of the four different polymorphs of $CsSnI_3$, plotted for various lattice temperatures obtained from the quasiharmonic approximation (the corresponding structural parameters are listed in Table V): (a) Bα, (b) Bβ, (c) Bγ, and (d) Y. The unit cell of the Bα phase contains five atoms ($Z = 1$), whereas the Bβ unit cell is twice as large (10 atoms; $Z = 2$), and the the two orthorhombic structures both contain 20 atoms in the primitive cell ($Z = 4$).

C. Phonon density of states and band dispersion

Within the harmonic approximation, Huang and Lambrecht observed imaginary phonon modes in the equilibrium band structures of both high-temperature black phases [7]. Imaginary modes were not observed in the orthorhombic phases (Bγ and Y), indicating that the orthorhombic structures are dynamically stable at 0 K. From the temperature-dependent lattice volumes obtained in the present quasiharmonic calculations, we calculated the phonon band structures and densities of states as a function of temperature (Fig. 4; the corresponding structural parameters are listed in TableV).

As in Ref. [7], we also observe soft modes in the dispersions of the Bα and Bβ phases. In the former, the soft modes occur at the zone boundaries [**q** vectors M and R; Fig. 4(a)]. This would correspond to a phase instability due mostly to rotations of the octahedra about the crystallographic c axis [26]. From the partial phonon density of states (PDOS) of the equilibrium structure (Fig. 5), it can be seen that the main contribution to the soft modes are distortions of the perovskite cage (Sn-I), which is again consistent with the findings in Refs. [1,7]. Moreover, one must note that these zone-boundary imaginary modes do not disappear at high temperatures (above 425 K), indicating that this structure is not dynamically stable at any of the lattice temperatures studied here.

At ∼29 K, a new optic-mode instability emerges at the Γ point, corresponding to a ferroelectric phase transition, which would lead to a higher degree of disorder in the system [26]. This is similar behavior to that observed, for example, in $SrTiO_3$, where the ferroelectric phase transition occurs at low temperatures (∼32 K) [26]. From the low-temperature PDOS curves [Fig. 6(a)], this disorder contribution appears to be due to the vibrations of the Cs atoms about their mean positions, which become more prominent with increasing temperature. The "rattling" motion of the Cs atom would cause the loss of the center of symmetry in the unit cell.

In support of these conclusions, Chung *et al.* [1] found that at 500 K the coordination environment and anisotropic displacement parameters (ADPs) of the Cs atoms were unusually high, and also that the ADPs of the I atoms indicated large thermal vibrations perpendicular to the Sn-I bonds, which is consistent with the distortion of the cage.

From the phonon band dispersion of the Bβ phase [Fig. 4(b)], the soft modes cross the whole of the BZ,

TABLE V. Lattice parameters of the four phases of $CsSnI_3$ at the QHA lattice temperatures at which the phonon DOS and band dispersions in Fig. 4 were obtained.

	T (K)	a_0, b_0, c_0 (Å)		T (K)	a_0, b_0, c_0 (Å)
Bα	6	$a_0 = 6.143$	Bβ	0	$a_0 = 8.622, b_0 = 6.122$
	100	$a_0 = 6.161$		109	$a_0 = 8.652, b_0 = 6.144$
	200	$a_0 = 6.162$		222	$a_0 = 8.695, b_0 = 6.174$
	300	$a_0 = 6.161$		300	$a_0 = 8.720, b_0 = 6.192$
	400	$a_0 = 6.161$		400	$a_0 = 8.745, b_0 = 6.210$
	500	$a_0 = 6.160$		500	$a_0 = 8.762, b_0 = 6.222$
Bγ	0	$a_0 = 8.609, b_0 = 12.264, c_0 = 8.559$	Y	0	$a_0 = 10.297, b_0 = 4.739, c_0 = 17.595$
	74	$a_0 = 8.633, b_0 = 12.299, c_0 = 8.583$		113	$a_0 = 10.333, b_0 = 4.755, c_0 = 17.655$
	223	$a_0 = 8.719, b_0 = 12.421, c_0 = 8.669$		222	$a_0 = 10.384, b_0 = 4.779, c_0 = 17.743$
	300	$a_0 = 8.893, b_0 = 12.410, c_0 = 8.602$		320	$a_0 = 10.436, b_0 = 4.803, c_0 = 17.831$
	437	$a_0 = 8.762, b_0 = 12.482, c_0 = 8.712$		407	$a_0 = 10.487, b_0 = 4.826, c_0 = 17.919$
	500	$a_0 = 8.792, b_0 = 12.525, c_0 = 8.741$		486	$a_0 = 10.836, b_0 = 4.749, c_0 = 17.883$

including the zone center. These soft modes persist across the temperature range studied, similar to those in the Bα phase.

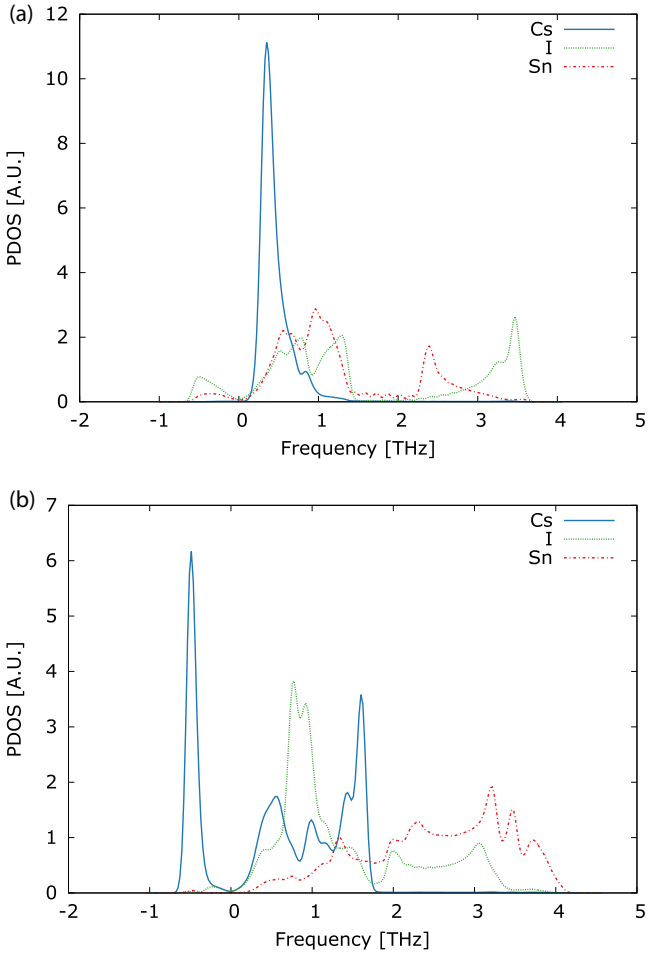

FIG. 5. (Color online) Partial phonon density of states of the Bα (a) and Bβ (b) phases of $CsSnI_3$, calculated at the 0 K equilibrium lattice parameters. It can be seen that distortions of the Sn-I cage are the major contributor to the negative part of the DOS in the Bα phase, whereas the imaginary modes in the Bβ phase are predominantly due to the motion of the caged Cs ion.

In addition, a second branch of imaginary frequencies are visible at the **q** vector Z. This is in contrast to the results in Ref. [7], where only one branch of soft modes was observed, with discontinuities along the segment M-X. We found that

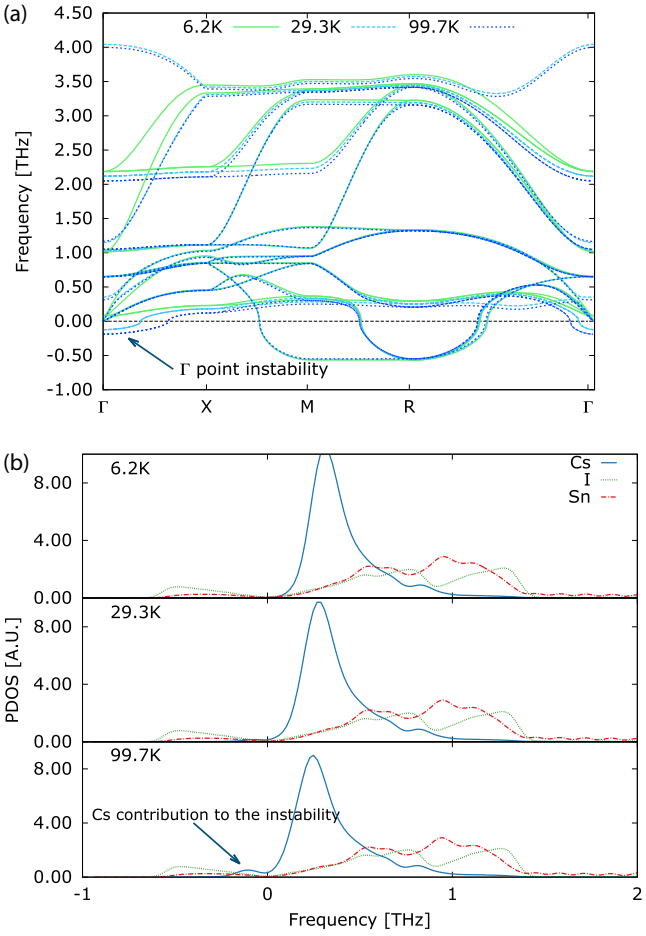

FIG. 6. (Color online) Phonon band dispersion (a) and partial density of states (b) of the Bα polymorph of $CsSnI_3$, at low temperatures. An imaginary optical mode emerges at the Γ point as the temperature increases, which appears to be due predominantly to the "rattling" of the Cs atom within the perovskite cage.

this discrepancy may be due to the different plane-wave cutoff employed in these and the other calculations (see Appendix A). In the PDOS in Fig. 5(b), the main contribution to the negative modes is the rattling of the Cs atom, with the negative-frequency part of the PDOS having a much larger amplitude on Cs than that in the Bα phase [1,7]. This effect is consistent with the instability of this system evident in the Gibbs free energy (Fig. 2), and suggests that, on cooling, structural transitions involving movement of the Cs atoms would occur [26].

The two room-temperature structures (Bγ and Y) do not show imaginary phonons over any of the temperature ranges studied in this work [Figs. 4(c) and 4(d)]. On cooling to the Bγ phase, the Cs atoms order and the structure is stable in the orthorhombic symmetry group. In this system, near 500 K a mode at the U **q** vector appears to undergo substantial softening with respect to lower-temperature structures, whereas the Y phase does not appear to show similar phenomena.

D. Discussion

We have obtained good qualitative agreement with other reports [1,7] in predicting the free-energy ordering of the different polymorphs of $CsSnI_3$, and the finite-temperature lattice parameters/cell volumes obtained from the QHA appear to be in better agreement with experimental data than those of the equilibrium (athermal) structure.

The transition temperatures estimated within the harmonic and quasiharmonic approximations are both relatively poor compared to the experimental data in Ref. [1]; for example, the transition between the Y and high-temperature cubic phases is expected to occur above 425 K, whereas the Helmoltz free-energy comparison predicts this to take place below 200 K, and the Gibbs free energies predict a transition slightly above 100 K (Fig. 2).

As the Bβ phase is not stable on the QHA free-energy landscape, these calculations predict that the Bα structure should transition directly to the Bγ phase. That said, the discrepancies between the calculated and experimentally observed transition temperatures amount to subtle energy differences, and given the apparent instability of the two high-temperature phases evident from their phonon dispersions, it is likely that these are observed as crystallographic averages of equivalent lower-symmetry structures. In this view, the transition temperatures observed experimentally would correspond to those at which sufficient thermal energy was available to allow these low-lying potential-energy maxima to be explored frequently enough to be observable in a diffraction experiment. Indeed, the Helmoltz free energy suggests that the Bα and Bγ structures are very close in energy at temperatures above $\sim$150 K, with the energy difference between them ($\sim$0.02 eV) being comparable to $k_B T$ between 180 and 200 K. Similarly, the Gibbs energy difference between Bα and Bγ is around 0.01 eV between 130 and 160 K, and is roughly constant (0.02 eV) from ($\sim$350 K) to 700 K.

It must be noted that a significant shortcoming of the present investigation is the treatment of the imaginary modes in the two high-temperature polymorphs. A proper physical description of these systems, e.g., using self-consistent phonon theory, should provide renormalized frequencies for the soft (imaginary) modes. In the present calculations, however, the imaginary modes are excluded from the partition function when computing thermodynamic properties, whereas renormalization could produce additional low-frequency modes, which contribute significantly to the free energy. However, on inspection of the bands at explicitly calculated high-symmetry **q** points, we found that in many cases the imaginary modes were doubly or triply degenerate, meaning that an involved renormalization scheme would need to be employed, which is beyond the scope of this study. Aside from this approximation, it is also important to note that the QHA is only considered to be valid up to $\frac{2}{3}$ of the melting temperature [19], above which higher-order anharmonic effects become prominent. We would thus expect the high-temperature properties obtained from the QHA to be in error to some extent, even given an improved scheme for renormalizing the imaginary modes.

V. CONCLUSIONS

We have performed lattice-dynamics calculations within the quasiharmonic approximation on the four polymorphs of $CsSnI_3$. Our calculated structural properties suggest that, on balance, the finite-temperature lattice parameters provide a better match to experimental data than those of the equilibrium structure, despite potential issues with the treatment of

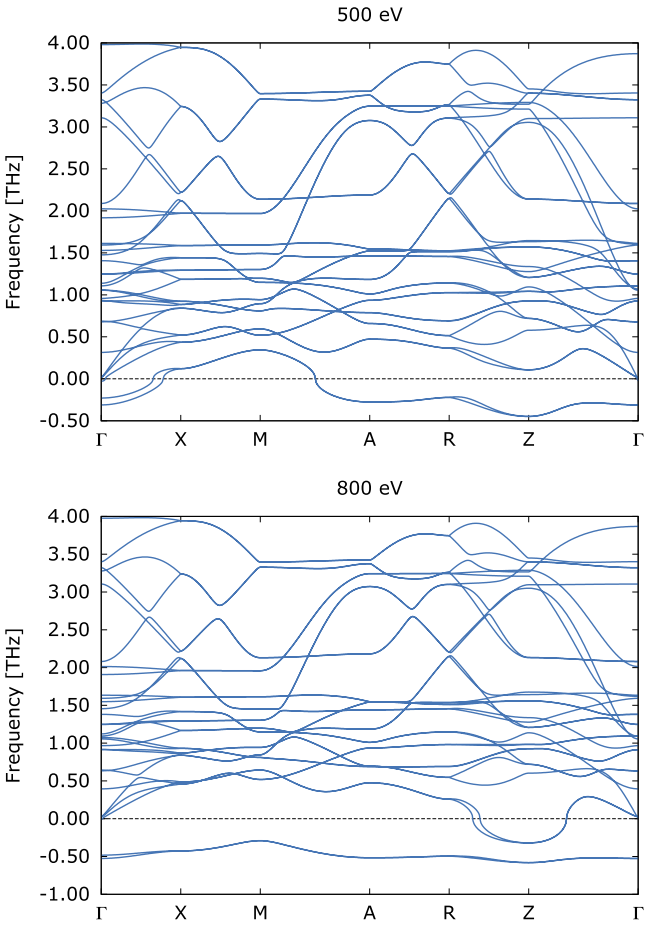

FIG. 7. (Color online) Phonon band dispersions of the Bβ phase of $CsSnI_3$ calculated with plane-wave cutoffs of 500 eV (electronically converged value; top) and 800 eV (bottom).

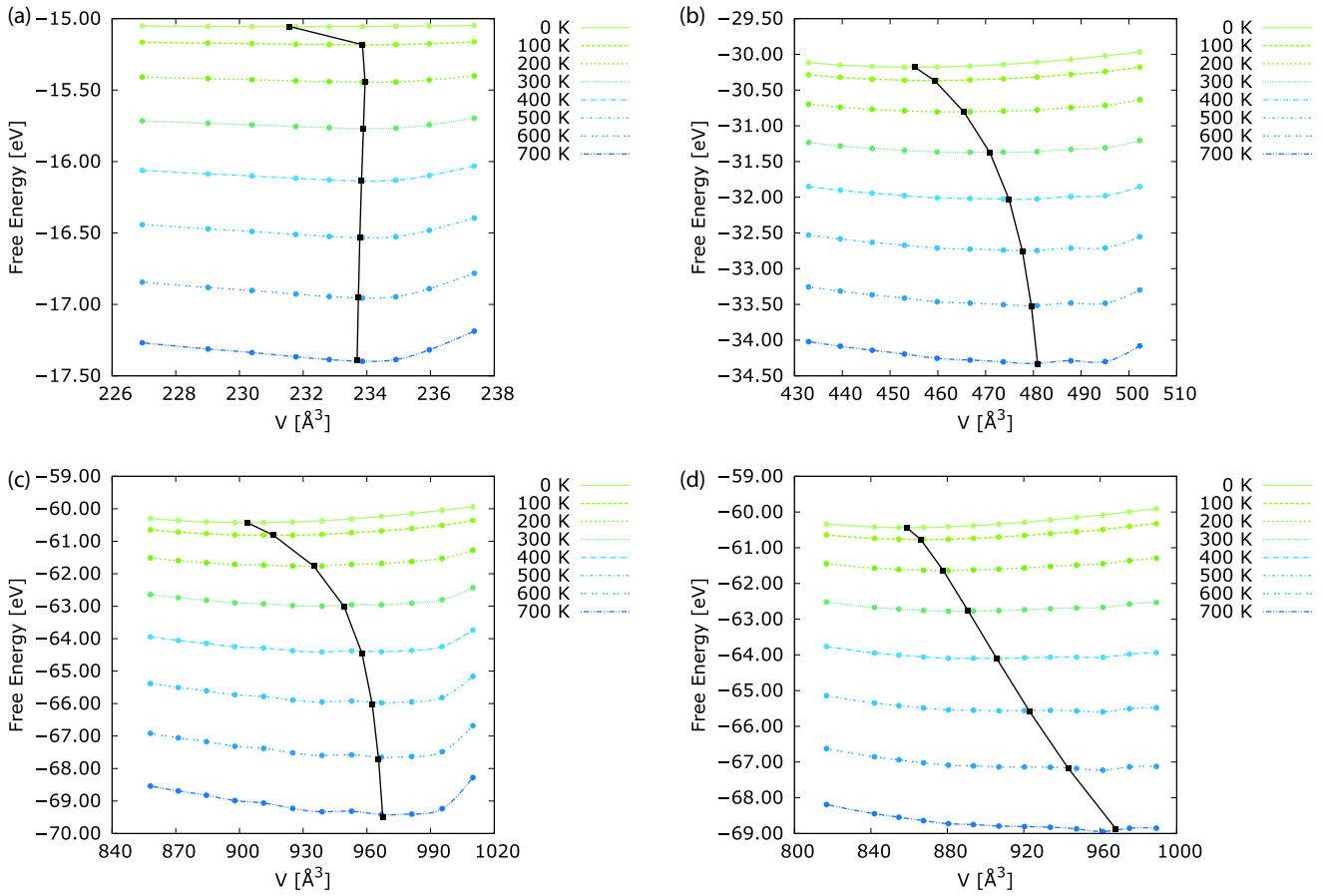

FIG. 8. (Color online) Helmoltz free-energy equation-of-state fits for the four $CsSnI_3$ polymorphs at different lattice temperatures: (a) Bα, (b) Bβ, (c) Bγ, and (d) Y. Note that the free energies are given per unit cell, and not per formula unit.

imaginary modes during the calculation of free energies. On the other hand, the predicted phase-transition temperatures do not agree quantitatively with experimental measurements, and further studies are required to pinpoint the origin of these discrepancies. From both the harmonic Helmholtz and quasiharmonic Gibbs free energies, we conclude that the Bβ phase is not stable between 0 and ∼500 K with respect to competing phases. This is reflected in the calculated temperature-dependent phonon band dispersions, in which a branch of negative modes is consistently observed across the entire Brillouin zone, associated with the "rattling" of the Cs atom within the perovskite cage. The high-symmetry Bα phase also exhibits imaginary phonon modes throughout the temperature range studied, which appear to arise from motion of the Sn-I framework, and also a certain degree of disorder in the Cs atom position, evident from a zone-center ferroelectric instability which emerges at temperatures just above 0 K. On the other hand, both the ground-state phases are found to be structurally and dynamically stable, and do not show negative frequencies in their phonon dispersions up to 500 K. The significance of these findings is that the Bα and Bβ structures may be crystallographic averages over low-frequency modes in the lower-symmetry phases leading to thermal hopping between equivalent minima, and this is a point that merits further experimental and theoretical investigation. Similar behavior is expected for other tin and lead compounds in the perovskite crystal structure.

ACKNOWLEDGMENTS

We thank A. Togo and A. A. Sokol for useful discussions on displacive structural instabilities, and W. R. L. Lambrecht for discussions on $CsSnI_3$. This work is supported by EPSRC Programme Grants (No. EP/K004956/1 and No. EP/K016288/1) and the ERC (Grant No. 277757). We acknowledge use of the ARCHER supercomputer through membership of the UK HPC Materials Chemistry Consortium, which is funded by EPSRC Grant No. EP/L000202, in the completion of this work. The authors also acknowledge computing support from the University of Bath Computing Services, which maintain the Aquila HPC cluster.

APPENDIX A: CONVERGENCE OF THE PHONON DISPERSIONS WITH RESPECT TO THE PLANE-WAVE CUT-OFF ENERGY

When carrying out DFT calculations, convergence testing is typically done based on criteria such as the total energy or stress. In the present work, we found that whereas moderate plane-wave cut-off energies (500 and 600 eV for the high-temperature and ground-state phases, respectively) were sufficient to converge the total energies and stress, a higher cutoff of 800 eV was needed to converge the phonon frequencies, in particular to eliminate artifacts at long **q**-vector regions of the phonon dispersion.

Initial harmonic-phonon calculations carried out with the lower plane-wave cutoffs gave rise to unphysical negative acoustic modes at the Γ point in calculations on the Bγ phase, indicating numerical noise in the force constants (we note that Phonopy does not symmetrize force constants by default, i.e. enforcing the acoustic-sum rule, as is a standard procedure in most codes). This issue was rectified by using a higher cutoff.

In addition, for the Bβ phase we observed differences in the low-frequency phonon modes, most notably the dispersion of the imaginary modes across the BZ, with different cutoffs (Fig. 7). When the lower cutoff was employed, negative frequencies were observed at every high-symmetry **q** vector bar the segment X-M; this is similar to the dispersion reported in Ref. [7]. However, where the energy cutoff was increased to 800 eV, the branch becomes negative through this segment, and a second negative-frequency branch emerges at Z.

APPENDIX B: CALCULATED TEMPERATURE-DEPENDENT LATTICE PARAMETERS

Table V lists the calculated lattice parameters for the different QHA lattice temperatures for which the phonon densities of states and band dispersions are shown in Fig. 4.

APPENDIX C: FREE-ENERGY EQUATIONS OF STATE

In Sec. IV B, apparent artifacts were observed in the calculated high-temperature bulk moduli, in particular those of the cubic Bα phase. On investigation, we found that this was most likely due to anomalies in the high-temperature free-energy equations of state [Fig. 8(a)], in particular a disproportionately sharp increase in the free energy under expansion. Since this phenomenon is not as prominent at low temperature, it is likely due to the treatment of imaginary modes in the present calculations (see Sec. IV D). It is notable that a similar phenomenon is also observed for the ground-state Bγ phase, which we found is due to the appearance of soft modes under lattice expansions corresponding to very high temperatures on the QHA free-energy surface. From the results in Fig. 3(a), the calculated bulk moduli appear to be more sensitive to these issues than the lattice volumes, which, when compared to experimental data, appear to be reasonable for the high-temperature structures.

[1] I. Chung, J.-H. Song, J. Im, J. Androulakis, C. D. Malliakas, H. Li, A. J. Freeman, J. T. Kenney, and M. G. Kanatzidis, J. Am. Chem. Soc. **134**, 8579 (2012).

[2] C. Yu, Y. Ren, Z. Chen, and K. Shum, J. Appl. Phys. **114**, 163505 (2013).

[3] K. Yamada, S. Funabiki, H. Horimoto, T. Matsui, T. Okuda, and S. Ichiba, Chem. Lett. **20**, 801 (1991).

[4] K. Shum, Z. Chen, J. Qureshi, C. Yu, J. J. Wang, W. Pfenninger, N. Vockic, J. Midgley, and J. T. Kenney, Appl. Phys. Lett. **96**, 221903 (2010).

[5] C. J. Howard and H. T. Stokes, Acta Cryst. B **54**, 782 (1998).

[6] A. M. Glazer, Acta Cryst. B **28**, 3384 (1972).

[7] L.-Y. Huang and W. R. L. Lambrecht, Phys. Rev. B **90**, 195201 (2014).

[8] L.-Y. Huang and W. R. L. Lambrecht, Phys. Rev. B **88**, 165203 (2013).

[9] A. Kojima, K. Teshima, Y. Shirai, and T. Miyasaka, J. Am. Chem. Soc. **131**, 6050 (2009).

[10] M. Liu, M. B. Johnston, and H. J. Snaith, Nature (London) **501**, 395 (2013).

[11] J. M. Frost, K. T. Butler, F. Brivio, C. H. Hendon, M. van Schilfgaarde, and A. Walsh, Nano Lett. **14**, 2584 (2014).

[12] F. Brivio, K. T. Butler, A. Walsh, and M. van Schilfgaarde, Phys. Rev. B **89**, 155204 (2014).

[13] A. Walsh, D. O. Scanlon, S. Chen, X. G. Gong, and S.-H. Wei, Angew. Chem., Int. Ed. Engl. **54**, 1791 (2015).

[14] J. M. Frost, K. T. Butler, and A. Walsh, APL Mater. **2**, 081506 (2014).

[15] I. Chung, B. Lee, J. He, R. P. H. Chang, and M. G. Kanatzidis, Nature (London) **485**, 486 (2012).

[16] Hayatullah, G. Murtazab, S. Muhammada, S. Naeemb, M. N. Khalidb, and A. Manzar, Acta Phys. Pol. A **124**, 102 (2013).

[17] M. Sternik and K. Parlinski, J. Chem. Phys. **123**, 204708 (2005).

[18] M. T. Dove, *Structure and Dynamics*, Vol. 12 (Oxford University Press, Oxford, 2003).

[19] J. M. Skelton, S. C. Parker, A. Togo, I. Tanaka, and A. Walsh, Phys. Rev. B **89**, 205203 (2014).

[20] A. Togo, L. Chaput, I. Tanaka, and G. Hug, Phys. Rev. B **81**, 174301 (2010).

[21] K. Parlinski, Z. Q. Li, and Y. Kawazoe, Phys. Rev. Lett. **78**, 4063 (1997).

[22] L. Chaput, A. Togo, I. Tanaka, and G. Hug, Phys. Rev. B **84**, 094302 (2011).

[23] F. D. Murnaghan, Proc. Natl. Acad. Sci. U.S.A. **30**, 244 (1944).

[24] P. Vinet, J. R. Smith, J. Ferrante, and J. H. Rose, Phys. Rev. B **35**, 1945 (1987).

[25] L. H. Rimmer and M. T. Dove, arXiv:1411.7071v1.

[26] M. T. Dove, *Introduction to Lattice Dynamics*, Vol. 8 (Cambridge University Press, Cambridge, 1993).

[27] W. Miller, C. W. Smith, D. S. Mackenzie, and K. E. Evans, J. Mater. Sci. **44**, 5441 (2009).

[28] P. Tschaufeser and S. C. Parker, J. Phys. Chem. **99**, 10609 (1995).

[29] P. Hohenberg and W. Kohn, Phys. Rev. **136**, B864 (1964).

[30] W. Kohn and L. Sham, Phys. Rev. **140**, A1133 (1965).

[31] G. Kresse and J. Furthmüller, Phys. Rev. B **54**, 11169 (1996).

[32] G. Kresse and J. Hafner, Phys. Rev. B **47**, R558 (1993).

[33] G. Kresse and J. Furthmüller, Comput. Mat. Sci. **6**, 15 (1996).

[34] J. P. Perdew, A. Ruzsinszky, G. I. Csonka, O. A. Vydrov, G. E. Scuseria, L. A. Constantin, X. Zhou, and K. Burke, Phys. Rev. Lett. **100**, 136406 (2008).

[35] J. P. Perdew, A. Ruzsinszky, G. I. Csonka, O. A. Vydrov, G. E. Scuseria, L. A. Constantin, X. Zhou, and K. Burke, Phys. Rev. Lett. **102**, 039902(E) (2009).

[36] G. Kresse and D. Joubert, Phys. Rev. B **59**, 1758 (1999).

[37] P. E. Blöchl, Phys. Rev. B **50**, 17953 (1994).

[38] H. J. Monkhorst and J. D. Pack, Phys. Rev. B **13**, 5188 (1976).

[39] F. Birch, Phys. Rev. **71**, 809 (1947).

[40] R. W. G. Wycoff, *Crystal Structures 1*, 2nd ed. (Interscience Publishers, New York, 1963).
[41] A. Togo, F. Oba, and I. Tanaka, Phys. Rev. B **78**, 134106 (2008).
[42] A. Togo, L. Chaput, and I. Tanaka, Phys. Rev. B **91**, 094306 (2015).
[43] P. Y. Yu and M. Cardona, *Fundamentals of Semiconductors: Physics and Materials Properties* (Springer-Verlag, Berlin, 1996), p. 104.
[44] M. Gajdoš, K. Hummer, G. Kresse, J. Furthmüller, and F. Bechstedt, Phys. Rev. B **73**, 045112 (2006).
[45] L. Topor, A. Navrotsky, Y. Zhao, and D. J. Weidner, J. Solid State Chem. **132**, 131 (1997).
[46] V. M. Goldschmidt, Naturwissenschaftenen **14**, 477 (1926).
[47] R. D. Shannon, Acta Cryst. A **32**, 751 (1976).
[48] Y. Zhao and D. J. Weidner, Phys. Chem. Miner. **18**, 294 (1991).

3.2 Comments to the Manuscript Phase Stability and Transformations in the Halide Perovskite $CsSnI_3$

- Page 144107-3, paragraph 4: Rephrasing sentence 'To perform a QHA calculation, the free energies are computed for a range of expansions and compressions about the equilibrium volume (the ion positions are relaxed for all the volumes). The free energies are then fitted, as a function of temperature, to the Vinet-Rose equation of state [102, 83]. From this approach, the equilibrium volume, bulk modulus, and Gibbs free energy can be obtained at arbitrary temperatures.'

- Page 144107-5, paragraph 2: Remove sentence 'This highlights the importance of taking into account contributions beyond the lattice internal energy when assessing polymorph stability.'

- Page 144107-6, paragraph 1: Remove sentence 'There is a disproportionate distortion of the high-temperature free energy of the expanded strauctures due to the presence of the imaginary modes in the phonon density of states'

- Page 144107-7, paragraph 1: Rephrasing sentence 'Within the harmonic approximation, Huang and Lambrecht [7] observed imaginary modes in both band structures of the cubic and tetragonal phases [7].

- Page 144107-7, paragraph 2: Rephrasing sentence 'Moreover, one must note that these zone-boundary imaginary modes do not disappear above the expected transition temperature (425 K). This indicates that the cubic structure in not dynamically stable at any of the studied temperatures.'

- Page 144107-9, paragraph 3: Rephrasing sentence '(..) experimental data in Ref. [1]. The transition between the ground-state Y phase and the high-temperature cubic phase is expected to occur above 425 K. From the harmonic approximation (Helmholtz free energy) the transition takes place below 200 K, while within the quasi-harmonic approximation (Gibbs free energy) the phase transition is predicted to occur slightly above 100 K (Fig. 2).

- Page 144107-9, paragraph 4: Grammer correction of 'Helmholtz'.

- Page 144107-9, paragraph 5: Rephrasing sentence '(..) imaginary modes are not considered in the evaluation of the partition function when computing thermodynamic properties, (..).'

3.3 Symmetry-Mode Analysis

Based on group-theoretical analysis it is possible to define the group-subgroup relationships among the fifteen possible space-groups resulting from octahedral tilting [101]. The majority of low-symmetry perovskite phases can be derived from the high-symmetry structure by rigid tilting of the octahedral units around their symmetry axes. The structural distortions that relate both structures can be qualified as a symmetry-breaking distortion [103]. The equilibrium position of the Cs cation can therefore be determined by the positions and tilting of the SnI_6 octahedra for a given set of bond angles.

By employing symmetry-mode analysis, it is possible to fully describe the distorted ground-state *Pnma* structure by decomposing the structural distortion into contributions from lattice modes with different symmetries. These are characterised by the irreducible representations (ir.reps.) of the centrosymmetric $Pm\bar{3}m$ structure (the reference structure is also known as the aristotype structure). The analysis is performed using the AMPLIMODES programme [104] of the Bilbao Crystallographic Server, and is useful to determine the driving mechanisms of the structural phase transitions and the fundamental instabilities at the origin of the distorted phases.

By providing the high- and low- symmetry structures, the software package AMPLIMODES [104] performs atom mappings (pairings) by identifying the atoms in the low symmetry structure that correspond to the asymetric unit of the reference structure, and therefore computing the atomic displacements that relates both structures. With this approach, it is then possible to define a basis of symmetry-adapted modes and calculate the amplitudes and polarisation vectors from the high-symmetry to the distorted structure [104, 103, 105].

Table 3.1: Summary of the basis modes in the distortion of $CsSnI_3$, from the $Pm\bar{3}m$ to the *Pnma* phase, distributed per type of Wyckoff position (WP). Numbers in parenthesis indicate the number of modes for each ir.rep..

Atoms	WP	Modes
I_3	$3c$	$R_4^-(1)$, $R_5^-(1)$, $X_5^-(1)$, $M_2^+(1)$, $M_3^+(1)$
Cs_1	$1a$	$R_4^-(1)$, $X_5^-(1)$

Tab. 3.1 presents a summary of the basis of symmetry modes and respective ir.reps. which describe the atomic displacements in each Wycoff orbit of the high symmetry phase [103]. There are a total number of seven basis modes, one corresponding to each of the three ir.rep. modes: R_5^-, M_2^+ and M_3^+, and two to ir.reps R_4^- and X_5^-. The single modes of R_5^-, M_2^+ and M_3^+ only correspond to displacements of the I_3 atom, wheres the remaining two also refer to displacements of the Cs cation. The atomic displacements of all atoms, multiplied by a given amplitude, yields the actual distortion of the low-symmetry structure [103].

Table 3.2: Mode decomposition, indicating the amplitudes (Å) of each ir.rep. distortion component.

k-vector	Ir.rep.	Direction	Isotropy Subgroup	Dimension	Amplitude
$(\frac{1}{2},\frac{1}{2},\frac{1}{2})$	R_4^-	(0,a,a)	$Imma$ (74)	2	0.4193
$(\frac{1}{2},\frac{1}{2},\frac{1}{2})$	R_5^-	(0,a,$-a$)	$Imma$ (74)	1	1.4885
$(0,\frac{1}{2},0)$	X_5^-	(0,0,a),(0,0,0)	$Cmcm$ (63)	2	1.1791
$(\frac{1}{2},\frac{1}{2},0)$	M_2^+	(a,0,0)	$P4/mbm$ (127)	1	1.7058
$(\frac{1}{2},\frac{1}{2},0)$	M_3^+	(a,0,0)	$P4/mbm$ (127)	1	0.0706

Tab. 3.2 summarises the mode decomposition, which lists the ir.reps involved in the $Pm\bar{3}m \rightarrow Pnma$ distortion and the absolute amplitudes of the symmetry components of the global distortion. From left to right, the table lists 1) the **k** wave-vector for each ir.rep. present in the distortion; 2) the restricted direction of the ir.rep. space; 3) the isotropy sub-group; 4) the dimension of the respective space-group (number of orthonormal basis-modes); and 5) the amplitudes of the symmetry components. By analysing Tab. 3.1, one may observe that the modes with highest amplitudes are the M_2^+, R_5^- and X_5^- modes, with values of $Q_{M_2^+} = 1.71$ Å, $Q_{R_5^-} = 1.49$ Å and $Q_{X_5^-} = 1.18$ Å, respectively. These modes are therefore major contributors to the distortion to the low symmetry phase. By analysing Figs. 3-1 and 3-2, it is possible to deduce that the M_2^+ and R_5^- ir.reps correspond to in-phase and out-of-phase rotations of the perovskite cage, respectively, whereas ir.rep. X_5^- corresponds to the rattling of the Cs ion inside the cage.

Fig. 3-3 shows the five ir.rep. distortion components that contribute to the symmetry-breaking during the $Pm\bar{3}m \rightarrow Pnma$ distortion. By performing the analysis of structure relations between two phases of the same compound with group-subgroup related space groups, it is possible to construct family trees of homeotypic crystal structures (Bärnighausen trees) [105]. From this analysis one may then perform the decomposition of the global distortion into symmetry-mode contributions, separating the correlated atomic displacements into the main modes which contribute the most for the phase transition [105].

It can be observed that a single ir.rep. distortion component is not sufficient to allow for the full structural distortion from the reference cubic structure to the ground-state $Pnma$ structure. In fact, it is a combination of at least three distortions with significant amplitudes (M_2^+, R_5^- and X_5^-) that cause the symmetry-breaking. Each primary mode condenses at different temperatures, which would correspond to two distinct phase transitions (expected transition sequence of $Pm\bar{3}m \rightarrow P4/mbm \rightarrow Pnma$). These results are consistent with what has been discussed in Refs. [99, 16] and in the previous section.

Fig. 3-4 represents the potential energy surface along each distortion mode (frozen mode). The end-point $u = 0$ corresponds to the high-symmetry $Pm\bar{3}m$ structure and $u = 1$ represents

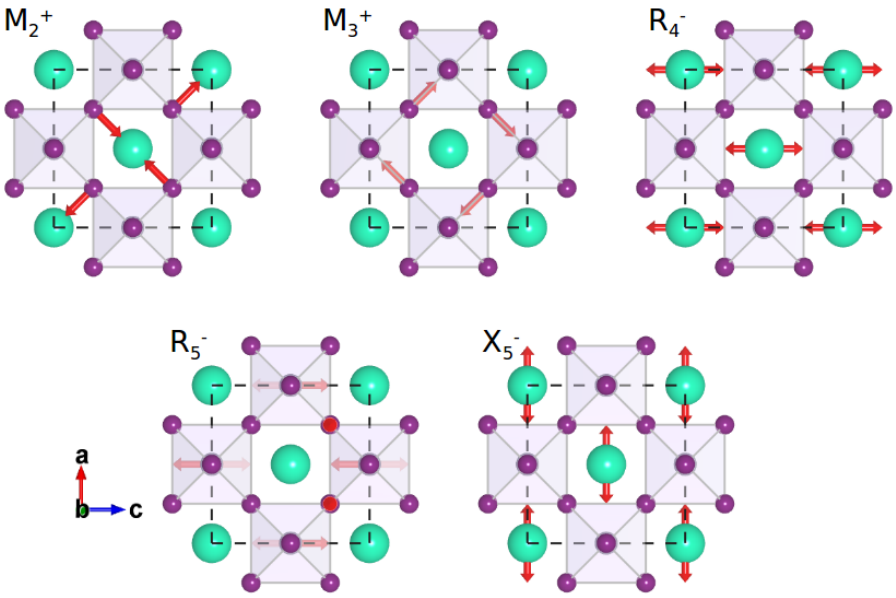

Figure 3-1: Illustration of the different distortion components describing the $Pm\bar{3}m \rightarrow Pnma$ transition in $CsSnI_3$. The directions of the atomic displacements are shown by arrows. The lengths of the arrows do not correspond to the amplitude distortions listed in Tab. 3.2, but have been increased to clearly show the atomic displacements. The I ions are represented in purple and the Cs ion in green.

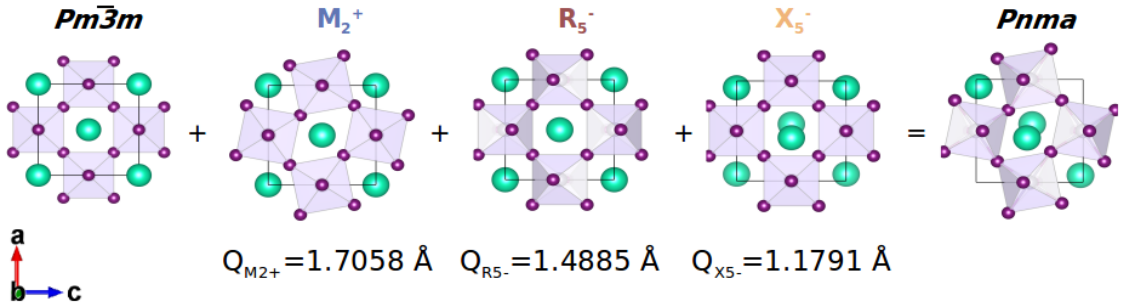

Figure 3-2: Decomposition of the structural distortion from $Pm\bar{3}m \rightarrow Pnma$ into contributions from lattice modes with different symmetries. The distorted structure derives from the high-symmetry structure through three frozen distortions, M_2^+, R_5^- and X_5^-. The I ions are shown in purple and the Cs in green.

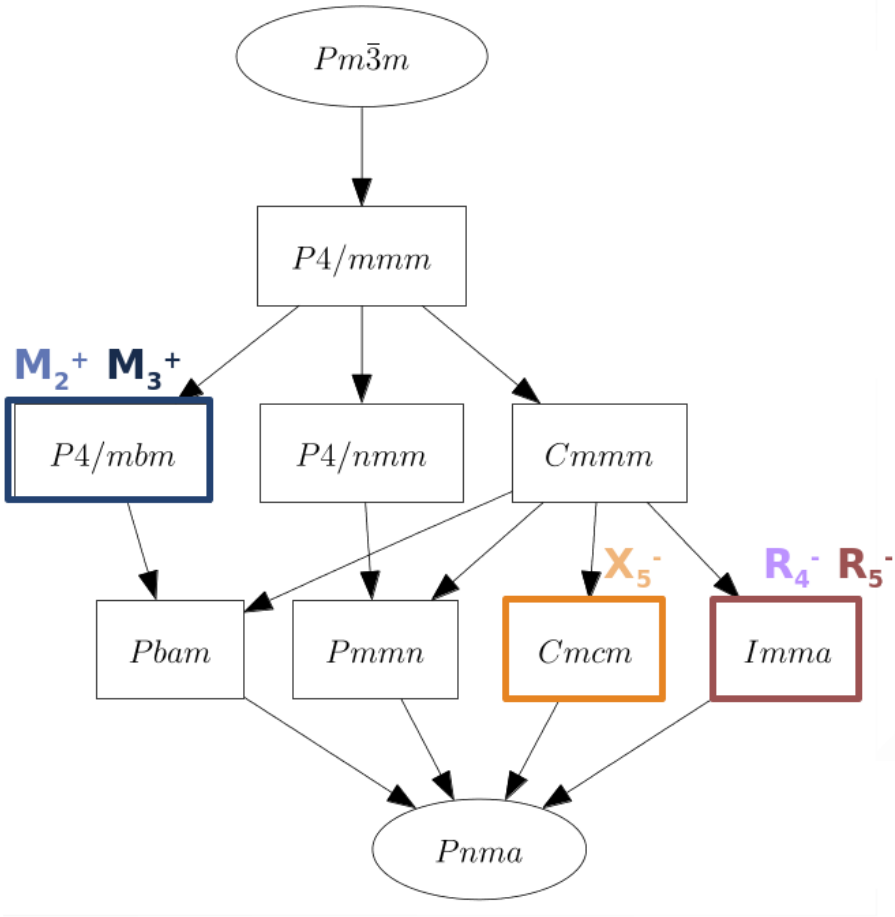

Figure 3-3: Bärnighausen tree for the group-subgroup relationship between the cubic aristotype and *Pnma* ground-state $CsSnI_3$ structures. The ir.rep. labels indicate the distortion components and related isotropy group that contribute to the symmetry-breaking of $Pm\bar{3}m \rightarrow Pnma$. The labels M_2^+, M_3^+, R_4^-, R_5^- and X_5^- correspond to the wave-vectors in the Brillouin zone listed in Tab. 3.2, for each symmetry mode. The graph was obtained using the SYMMODES software [11, 12].

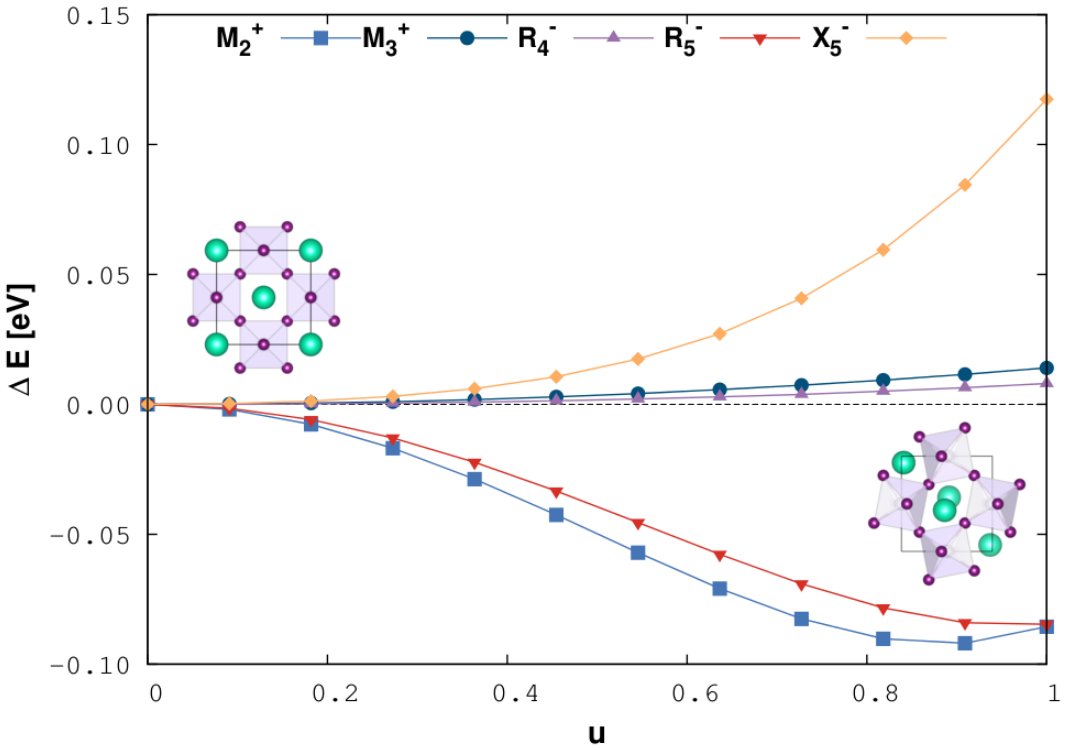

Figure 3-4: Potential energy surface along each distortion mode, with $u = 0$ being the centrosymmetric cubic structure and $u = 1$ the distortion structure corresponding to the isotropy sub-group of the frozen mode. All the five distortion modes contribute to the $Pnma$ distortion, although the most significant are the M_2^+, R_5^- and X_5^-.

the distortion corresponding to the isotropy sub-group of the respective frozen mode (i.e.: $u = 1$ for the M_2^+ corresponds to the $P4/mbm$ sub-group). The sum of all the five different $u = 1$ end-points will agree with the ground-state $Pnma$ symmetry. It can be observed that the energy lowers considerably along the M_2^+ and R_5^- modes, which means that these distortions are mainly responsible for the symmetry-lowering to the $Pnma$ phase. This corresponds to what was discussed above, and to these modes contributing with more weight to the distortion ($Q_{M_2^+} = 1.71$ Å and $Q_{R_5^-} = 1.49$ Å). The X_5^- mode, which refers to the rattling of the Cs atom, produces an increase in energy when the frozen distortion occurs. In combination with the other distortions of the surrounding cage the Cs movement leads to an averaged reduction in energy of the $CsSnI_3$ system.

Chapter 4

Germanium Telluride (GeTe)

(...)what would be the use of studying physics if the mysteries were not the most important things to investigate.
Richard P. Feynman

GeTe is a typical Ferroelectric Rashba Semi-Conductor (FERSC), displaying a ground-state ferroelectric polar structure with spin-orbit effects, that give rise to the Rashba splitting of the electronic bands. This material is quite intriguing since it does not fall into the classes of conventional ferroelectrics. The polarisation in GeTe persists with the thickness of the order of several nanometers, where it is even possible to reverse the orientation of the polarisation by swapping of short and long Ge-Te bonds in the polar structure [106].

GeTe exhibits a high-temperature cubic rocksalt phase and a low-temperature ferroelectric rhombohedral phase. The phase-transition between the two phases occurs between 625-705 K [107, 108, 109]. To study the nature of the structural phase transition, we have carried out lattice dynamics calculations. We used the quasi-harmonic approximation, to model the temperature dependence of the properties and to obtain the free energies and phonon dispersions of the two phases. These calculations revealed that the disorder is not static, and that the local symmetry breaking would be caused by the displacement of the cation, which easily transitions back and forth between two local minima, corresponding to the $R3m$ structure.

From a microscopic point of view, the application of relativistic many-body perturbation theory may allow for a more complete understanding of the electronic properties of the system, enabling the study of the spin-electronic phenomena through the distortion pathway. From the conclusions drawn from the lattice dynamics, one would also assume that the Rashba-splitting is dynamical, since the local symmetry breaking would drive the splitting of the spin-bands. Similar conclusions also apply to the crystal-field splitting. These results are consistent with experimental evidence that the transition between the two phases in GeTe involves a type of order-disorder transition of distorted units and is not displacive.

To analyse the mechanism of ferroelectric transitions, one needs to integrate interpretations from a macroscopic perspective, such as phenomenological Landau theories, to address the issue of hysteresis behaviour. We have also carried this out, by employing the theoretical methodology reported in Ref. [91], where the electric equation of state has been implemented, making it possible to study the evolution of the order parameter (polarisation) through the paraelectric-to-ferrolectric phase transition.

The first part of the work consists of a detailed discussion of the phase transition, from the paraelectric to ferroelectric structure, and the variation of the Rashba effect and crystal-field splitting according to the distortion path. The second part discusses the effective masses of the band edges with the Rashba-splitting, the dielectric constants and the Born-effective charges. The third part concludes with the application of the Landau free energy (electric equation of state) to probe the thermodynamics of the phase transition in GeTe.

4.1 Lattice Dynamics of the Rashba Effect in GeTe

The paper that follows details the work carried out mostly during the second year of the PhD, and some part of the third year. For this work, knowledge of lattice dynamics acquired during the first year of the PhD was applied to study the phase transition of GeTe. Since interest was mostly considered for the ground-state phase, which exhibits ferroelectric properties and the Rashba-splitting, more deep understanding of respective properties were required. For such, assimilating skills based on many-body perturbation methods were essential in order to calculate the relativistic band structures, and other properties derived from these effects. This phase was carried out in collaboration with researchers from King's College of London who provided the preliminary support for using the Questaal code to perform QSGW calculations.

Influence of Lattice Dynamics on the Rashba Effect in GeTe

E. Lora da Silva,[1] S. McKechnie,[2] M. van Schilfgaarde,[2] J. M. Skelton,[1] S. C. Parker,[1] and A. Walsh[3,4]

[1]*Department of Chemistry, University of Bath, Bath BA2 7AY, United Kingdom*
[2]*Department of Physics, Kings College London, London WC2R 2LS, United Kingdom*
[3]*Department of Materials Science and Engineering, Yonsei University, Seoul 03722, Korea*
[4]*Department of Materials, Imperial College of London, London SW7-2AZ, United Kingdom**

(Dated: July 18, 2018)

Abstract

At room temperature, GeTe adopts a polar α-phase ($R3m$), but transitions to a centrosymmetric rocksalt β-phase ($Fm\bar{3}m$) above 670 K. The material is an example of a ferroelectric Rashba semiconductor (FERSC), where the combination of lattice polarization and spin-orbit coupling results in a spin splitting at the valence- and conduction-band extrema. We probe how these effects evolve through the α to β phase transition using a combination of first-principles lattice-dynamics and electronic-structure techniques. The quasi-harmonic approximation (QHA) is used to explore the temperature dependence of the structure and properties, with explicit mapping of the anharmonic potential-energy surface used to explore the double-well phonon instability associated with the β phase. The magnitude of the Rashba splitting is quantified using all-electron relativistic quasi-particle self-consistent GW (QSGW) theory. While the change in spontaneous polarization shows a quadratic relationship to the lattice distortion, the Rashba splitting shows a more complex response. We further predict that β-GeTe may exhibit a dynamic Rashba effect due to local symmetry-breaking distortions at high temperature.

I. INTRODUCTION

Ferroelectric materials usually undergo a phase transition from a high-temperature paraelectric phase to a low-temperature polar phase. The emergence of spontaneous polarization is a consequence of the symmetry-breaking structural transition that takes place at the transition temperature, T_{C}.

The discovery of novel physical properties in materials science is often driven by the goal of finding materials that couple multiple functionalities (i.e. are multifunctional), which can provide opportunities for new and improved technological applications. A good example are the subset of ferroelectrics materials identified as ferroelectric Rashba semiconductors (FERSC).[1] These simultaneously display spontaneous polarization (ferroelectricity) and spin-orbit coupling (SOC) effects, and the resulting relativistic electronic structure can display the Rashba effect - a momentum-dependent splitting of spin bands.

GeTe is a prototypical FERSC material. It is simple in structure,[1] with only two atoms in the primitive unit cells of both the low-temperature α ($R3m$) and high-temperature β ($Fm\bar{3}m$) phases. The α and β phases are linked by a displacement of the Ge atom by 0.02 Å along the $< 111 >$ while retaining the cubic cell parameters, which removes the center of symmetry and allows for spontaneous polarization. The phase transition occurs around 625–705 K.[2–4]

Although the ferroelectric phase of GeTe is well characterized, the paraelectric-to-ferroelectric phase transition is not fully understood. In particular, different studies question whether the transition is displacive or order-disorder in nature, the answer to which relies on the balance between the dynamics of the phase transition and the role of anharmonic (*soft*) phonon modes.[5] While for displacive phase transitions the behaviour of the crystal is well described within the soft-mode theory,[41] with the transition involving small symmetry-breaking displacements; order-disorder transitions are mostly related to ions hopping between sites that differ from the high-symmetry sites, and the transition involves ordering of all the ions.[41] Several studies agree that the phase transition of GeTe is displacive, including the analysis of neutron-diffraction data, which shows a temperature-induced volume contraction at the phase transition,[6,7], and Raman spectroscopy, which shows a softening of the phonon frequencies with increasing temperature.[8] Resonant ultrasound spectroscopy has revealed large strains at the phase transition, which result from optic-mode softening and a Peierls distortion.[9] However, despite the evidence of a displacive transition, the magnitude of the softening is consistent with an order-disorder configurational component.[9] Strain analysis of the cubic-to-rhombohedral transition shows a weakly first-order character,[9] which is consistent with evidence for latent heat in the phase transition from differential thermal analysis.[8]

From a theoretical perspective, density-functional theory (DFT) phonon calculations and symmetry arguments have suggested that the rhombohedral-to-cubic phase transition is displacive.[5] It has been argued that the transition is driven by the condensation of three components of the triply-degenerate $T_{1\mathrm{u}}$ transverse Γ_4^- soft optic mode at the Brillouin zone-center ($\mathbf{q}$ = 0,0,0). When the mode condenses, the center of symmetry in the cubic structure is broken, inducing spontaneous polarization along the trigonal ($< 111 >$) axis.[5]

It has also been argued that the use of experimental techniques that probe the average structure, e.g. Raman scattering and Bragg diffraction, lead to misleading conclusions regarding the nature of the phase change.[10] By employing other techniques to gather information about the local structure, such as total scattering and pair-distribution function (PDF) analysis, it

has been shown that the phase transition shows evidence of order-disorder behavior.[11] This interpretation is based on the existence of two different Ge-Te bond lengths even above the critical temperature, indicating that the local distortions in the low-temperature phase do not disappear at the transition temperature. Also, extended x-ray-absorption fine structure (EXAFS) spectroscopy, which directly probes changes in the Ge-Te bond length with characteristic time measurement times on the order of 10^{-15} s, argues for an order-disorder rather than displacive phase transtion.[10] These results demonstrate that the structure retains the local geometry of the low-temperature above T_C. The fact that GeTe becomes paraelectric at the macroscopic scale implies that the local distortions become stochastic and uncorrelated above T_C. The observation that the local Peierls distortion persists up to the melting temperature led to the conclusion that the transition involves order-disorder behavior of distorted units.[9]

Other theoretical studies suggest the existence of two competing instabilities for GeTe: the structural distortion from the paraelectric-to-ferroelectric phase, and a metal-to-insulator transition.[12] Large values of Born-effective charges are generally considered reliable indicators of the tendency of an insulator towards a ferroelectric instability. However, the effective charges are strongly influenced by proximity to metallicity and by strong electron correlation. The centrosymmetric phase of GeTe displays anomalously-large Born-effective charges, which should result in large frequency splitting between the longitudinal and transverse optical phonons (LO-TO splitting) at the zone-centre .[12] However, there is considerable debate as to whether optic-mode separation at the zone-center would be visible, since the LO–TO splitting would vanish in a metallic phase due to screening of long-range electrostatic fields by carriers.[12,13]

The present study of GeTe consists of two principal sections. The first part uses lattice-dynamics calculations to probe the structural instabilities associated with the paraelectric-to-ferroelectric phase transition, by employing the quasi-harmonic approximation (QHA). The second part investigates the Rashba and crystal-field splitting along the distortion pathway from the cubic to the rhombohedral phase. These latter calculations are done using all-electron relativistic quasi-particle self-consistent GW (QSGW) theory to obtain highly accurate results.

II. THEORETICAL METHODS

To compute the interatomic force constants, calculations were performed within the pesudopotential plane-wave DFT[14,15] framework implemented in the Vienna *Ab-initio* Simulation Package (VASP) code.[16–18] The semi-local generalized-gradient approximation functional with the Perdew-Burke-Ernzerhof parametrization revised for solids (PBEsol)[19,20] was employed for all calculations. Projector augmented-wave (PAW)[21,22] pseudopotentials were used to treat semi-core electronic states.

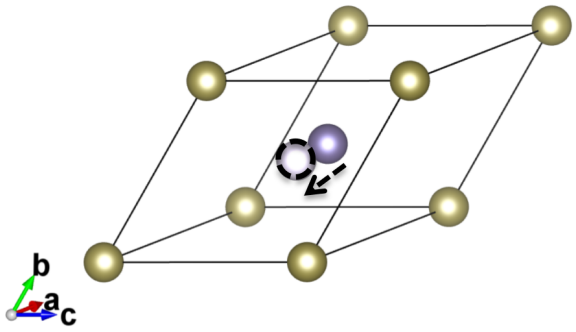

FIG. 1. Primitive unit cell of β-GeTe ($Fm\bar{3}m$), with the Ge cation (dark purple) at $(\frac{1}{2},\frac{1}{2},\frac{1}{2})$ and the Te anion (yellow) at $(0,0,0)$. The distorted α ($R3m$) phase is obtained by displacing the Ge ion in the $<111>$ direction to $(0.48,0.48,0.48)$ (light purple with black dashed outline).

The starting point for our calculations was a full structural relaxation of the two phases, performed with a plane-wave kinetic-energy cut-off of 800 eV. Such a high cut-off was found to be necessary to fully converge the phonon dispersion curves, as discussed in Ref. 23. The electronic Brillouin zone (BZ) of both phases was sampled with a Γ-centred Monkhorst-Pack mesh[24] with 10×10×10 subdivisions.

The theoretical background to harmonic and quasi-harmonic lattice-dynamics calculations is presented in Refs. 23 and 25. In the harmonic approximation (HA), the equilibrium distance between atoms is independent of the thermodynamic temperature, and anharmonic effects are thus required to account for thermal expansion. We employ the quasi-harmonic approximation (QHA), in which the thermal expansion of the crystal lattice is obtained from the volume dependence of the phonon frequencies. To perform a QHA calculation, the phonon frequencies are calculated for a range of expansions and compressions about the 0 K equilibrium volume, and the constant-volume (Helmholtz) free energy for each calculation is evaluated as a function of temperature. The equilibrium volume, bulk modulus and Gibbs free energy can then be obtained at arbitrary temperature by fitting the free energy as a function of volume to an appropriate equation of state.[26,27]

Lattice-dynamics calculations were performed using the supercell finite-displacement method implemented in the Phonopy software package,[28] with VASP used as the force calculator.[29]

Convergence of the phonon supercell size was carried out against 2×2×2, 4×4×4 and 6×6×6 expansions of the primitive cell, and it was found that the 4×4×4 supercell was sufficient to obtain a good representation of the phonon density-of-states and band-structures. For both phases, the phonon frequencies were sampled on an in-

terpolated 48×48×48 **q**-point mesh when evaluating the phonon density of states (DoS) and vibrational internal energy and entropy.

To correct for long-range Coulomb interactions (LO-TO splitting), a non-analytical correction (NAC), using the Born effective-charge tensors and the electronic-polarization component of the macroscopic static dielectric tensor, was applied.[12,30] These quantities were obtained using the density-functional perturbation theory (DFPT) method implemented in VASP.[31] These calculations were performed on the unit-cells of the two structures, and convergence of both quantities necessitated increasing the k-point mesh to 30×30×30 subdivisions for both phases, due to the narrow band-gap of GeTe.

The macroscopic polarization was calculated by employing the Berry phase methodology,[32,33]. Calculations were performed with the screened hybrid functional of Heyd, Scuseria, and Ernzerhof (HSE06) to accurately reproduce the small band-gap, in particular in the high-symmetry β phase.[34,35] The energy cut-off was reduced to 700 eV, and the k-point mesh to 6×6×6 subdivisions.

To provide quantitative electronic-structure information, in particular on the relativistic Rashba splitting, further calculations were performed using the QSGW[36,37] method, as implemented in the Questaal (formerly LMSuite) package.[38] DFT calculations using the local-density approximation (LDA) functional (Barth-Hedin parametrization[39]) were performed alongside QSGW calculations to evaluate the electronic band structure. Extended local orbitals were included in the basis sets for Ge and Te, in order to capture more semi-core states than with the defaults.

For the DFT-LDA calculations, the BZ was sampled using the tetrahedron method[40] and a sampling mesh with 12×12×12 subdivisions, which was reduced to a 6×6×6 mesh for the GW calculations. The plane-wave cut-off for the interstitial charge density (GMAX) was defined with a 9.1 Ry cut-off radius. For the QSGW calculation the G-vector cut-offs for the interstitial part of the eigenfunctions and the Coulomb interaction matrix were set to 6.0 and 5.4 Ry, respectively.

III. RESULTS

A. Lattice Dynamics

The phonon dispersion of the cubic and rhombohedral phases of GeTe are shown in Fig. 2. The QHA associates lattice volumes to thermodynamic temperatures, and thus allows the temperature dependence of the dispersion to be evaluated to this level of approximation.

The dispersion has six phonon branches ($3N$, where N = 2 is the number of atoms in the primitive cell), which are divided into three acoustic and three optic modes. The acoustic branch is triply degenerate at the Γ-point with ω = 0 THz, as expected. In the high-temperature β-GeTe structure, the two transverse optic (TO) modes are imaginary at Γ (Fig. 2.b), indicative of a ferrolectric instability.[12,13,41] A large splitting of the longitudinal and transverse optical modes is also evident and is of the order of 5.74 THz. This feature is alos an indicator of a ferroelectric structural instability, as argued in Ref. 12. The degenerate X-point TO modes soften gradually with temperature, and become imaginary at $T > 498$ K. This observation supports the findings in Ref. 5, where the authors calculated the phonon band-structure of cubic GeTe for a lattice constant measured above T_C. Since the imaginary modes at X are higher in frequency, they are not active in driving the paraelectric-to-ferroelectric phase transition.[5]

Within the QHA, the cubic structure remains dynamically unstable throughout the range of temperatures covered by our volume expansions, and the imaginary modes do not stiffen at high T. As noted above, this is consistent with the high-temperature phase being a crystallographic average of thermal hopping between equivalent distorted local minima. These results are similar to our previous work on the inorganic perovskite $CsSnI_3$, where the two high-temperature phases (cubic and tetragonal) were found to be crystallographic averages over the low-energy minima separating equivalent orthorhombic phases,[23] which is supported by direct measurements of the local structure in the high-temperature phase.[42,43]

In contrast, for the rhombohedral phase (Fig. 2.a), no imaginary frequencies are observed in any of the calculated dispersion curves, evidencing dynamical stability across the range of temperatures studied. This is consistent with rhombohedral phase being the ground-state structure for GeTe.

B. Free Energy

The relative free energies of the two phases (i.e. the combination of DFT internal energy with the harmonic or quasi-harmonic vibrational internal energy and entropy) are shown in Fig. 2.d. The harmonic constant-volume (Helmholtz) energies predict the phase transition to occur at T = 615 K, whereas the quasi-harmonic (Gibbs) energies predict the transition to occur at T = 325 K. Experimentally, it has been evidenced that the phase transition occurs between the range of 625–705 K,[3,4] and thus, the harmonic calculation is apparently in better agreement with the experimental observations. We ascribe this to the fact that neither the harmonic nor quasi-harmonic approximations account for the influence of the soft modes in the cubic phase on the free energy, both directly and indirectly *via* their effect on the frequencies of orthogonal modes, a deficiency which is amplified by the sensitivity of the volume to the free energy in the latter.

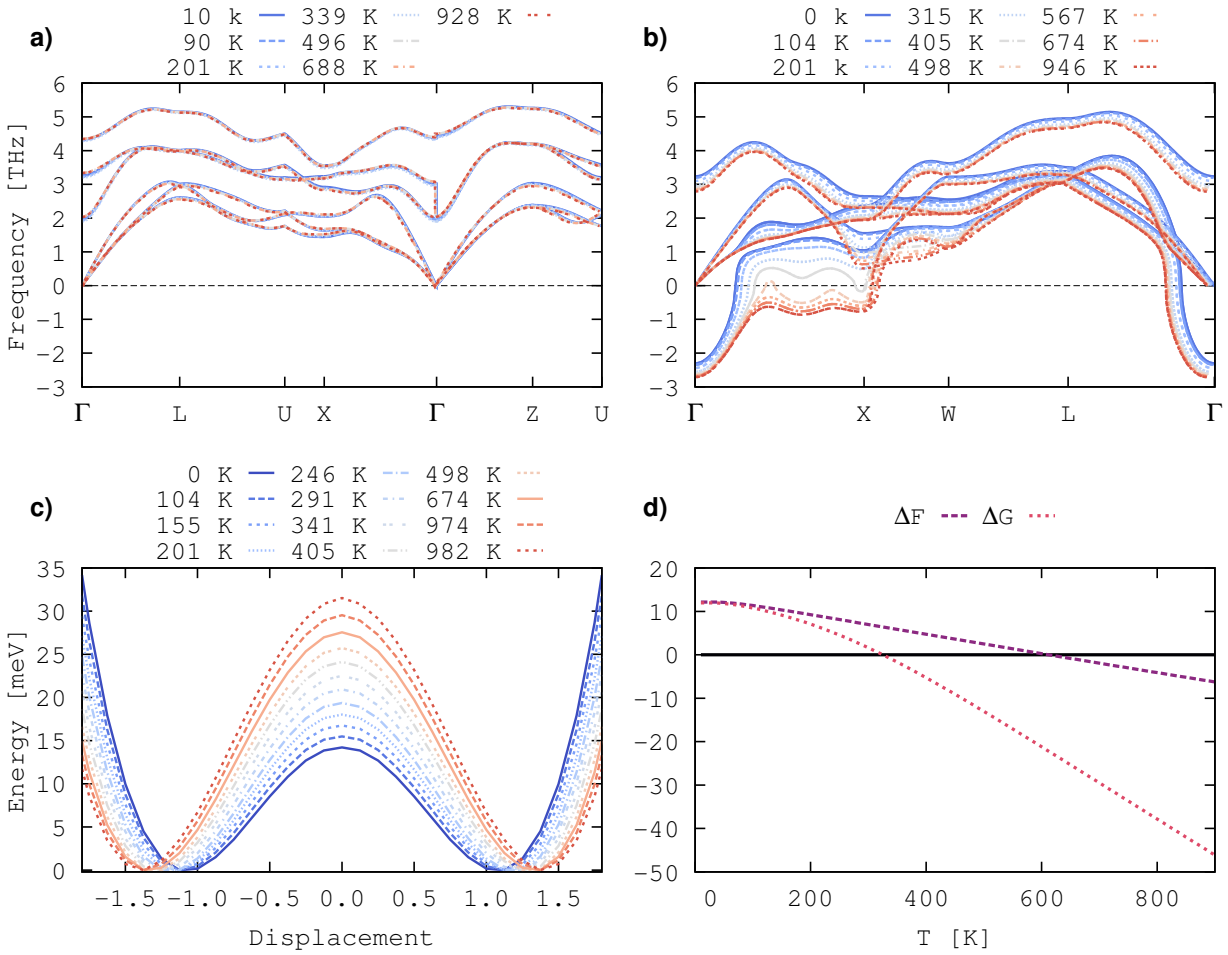

FIG. 2. Quasi-harmonic phonon dispersion curves for α- (a) and β-GeTe (b). Non-analytical corrections to the zone-center phonon frequencies have been included. The color gradient runs from blue (low T) to red (high T) across the temperatures associated with the volume expansions considered in our calculations. The energy as a function of Ge cation displacement along the $< 111 >$ direction from the cubic phase ($d = 0$) is plotted in (c), and shows a classic double-well potential-energy surface for which the curves have been normalized to the lowest distortion amplitude at T=0 K. Plot (d) shows the harmonic (constant-volume/Helmholtz; violet) and quasi-harmonic (constant-pressure/Gibbs, pink) free energy of β-GeTe relative to α-GeTe as a function of temperature.

C. Double Well Energy Surface

We have probed the potential energy surface associated with the phase transition by mapping the energy as a function of the distortion connecting the two end points. We define the coordinate u as the Ge cation displacement from its centrosymmetric position at $u = 0$, along the $< 111 >$ crystallographic direction, to the distorted position at $u = 1$ (Fig. 1). The result is a characteristic double-well potential energy surface with β-GeTe being a saddle point between two α-GeTe local minima. In the $T = 0$ K structure, the calculated energy barrier is on the order of 13.1 meV, and increases up to 31.5 meV at higher temperatures.

Up to $T = 498$ K, the energy barrier is lower than that required for the hopping process to be spontaneous given the available thermal energy (k_BT ~25 meV at $T = 300$ K). Above $T = 498$ K, the barrier increases in height, making it harder for the transition between minima to occur. When $T = 0$ K, the energy minima correspond to a ~0.02 Å displacement of the Ge cation. At higher temperatures the minimum shifts further, with the highest distortion of ~0.03 Å at $T = 982$ K.

The increase of the barrier with thermal expansion can be explained based on the bonding formation between Ge and the Te ions. Since the Ge ion moves to form bonds with three Te ions, then the more the structure expands, more energy is required to break the bonds to move it from one set of Te neighbours to the other, thus increasing the energy barrier.

D. Electronic Band Structure

The calculated electronic band structure of rhombohedral GeTe is shown in Fig. 3. We compare results obtained using DFT with the LDA functional and the QSGW method, and observe differences in the electronic spectra and consequently the band gaps and SOC splitting.

The direct band gap at the high-symmetry point L = (0.0, 0.5, 0.0) is 0.47 eV with DFT-LDA and increases slightly to 0.54 eV with QSGW. The LDA values are a quantitative match for the 0.48 eV gap obtained from the LDA calculations in Ref. 13. There is a smaller indirect band gap to a conduction band minimum (CBM) at L' = (0.35,0.20,0.20). Our calculations yield indirect gaps of 0.35 and 0.41 eV with DFT-LDA and QSGW, respectively, which are slightly higher than the LDA gap of 0.28 eV quoted in Ref. 13.

E. Rashba Splitting

The spin-orbit coupling in α-GeTe induces Rashba splitting centred around the high-symmetry point, Z, which is the wavevector perpendicular to the direction of the ferroelectric distortion. The Rashba band gap induced by the splitting along the $Z-A$ direction, E_g^R, is calculated to be 0.56 eV with both DFT-LDA and QSGW. We obtain a band gap at Z, E_g^Z, of 0.68 and 0.63 eV with DFT-LDA and QSGW, respectively. These calculations may be compared to literature values of 0.74 eV with PBE[1] and 0.96 eV with HSE06.[2,46] We note that both calculations from Refs. 1, 2 and 46 were performed using pseudopotentials, as opposed to the all-electron calculations performed in the present work.

We have further calculated a set of band structures along the α to β-GeTe transition (Fig. 4). Two points correspond to the high-symmetry structure with $u = 0$ (β-GeTe) and the ferroelectric structure with $u = 1$ (α-GeTe), while the other four are intermediate configurations along the distortion path.

Rashba splitting is absent in β-GeTe, owing to the presence of a center of inversion. Distortion leads to an increase in the magnitude of the Rashba splitting (Fig. 5), and a corresponding increase Rashba band gap from 0.06 to 0.56 eV (Tab. I). Fig. 4 shows that the upper valence and lower conduction bands of the centrosymmetric phase are doubly degenerate, and the spin degeneracies are lifted along the distortion path, leading to the observed increase in the band-gap widths.

F. Role of Spontaneous Polarization

The macroscopic electric polarization, calculated as the sum of electronic and ionic components using the Berry phase approach, are shown along the distortion path in Fig. 5. The spontaneous polarization shows a mild quadratic behaviour on going from the β to the α phase, resulting in a polarization difference between the end-points of $\Delta P_s = 0.53$ Cm^{-2}. This difference is consistent with the value of $\Delta P_s \sim = 0.60$ Cm^{-2} calculated in Ref. 13.

TABLE I. Calculated (QSGW) band gaps obtained from the six different dispersions depicted in Fig. 4, where the coordinate $u = 0.0$ corresponds to the high-symmetry β-GeTe structure and $u = 1.0$ indicates the low-symmetry α phase. E_g^R refers to the Rashba gap located along the $Z-A$ direction, while E_g^Z is the gap at the Z-point.

	u=0.0	u=0.2	u=0.4	u=0.6	u=0.8	u=1.0
E_g^R (eV)	0.06	0.10	0.18	0.30	0.42	0.56
E_g^Z (eV)	0.06	0.11	0.21	0.32	0.47	0.63

We can track the strength of the Rashba effect in GeTe through the Rashba energy E_R, which is the energy splitting from the high-symmetry point, along with the corresponding k-space momentum offset k_R. These quantities are calculated by searching for the extremal points of the valence and conduction bands using a gradient-minimization approach. The full Rashba interaction parameter is then defined as $\alpha_\mathrm{R} = 2E_\mathrm{R}/k_\mathrm{R}$.[1,2,46]

We tested the functional dependence of α_R in the low-temperature phase of GeTe. With DFT-LDA, α_R=4.10 eV Å and 1.89 eV Å, for the VBM and CBM respectively, with E_R=90.86 meV and k_R=0.044 Å^{-1} for the VBM and E_R=31.60 meV and k_R=0.033 Å^{-1} for the CBM. These results are in agreement with the values from Refs. 1 and 46, which quote PBE values of α_R=4.9 eV Å for the VBM (E_R = 227 meV and k_R=0.094 Å^{-1}) and 2.5 eV Å for the CBM (E_R = 120 meV and k_R=0.094 Å^{-1}). Still from Refs. 1 and 46 the values of HSE06 for the VBM decrease slightly when compared to their PBE values, although still higher when compared to the present results: α_R=4.2, with E_R = 187 meV and k_R=0.088 Å^{-1}.

For QSGW, a relevant decrease in the Rashba parameter for the VBM splitting is observed, which is mostly due to the contribution of E_R which presents a much lower value than for LDA (VBM: k_R=0.028 Å^{-1}, E_R=44.84 α_R = 3.24 eV Å. CBM: k_R=0.022 Å^{-1}, E_R=22.67 meV, and α_R = 2.07 eV Å).

In contrast to the smooth change in lattice polarization through phase transition, the behaviour of the Rashba parameter is markedly non-linear. Instead it fits to a fourth-order polynomial, with a maximum between u = 0.4–0.6. The magnitude of the Rashba splitting is larger for the valence band, which is formed mainly from p states from the heavier Te ions, whereas the conduction band is composed of predominantly Ge p states.[12]

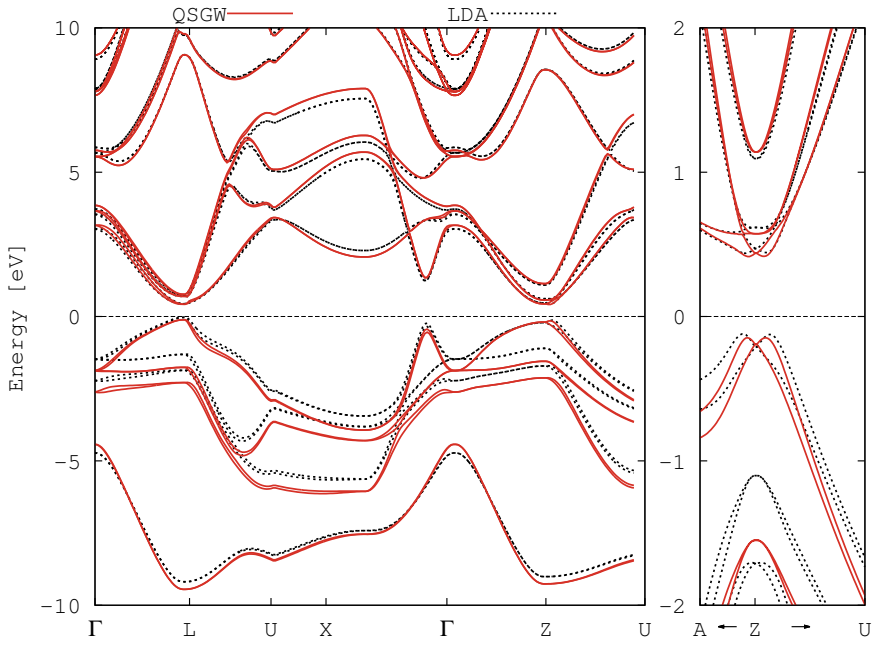

FIG. 3. Relativistic electronic band structure of the α ($R3m$) phase of GeTe. The lattice parameter $a_{300K} = 6.48$ Å is the value obtained from the quasi-harmonic approximation. The dotted black line shows the DFT-LDA band structure, while the solid red line shows the dispersion obtained from QSGW calculations. Both sets of calculations are performed using the same all-electron code, and the band dispersions are aligned to the calculated Fermi energies, and set to $E = 0$ eV. The left-hand plot shows the band structure along the main high-symmetry segments in the $R3m$ space-group, while the right-hand plot shows the dispersion along the A-Z-U path,[45] which is the plane normal to the polarization vector where the largest Rashba splitting is observed.

G. Role of Crystal-Field Splitting

The interactions responsible for the large Rasba-splitting in GeTe are not only the strong spin-orbit coupling, which induces splitting in the electronic band structure by coupling the spin and orbital degrees of freedom, but also the crystal-field (CF) splitting arising from changes in the local and long-range chemical environments. As a descriptor of the CF contribution, we calculate the on-site electrostatic-potential gradient at each of the lattice sites in the crystal. The values obtained from QSGW are shown in Fig. 5.c.

As expected, the magnitude of the CF is proportional to the spontaneous polarization, but there is a difference between lattice sites. In the $Fm\bar{3}m$ phase, the contribution of the two ion centers is zero, since the SOC and CF do not break the centrosymmetry of the crystal structure. For the intermediate structures, the intensity of the local electric field at the anion and cation sites increases linearly up to 0.44 and 1.04 eV/Å at the Te and Ge sites, respectively. The Ge center makes a slightly higher contribution to the splitting, which is due to the displacement of the cation from the centrosymmetric position adjusting the surrounding charge distribution of the Te anions and resulting in two different Te neighbor distances.[12]

IV. CONCLUSIONS

Despite its apparently simple chemistry and crystal structures, the physics of the phase transformation in GeTe continues to promote great debate, with evidence for the transition being both displacive and order-disorder nature. The imaginary phonon mode observed in the high-temperature cubic β-phase of GeTe in harmonic and quasi-harmonic lattice-dynamics calculations would appear to suggest a displacive second-order phase transition, which agrees not only with other theoretical results from relevant literature, but also from experimental techniques that probe the average structure. However, local structure and calorimetric measurements suggest the high-temperature phase is a crystallographic average over soft-mode minima. Our calculations also suggest that dynamic fluctuations in the local structure would occur as the cation transitions between local minima across a small energetic barrier. Moreover, our quasi-harmonic results imply that the cubic structure is a crystallographic average over the low-energy minima separating equivalent rhombohedral phases, since the dynamical

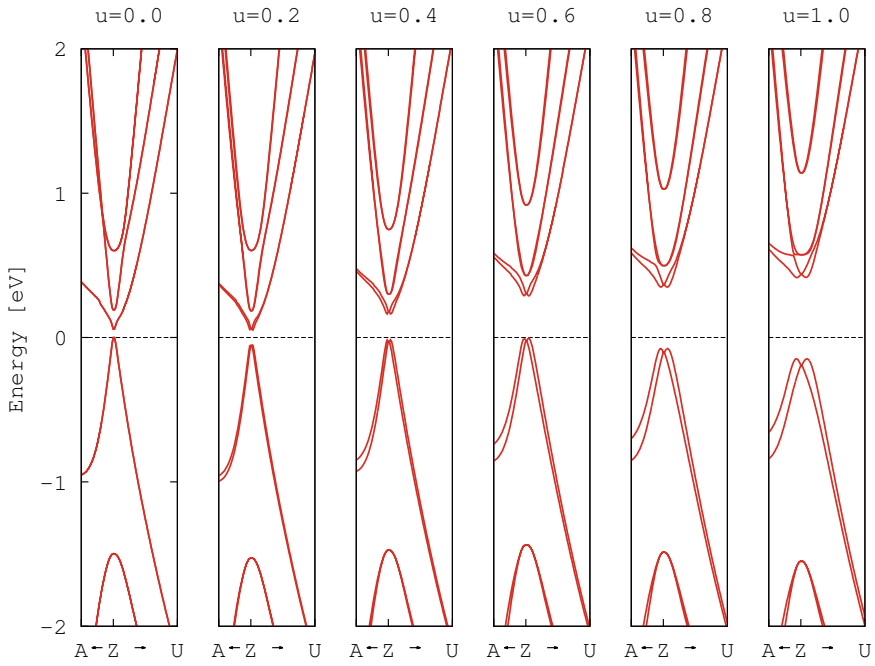

FIG. 4. Change in the relativistic QSGW electronic band structure along the path from the centrosymmetric β (u=0.0) to the non-centrosymmetric α (u=1.0) phases of GeTe. The dispersion is shown along the high-symmetry A-Z-U path where the largest Rashba effect is observed.[45])

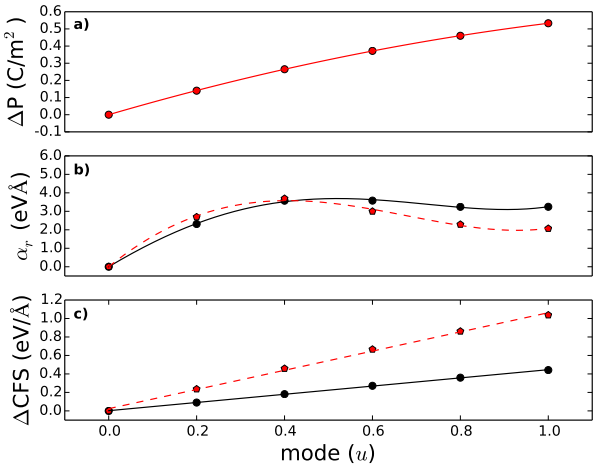

FIG. 5. (a) Change in electric polarization along the distortion path between the high-symmetry α and low-symmetry β phases of GeTe, calculated using the Berry-phase method with the HSE06 functional. (b) Change in the Rashba parameter (α_r) of the valence (black) and conduction (red) bands calculated using QSGW. (c) Change in crystal-field splitting of the Ge (red) and Te (black) ions calculated from QSGW.

instabilities persist for the high-symmetry phase at any studied temperature range.

We have shown that there is a smooth increase in spontaneous polarization on transition from the paraelectric β to ferroelectric α phase of GeTe, which is in with other published works. This smooth increase is accompanied by an increase in the electronic band gap and the appearance of relativistic Rashba splitting in the band structure. However, the Rashba interaction saturates at small distortion amplitudes due to the balance between macroscopic spontaneous polarization and local crystal-field effects.

We have presented results from all-electron QSGW calculations of the dynamics of the Rashba splitting and the crystal-field splitting as the distortion proceeds. Present QSGW results suggest that the Rashba parameter at the rhombohedral phase is smaller at the VBM than previously suggested through relevant theoretical literature, although the trend of the magnitude between the VBM and CBM parameter is the same (at the CBM the Rashba splitting has smaller magnitude). the crystal-field splitting shows a linear trend along the distortion path, with the biggest interaction occurring due to the Ge ion.

V. APPENDIX

A. Crystal Structure Optimization

Equilibrium volumes, lattice parameters and bulk moduli were determined by fitting energy-volume curves to the Birch-Murnaghan equation of state.[26,47] Table II presents the calculated lattice parameters and bulk moduli of the two phases of GeTe. For the cubic structure, we obtain a lattice parameter of $a_0 = 6.47$ Å and a bulk modulus $B_0 = 58$ GPa. The parameters for the rhombohedral structure are very similar at $a_0 = 6.47$ Åand $B_0 = 55$ GPa.

TABLE II. Equilibrium lattice parameters, a_0, and Bulk moduli, B_0, of the two phases of GeTe. We compare the equilibrium parameters to the values obtained within the quasi-harmonic approximation at room-temperature ($T = 300$ K) and close to the phase-transition ($T = 700$ K).

	a_0 (Å)			B_0 (GPa)		
	0 K	300 K	700 K	0 K	300 K	700 K
$Fm\bar{3}m(225)$ [a][b]	6.47	6.52	6.55	58	50	160
$R3m$ (160) [c]	6.47	6.48	6.49	55	73	79

[a] $a_0 = 5.85$ Å; $B_0 = 51$ GPa (LDA)[48]
[b] $a_0 = 5.99$ Å (Exp. $\sim=$ 300 K)[49]
[c] $a_0 = 5.89$ Å (LDA)[13]

B. Effect of LO–TO Splitting

Fig. 6 shows the phonon band structures of the cubic (a) and rhombohedral (b) phases of GeTe, with and without non-analytical corrections for LO–TO splitting. In the cubic structure (a), the correction lifts the LO mode from the doubly-degenerate TO modes, and it becomes real with $\nu \sim 3.5$ THz. The rhombohedral phase also shows large LO-TO splitting of 1.4 THz, although the three Γ-point optic modes have real frequencies.

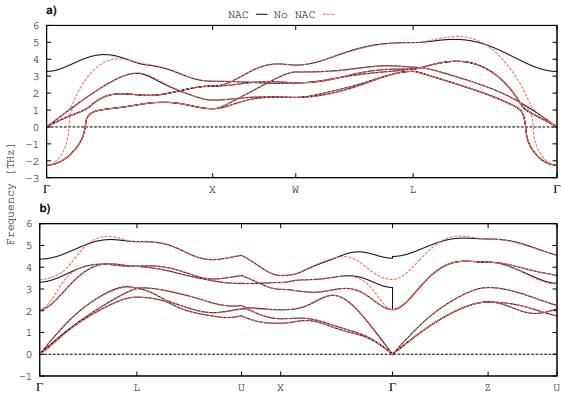

FIG. 6. Phonon band structures of the cubic (a) and rhombohedral (b) phases of GeTe. Each plot compares the dispersions obtained with and without a non-analytical correction to the long-wavelength phonon frequencies ($q \to 0$), which results in large LO-TO splitting at the zone-centre.

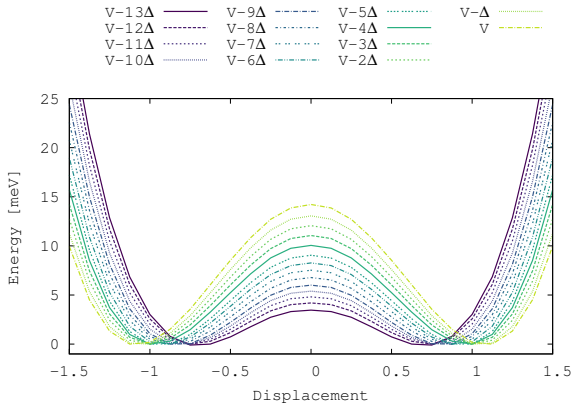

FIG. 7. Potential energy as a function of Ge cation displacement in cubic (β) GeTe under applied pressures of room pressure to 28.35 GPa.

C. Effect of Pressure

Fig. 7 shows potential-energy surface as a function of Ge cation displacement of the cubic phase under pressure. As the lattice constant is reduced and the pressure increases, the energy minimum shifts towards zero and the barrier between minima is progressively reduced; for the maximum applied pressure of 28.35 GPa, corresponding to a reduction in the volume of 3.12 Å^3, the energy minimum lies close to 0.01 Å, and the barrier decreases to 3 meV. These results suggest that the ferroelectric instability in the cubic phase may be suppressed by pressure, since beyond a threshold pressure the barrier will disappear and leave a single minimum at the cubic cation position. This is easily anticipated from the fact that the cation will be restricted to the cubic position due to space constraints at reduced lattice volumes.

* a.walsh@imperial.ac.uk

[1] Silvia Picozzi. Ferroelectric rashba semiconductors as a novel class of multifunctional materials. *Front. Phys.*, 2:10, 2014.

[2] Domenico Di Sante, Paolo Barone, Riccardo Bertacco, and Silvia Picozzi. Correction: Electric control of the giant rashba effect in bulk gete. *Ad. Mat.*, 25(27):3625–3626, 2013.

[3] K.M. Rabe and J.D. Joannopoulos. Ab Initio Determination of a Structural Phase Transiton Temperature. *Phys. Rev. Lett.*, 59(5):570, 1987.

[4] K.M. Rabe and J.D. Joannopoulos. Theory of the Structural Phase Transiton of GeTe. *Phys. Rev. B*, 36(12):6631, 1987.

[5] Urszula D. Wdowik, Krzysztof Parlinski, Stéphane Rols, and Tapan Chatterji. Soft-Phonon Mediated Structural Phase Transition in GeTe. *Phys. Rev. B*, 89:224306, Jun 2014.

[6] Tapan Chatterji, C. M. N. Kumar, and Urszula D. Wdowik. Anomalous Temperature-Induced Volume Contraction in GeTe. *Phys. Rev. B*, 91:054110, Feb 2015.

[7] T Chattopadhyay, J X Boucherle, and H G vonSchnering. Neutron Diffraction Study on the Structural Phase Transition in GeTe. *Journal of Physics C: Solid State Physics*, 20(10):1431, 1987.

[8] E.F. Steigmeier and G. Harbeke. Soft Phonon Mode and Ferroelectricity in GeTe. *Solid State Communications*, 8:1275, 1970.

[9] D. Yang, T. Chatterji, J. A. Schiemer, and M. A. Carpenter. Strain Coupling, Microstructure Dynamics, and Acoustic Mode Softening in Germanium Telluride. *Phys. Rev. B*, 93:144109, Apr 2016.

[10] Paul Fons, Alexander V. Kolobov, Milos Krbal, Junji Tominaga, K. S. Andrikopoulos, S. N. Yannopoulos, G. A. Voyiatzis, and T. Uruga. Phase Transition in Crystalline GeTe: Pitfalls of Averaging Effects. *Phys. Rev. B*, 82:155209, Oct 2010.

[11] T. Matsunaga, P. Fons, A. V. Kolobov, J. Tominaga, and N. Yamada. The Order-Disorder Transition in GeTe: Views from Different Length-scales. *Appl. Phys. Lett.*, 99(23):231907, 2011.

[12] U. V. Waghmare, N. A. Spaldin, H. C. Kandpal, and Ram Seshadri. First-principles indicators of metallicity and cation off-centricity in the iv-vi rocksalt chalcogenides of divalent ge, sn, and pb. *Phys. Rev. B*, 67:125111, Mar 2003.

[13] R. Shaltaf, E. Durgun, J.-Y. Raty, Ph. Ghosez, and X. Gonze. Dynamical, Dielectric, and Elastic Properties of GeTe Investigated with First-Principles Density Functional Theory. *Phys. Rev. B*, 78:205203, Nov 2008.

[14] P. Hohenberg and W. Kohn. Inhomogeneous Electron Gas. *Phys. Rev.*, 136:B864, 1964.

[15] W. Kohn and L. Sham. Self-Consistent Equations Including Exchange and Correlation Effects. *Phys. Rev.*, 140:A1133, 1965.

[16] G. Kresse and J. Furthmüller. Efficient iterative schemes for ab initio total-energy calculations using a plane-wave basis set. *Phys. Rev. B*, 54:11169, 1996.

[17] G. Kresse and J. Hafner. Ab initio molecular dynamics for liquid metals. *Phys. Rev. B*, 47:R558, 1993.

[18] G. Kresse and J. Furthmüller. Efficiency of ab-initio total energy calculations for metals and semiconductors using a plane-wave basis set. *Comput. Mat. Sci.*, 6:15, 1996.

[19] J. P. Perdew, A. Ruzsinszky, G. I. Csonka, O. A. Vydrov, G. E. Scuseria, L. A. Constantin, X. Zhou, and K. Burke. Restoring the density-gradient expansion for exchange in solids and surfaces. *Phys. Rev. Lett.*, 100:136406, 2008.

[20] J. P. Perdew, A. Ruzsinszky, G. I. Csonka, O. A. Vydrov, G. E. Scuseria, L. A. Constantin, X. Zhou, and Kieron Burke. Erratum: Restoring the Density-Gradient Expansion for Exchange in Solids and Surfaces [Phys. Rev. Lett. 100, 136406 (2008)]. *Phys. Rev. Lett.*, 102:039902, 2009.

[21] G. Kresse and D. Joubert. From ultrasoft pseudopotentials to the projector augmented-wave method. *Phys. Rev. B*, 59:1758, 1999.

[22] P. E. Blöchl. Projector augmented-wave method. *Phys. Rev. B*, 50:17953, 1994.

[23] E. Lora da Silva, Jonathan M. Skelton, Stephen C. Parker, and Aron Walsh. Phase Stability and Transformations in the Halide Perovskite $CsSnI_3$. *Phys. Rev. B*, 91:144107, Apr 2015.

[24] H. J. Monkhorst and J. D. Pack. Special Points for Brillouin-Zone Integrations. *Phys. Rev. B*, 13:5188, 1976.

[25] A. Togo, L. Chaput, I. Tanaka, and G. Hug. First-Principles Phonon Calculations of Thermal Expansion in Ti_3SiC_2, Ti_3AlC_2, and Ti_3GeC_2. *Phys. Rev. B*, 81:174301, 2010.

[26] F. D. Murnaghan. The Compressibility of Media under Extreme Pressures. *Proc. Natl. Acad. Sci.*, 30:244, 1944.

[27] P. Vinet, J. R. Smith, J. Ferrante, and J. H. Rose. Temperature Effects on the Universal Equation of State of Solids. *Phys. Rev. B*, 35:1945, 1987.

[28] A. Togo, F. Oba, and I. Tanaka. First-principles calculations of the ferroelastic transition between rutile-type and $CaCl_2$-type SiO_2 at high pressures. *Phys. Rev. B*, 78:134106, 2008.

[29] L. Chaput, A. Togo, I. Tanaka, and G. Hug. Phonon-phonon interactions in transition metals. *Phys. Rev. B*, 84:094302, 2001.

[30] P. Y. Yu and M. Cardona. *Fundamentals of Semiconductors: Physics and Materials Properties*. Number pp. 104. 1996.

[31] M. Gajdoš, K. Hummer, G. Kresse, J. Furthmüller, and F. Bechstedt. Linear Optical Properties in the PAW Methodology. *Phys. Rev. B*, 73:045112, 2006.

[32] Quantal Phase Factors Accompanying Adiabatic Changes. *Proceedings of the Royal Society of London A: Mathematical, Physical and Engineering Sciences*, 392(1802):45–57, 1984.

[33] R. D. King-Smith and D. Vanderbilt. Theory of Polarization of Crystalline Solids. *Phys. Rev. B*, 47:1651, 1993.

[34] Jochen Heyd, Gustavo E. Scuseria, and Matthias Ernzerhof. Erratum: "Hybrid Functionals Based on a Screened Coulomb Potential" [j. chem. phys. 118, 8207 (2003)]. *The Journal of Chemical Physics*, 124(21):219906, 2006.

[35] Jochen Heyd and Gustavo E. Scuseria. Efficient Hybrid Density Functional Calculations in Solids: Assessment of the Heyd–Scuseria–Ernzerhof Screened Coulomb Hybrid Functional. *The Journal of Chemical Physics*, 121(3):1187–1192, 2004.

[36] M. van Schilfgaarde, Takao Kotani, and S. Faleev. Quasiparticle self-consistent *gw* theory. *Phys. Rev. Lett.*, 96:226402, Jun 2006.

[37] Takao Kotani, Mark van Schilfgaarde, and Sergey V. Faleev. Quasiparticle self-consistent *gw* method: A basis for the independent-particle approximation. *Phys. Rev. B*, 76:165106, Oct 2007.

[38] Questaal Home. https://questaal.org.

[39] U. von Barth and L. Hedin. A Local Exchange-Correlation Potential for the Spin Polarized Case. *J. Phys. C: Solid State Physics*, 5(13):1629, 1972.

[40] O. Jepsen P. E. Blöchl and O. K. Anderen. Improved Tetrahedron Method for Brillouin-Zone Intergartions. *Phys. Rev. B*, 49:16223, 1994.

[41] M. T. Dove. *Introduction to Lattice Dynamics*, volume 8. Cambridge University Press, 1993.

[42] F. Bertolotti, L. Protesescu, M. V. Kovalenko, S. Yakunin, A. Cervellino, S. J. L. Billinge, M. W. Terban, J. S. Pedersen, N. Masciocchi, and A. Guagliardi. Coherent Nanotwins and Dynamic Disorder in Cesium Lead Halide Perovskite Nanocrystals. *ACS Nano*, 11:3819–3831, 2017.

[43] R. J. Worhatch, H. J. Kim, I. P. Swainson, A. L. Yonkeu, and S. J. L. Billinge. Study of Local Structure in Selected Cubic Organic-Inorganic Perovskites. *Chem. Mater.*, 20:1272–1277, 2008.

[44] Raffaello Bianco, Ion Errea, Lorenzo Paulatto, Matteo Calandra, and Francesco Mauri. Second-Order Structural Phase Transitions, Free Energy Curvature, and Temperature-Dependent Anharmonic Phonons in the Self-Consistent Harmonic Approximation: Theory and Stochastic Implementation. *Phys. Rev. B*, 96:014111, Jul 2017.

[45] D. Di Sante, P. Barone, R. Bertacco, and S. Picozzi. Electric Control of the Giant Rashba Effect in Bulk GeTe. *Advanced Materials*, 25(4):509–513, 2013.

[46] Domenico Di Sante, Paolo Barone, Riccardo Bertacco, and Silvia Picozzi. Electric control of the giant rashba effect in bulk gete. *Ad. Mat.*, 25(4):509–513, 2013.

[47] F. Birch. Finite Elastic Strain of Cubic Crystals. *Phys. Rev.*, 71:809, 1947.

[48] K. M. Rabe and J. D. Joannopoulos. Structural Properties of GeTe at T=0. *Phys. Rev. B*, 36:3319–3324, Aug 1987.

[49] J.N Bierly, L Muldawer, and O Beckman. The Continuous Rhombohedral-Cubic Transformation in GeTe-SnTe Alloys. *Acta Metallurgica*, 11(5):447 – 454, 1963.

4.2 Effective Mass

In a solid electrons experience a potential in the crystal, which can be accounted for by treating them as free electrons with an effective mass m^* [110].

The *de Broglie* wave-length is written as:

$$\lambda = \frac{h}{p}, \tag{4.1}$$

where $p = m\nu$ is the momentum of the electron and h is the Planck constant. By noting that $k = 2\pi/\lambda$, we can re-write the wave-vector in the form:

$$k = \frac{p}{\hbar} \tag{4.2}$$

where $\hbar = h/2\pi$ is the reduced Planck constant.

The energy states of a free electron as a function of the wave-vector, can be represented by the dispersion relation as:

$$E = \frac{1}{2}mv^2 = \frac{p^2}{2m} = \frac{\hbar^2 k^2}{2m} \tag{4.3}$$

An exact defined value of the wave-vector, $\mathbf{k}$, implies complete uncertainty about the position of the electron in real space (Heisenberg uncertainty), and thus localisation can be described by expressing the state of the electron as a wave-packet, with a defined velocity. The group velocity defines the slope of the dispersion relation, and is given by:

$$v_g = \frac{\partial \omega}{\partial k} \tag{4.4}$$

The frequency, ω, is related to the energy E through the Planck-Einstein relations:

$$E = \omega\hbar \tag{4.5}$$

Combining Eqs. 4.2 and 4.5 one obtains:

$$v_g = \frac{1}{\hbar}\frac{\partial E}{\partial k} \tag{4.6}$$

Differentiating Eq. 4.6 with respect to time, one therefore obtains:

$$\frac{\partial v_g}{\partial t} = \frac{1}{\hbar}\frac{\partial^2 E}{\partial k \partial t} = \frac{1}{\hbar}\frac{\partial^2 E}{\partial k^2}\frac{\partial k}{\partial t} \tag{4.7}$$

From the Planck-Einstein relation, (Eq. 4.5), we can write:

$$mv_g = \hbar k \tag{4.8}$$

and thus:

$$m\frac{\partial v_g}{\partial t} = \hbar\frac{\partial k}{\partial t} \tag{4.9}$$

which gives the force, F, acting on the group of electrons. Combining Eqs. 4.7 and 4.9, yields:

$$F = \frac{\hbar^2}{\partial^2 E/\partial k^2}\frac{\partial v_g}{\partial t} \tag{4.10}$$

Since there is a force acting on the electrons, the mass of the free electron should be replaced by an effective mass, m^*, which is given by:

$$\frac{1}{m^*} = \frac{1}{\hbar^2}\frac{\partial^2 E}{\partial k^2} \tag{4.11}$$

The effective mass determines the local curvature of the dispersion energy of reciprocal space, and is therefore a tensor qunatity [110]:

$$\left(\frac{1}{m^*}\right)_{\alpha\beta} = \frac{1}{\hbar^2}\frac{\partial^2 E}{\partial k_\alpha \partial k_\beta} \tag{4.12}$$

where α, β are the three Cartesian directions.

The density of states (DOS) effective mass can be obtained as the geometric mean of the three masses. Taking into account that there may be several equivalent minima (e.g., two degenerate bands at the high symmetry Z-point in the rhombohedral phase of GeTe), one obtains the DOS effective mass by:

$$m^*_{\text{dos}} = g^{2/3}(m_x m_y m_z)^{1/3} \tag{4.13}$$

where g is the degeneracy factor counting the number of equivalent valleys. By considering the DOS on a per-valley basis one may omit g [111], which we do hereafter.

Table 4.1 presents the calculated effective masses at the Rashba-gap, obtained by employing the QSGW method (complete details of the parameters for the calculation can be found in Sec. 4.1). It can be seen that the effective masses are anisotropic, and for the cubic structure, at u=0.0, that they are lighter in two directions and heavier component in the third. As the symmetry is broken, the anisotropy of the mass components are also altered. Anomalous behaviour of the intermediate structure (u=0.8) is observed at the valence band (z-direction)

Table 4.1: QSGW principle effective masses in the x-, y- and z- directions, calculated at the Rashba-gap (along the A-Z segments) for the two phases of GeTe, $Fm\bar{3}m$ and $R3m$, and also for four intermediate structures, along the distortion path between the two phases. A negative valence band mass is consistent with a downward curvature, whereas the masses of the conduction band are positive (upward curvature). Values are given in units of the rest mass, where $m_0 = 9.11 \times 10^{-31}$ kg.

	valence			conduction		
u=0.0	-0.006	-0.006	-0.148	0.154	0.008	0.008
u=0.2	-0.014	-0.028	-0.296	0.295	0.067	0.018
u=0.4	-0.016	-0.235	-0.407	0.882	0.440	0.021
u=0.6	-0.016	-0.035	-0.548	0.504	0.063	0.028
u=0.8	-0.046	-0.959	55.422	0.557	0.524	0.058
u=1.0	-0.074	-1.446	-3.819	13.341	0.380	0.114

with a value of 55.422 m_0. Also at the conduction band and for the $R3m$ structure the effective mass value at the x-direction is also abnormal (13.341 m_0). The cause for these discrepencies are not yet understood and further analysis are required in order to determine the cause of these irregular values for the obtained effective mass componentes.

For the high-symmetry phase, the geometric means of the per-valley effective masses at the Z-point are $m^*_{\mathrm{h\,dos}}$=0.017 m_0 and $m^*_{\mathrm{e\,dos}}$=0.021 m_0 for the holes and electrons, respectively. The effective masses increase when the system undergoes the transition to the $R3m$ phase, such that $m^*_{\mathrm{h\,dos}}$=0.025 m_0 and $m^*_{\mathrm{e\,dos}}$=0.045 m_0. By comparing these with m^* at the Rashba band-gap (along A-Z), we obtain $m^*_{\mathrm{h\,dos}}$=0.740 m_0 and $m^*_{\mathrm{e\,dos}}$=0.833 m_0, with much heavier masses and thus a different carrier mobility closer to the Fermi level (Sec. 4.1, Fig.4, for more details).

Fig. 4-1 shows the geometric mean of the per-valley effective masses at the Z-point for the centrosymmetric phase (Rashba-gap when inversion symmetry is broken), intermediate structures and the ferroelectric phase. The best adjusted fit was found to be an 8th order polynomial of the form

$$ax^2 + bx^4 + cx^6 + dx^8 \tag{4.14}$$

where a, b, c and d are the fitted coefficients and x is the geometric mean effective mass.

The values increase as the splitting increases, with a peak at u=0.8 in $m^*_{\mathrm{h\,dos}}$ due to the anomalous behaviour of the heavy component (Tab. 4.1).

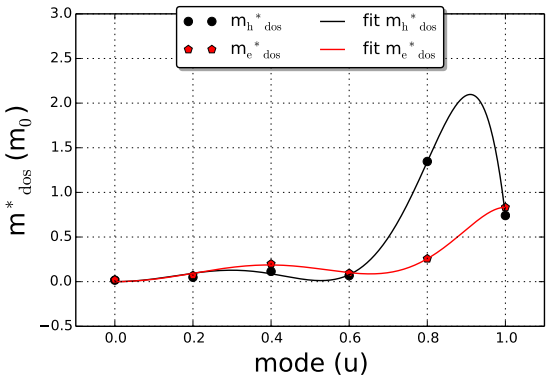

Figure 4-1: Effective masses calculated for six structures of GeTe, along the path between the cubic and rhombohedral structures, where u=0 refers to the former and u=1 to the latter. Intermediate values lie on the distortion pathway between u=0 and u=1. The plots are fitted to an 8^{th} order polynomial.

4.3 Dielectric Properties

The Born-effective charges are considered a good indication of a ferroelectric instability, since the values tend to be larger than the nominal ionic charges in most ferroelectric materials. However, anomalous values alone are not a sufficient indicator of a ferroelectric transition [97, 98].

The frequency splitting of the longitudinal and transverse optic modes at the zone centre (LO-TO splitting) is obtained by including a non-analytical correction to the dynamical matrix at $q \rightarrow 0$, based on the Born effective-charge tensors and the electronic-polarisation component of the macroscopic static dielectric tensor [112]. For the cubic system, a large LO-TO splitting in the phonon spectrum is correlated to a strong instability in the system (Sec. 4.1, Appendix B). The rocksalt GeTe structure shows a doubly-degenerate TO mode and hence has a single LO-TO splitting, which is isotropic due to the cubic symmetry. These quantities were obtained by using the density-functional perturbation theory routines (implemented in VASP [113]) on the unit cells of the two structures. Convergence of these quantities required increasing the **k**-point mesh to 30×30×30 for the two phases (more details in Sec. 4.1, Theoretical Methods).

The values of the Born-effective charges are relatively high when compared to the nominal ionic charges of the elements that comprise GeTe (Ge=+2 and Te=-2) [90]. The arguments rely on the fact that the differences may be caused by partial hybridization of the p-states in Ge and Te, resulting in mixed ionic-covalent bonding [90]. The effective charges of the cubic structure are much larger than those in the rhombohedral structure (Tab. 4.2). For the rhombohedral phase, the independent components, (one parallel to the trigonal axis and two perpendicular)

Table 4.2: Born effective-charges of the high-symmetry ($Fm\bar{3}m$) and the ground-state ($R3m$) phases of GeTe. Values are given in matrix form, where the diagonal elements represent the x, y and z Cartesian directions.

$Fm\bar{3}m$ (225)					
Te			Ge		
-10.14629	0.00000	0.00000	10.09108	0.00000	0.00000
0.00000	-10.14629	0.00000	0.00000	10.09107	0.00000
0.00000	0.00000	-10.14629	0.00000	0.00000	10.09107
$R3m$ (160)					
Te			Ge		
-6.38925	0.72864	0.72864	6.38995	-0.73020	-0.73020
0.72843	-6.38831	0.72843	-0.73000	6.38901	-0.73000
0.72865	0.72865	-6.38765	-0.73011	-0.73011	6.38838

are slightly higher than those reported in Ref. [90]. In the present work, we obtain for the Ge ion 7.120 and 4.929 (eigenvalues calculated from the matrix shown in Tab. 4.2), whereas the Te charges are -7.117 and -4.931, when compared to 6.897 and 4.574, and -6.894 and -4.571, for Ge and Te, respectively [90] (28×28×28 **k**-point mesh spacing, 408 eV energy cut-off and HGH pseudopotentials). Despite this, the difference between the independent components is 2.2, which is a similar magnitude to that found in Ref. [90], which effect is caused by the strongly anisotropic charge tensor.

When we apply the Born-effective charges to the phonon band-structure (Sec. 4.1, Appendix C. Fig. 6.b and Fig. 4-2) and, due to the crystal anisotropy, the LO-TO splitting varies significantly along different phonon segments. Along the X-Γ direction ($\overrightarrow{X\Gamma}$) three optic modes with different frequencies are observed. Whereas, along the Γ-Z direction ($\overrightarrow{\Gamma Z}$) one observes that the two lower frequency optic modes are degenerate (E symmetry), with a higher frequency mode with A_1 symmetry [90]. For $\overrightarrow{X\Gamma}$, the three optic frequencies are located at ν=2.1 THz, ν=3.0 THz and ν=4.2 THz, whereas for $\overrightarrow{\Gamma Z}$ we obtain ν=2.1 THz, ν=4.2 THz. The lower and higher frequencies observed in the present calculations are consistent with what was obtained theoretically in Ref. [90], where E(TO)=2.2 THz, and A(LO)=4.6 THz and, experimentally with two lines observed at 4.2 THz and one at 2.9 THz [114].

Also, if one does not consider the NAC term, in order to artificially enforce a complete screening of the dipole-dipole interaction by the conduction electrons, as argued in Ref. [90], the higher frequency optic mode, A_1, lowers the frequency down to ν=3.4 THz. The second mode previously located at ν=3.3 THz, becomes degenerate, lowering the frequency down to ν=2.1 THz (see Appendix C of Sec. 4.1). It has also been argued, from an experimental perspective, [114] that the LO mode is screening-degenerate with the lower frequency TO mode

Table 4.3: Calculated dielectric constants (ϵ_{ij}^{∞}) for the high-symmetry ($Fm\bar{3}m$) and the ground-state ($R3m$) phases of GeTe. Values are given in matrix form, where the diagonal elements represent the x, y and z Cartesian directions.

Fm-3m (225)			R3m (160)		
119.628750	0.00000	0.00000	59.842286	-3.391783	-3.391783
0.00000	119.628750	0.00000	-3.391783	59.842286	-3.391783
0.00000	0.00000	119.628750	-3.391783	-3.391783	59.842286

due to the high-carrier concentration (dipole-dipole interaction); therefore the TO-LO modes would correspond to the E mode, of Γ_1 ir.reps. The higher frequency A_1 mode (Γ_3 ir.reps.) would therefore be the TO, which is split by the anisotropy of the crystal, and it is the mode responsible for the ferroelectric-to-paraelectric phase transition. [114, 90]

The dielectric tensor, ϵ_{ij}, is related to the applied electric field, defined as:

$$E_i = \sum_j \epsilon_{ij}^{-1} E_{0j} \tag{4.15}$$

where E is the electric field inside the material and E_0 is the externally appplied field. The indices i and j refer to the spatial coordinates. The dielectric tensor can be decomposed into two components [115, 116] as:

$$\epsilon_{ij} = \epsilon_{ij}^{0} + \epsilon_{ij}^{\infty} \tag{4.16}$$

where ϵ_{ij}^{0} is the ionic contribution (low-frequency) and ϵ_{ij}^{∞} is the electronic contribution (high-frequency) and compares as $\epsilon_{\infty} = n^2$, with n being the refractive index [115, 116].

In the case that a material does not respond to the external field, ϵ_{ij}^{∞} results in the identity tensor and ϵ_{ij}^{0} would thus be zero. In order for ϵ_{ij}^{0} to have a finite value, at least two ions (with different charges) in the primitive cell would be required [117, 118].

The dielectric constants of the two phases of GeTe are obtained with the same converged **k**-point sampling mentioned for the Born-effective charges (30×30×30). For the low-frequency behaviour, the interatomic force constants were computed using linear-response DFPT calculations (more details in Sec. 4.1). The high-frequency dielectric constants were obtained by calculating the optical dielectric functions in the independent-particle approximation.

In Tab. 4.3 the values for ϵ_{ij}^{∞} are listed in matrix form and Tab. 4.4 gives the corresponding values of ϵ_{ij}^{0}. The cubic structure shows very large $\epsilon_{ij}^{\infty} = 119.6$ which is entirely from ϵ_{ij}. This is due to the small band-gap, which is also reflected in the Born-effective charges [90].

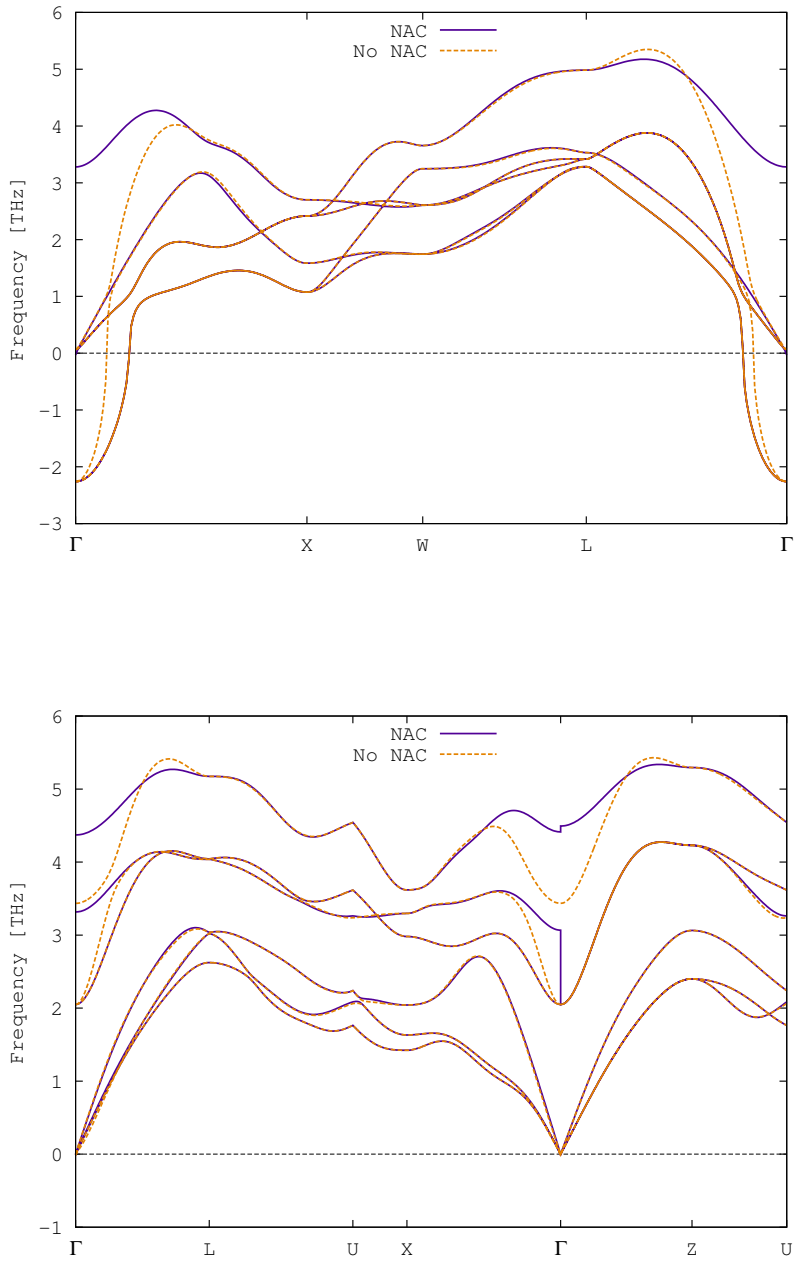

Figure 4-2: Phonon band-structure of the cubic phase (top) and rhombohedral (bottom) phase of GeTe. Comparison is made when Born-effective charges are applied, which results in anormously large LO-TO splitting at the zone-centre.

Table 4.4: Calculated low-frequency dielectric constants (ϵ^0_{ij}) of the high-symmetry ($Fm\bar{3}m$) and the ground-state ($R3m$) phases of GeTe. Values are given in matrix form, where the diagonal elements represent the x, y and z Cartesian directions.

Fm-3m (225)			R3m (160)		
0.00000	0.00000	0.00000	160.368150	-60.805026	-60.805026
0.00000	0.00000	0.00000	-60.805026	160.317851	-60.792190
0.00000	0.00000	0.00000	-60.805026	-60.792190	160.293118

Since the calculations are not considering the long range polarisation interaction, therefore not considering the splitting betweent the TO and LO optic modes (Sec. 4.1, Appendix B) the ionic contribution (ϵ^0_{ij}) is zero for the cubic system.

Since the $R3m$ phase has two independent components (perpendicular and parallel to the trigonal axis), we obtain values of 63.2 and 53.1 for ϵ^∞_{ij}, and 221.1 and 38.7 for ϵ^0_{ij}, respectively. This results in $\epsilon_{ij} = 284.3$ for the perpendicular component and $\epsilon_{ij} = 91.8$ for the parallel component. It should be noted that the ionic contribution, especially for the perpendicular independent component, is quite high, which can be due to the frequency difference observed in the phonon-band structure between $\nu_1 = 2.0$ THz and $\nu_2 = 3.4$ THz, as discussed in Sec. 4.1 (Appendix B). The values of the electronic contributions are close to results obtained in Ref. [90], but the ionic contributions are higher, with values of 247.32 and 68.67 for the perpendicular and parallel components, respectively. This discrepancy is likely due to the differences in the cut-off defined in the two sets of calculations (408 eV *vs* 800 eV in the present work).

4.4 Electric Equation of State

To assess the macroscopic behaviour through the phase transition in GeTe, an electric equation of state based on a Landau-type free energy is employed. Within this method, the evolution of the polarisation from the centrosymmetric to the ferroelectric phase is studied in order to model the hysteresis behaviour.

By applying an external electric field, E, we will define u as the order parameter (polar degree of freedom), which refers to the distortion path from the centrosymmetric phase ($u = 0$) to the polar structure ($u = 1$) at $E = 0$. Since the free energy can be expressed as a function of u, the dependant variable in thermal equilibrium is obtained by minimising the free energy. Therefore, by expanding the free energy up to second order in E and sixth order in u, the total energy and dielectric constants (calculated with DFT using the non-local HSE06 functional with SOC) can be fitted to the electric equation of state developed in Ref. [91], which applies

to proper-ferroelectrics and hyperferroelectrics [91]:

$$\mathcal{F}(u,E) = -au^2 + bu^4 + cu^6 - P_{\mathrm{S}}uE - \frac{1}{2}\chi_e(u)E^2 \tag{4.17}$$

where $\mathcal{F}$ is the free energy per volume unit (energy density); χ_e is the electronic susceptibility as a function of u (dimensionless parameter since $\chi_e = \epsilon_\infty(u)-1$); P_{S} the spontaneous polarisation at $E = 0$ ($P_{\mathrm{S}_{(u=1)}} - P_{\mathrm{S}_{(u=0)}}$); a, b and c are constants, which have to satisfy the dimensions of energy density since u is a dimensionless parameter.

The polarisation is obtained from:

$$P(u) = -\frac{\partial \mathcal{F}}{\partial E} = P_{\mathrm{S}}u + \chi_e(u)E \tag{4.18}$$

DFT calculations were carried out to obtain the energies and dielectric constants of six structures along the $Fm\bar{3}m \rightarrow R3m$ path. Two of these correspond to the end-points, i.e. the high-symmetry structure with u=0 ($Fm\bar{3}m$) and the ferroelectric structure with u=1 ($R3m$). The remaining four are intermediate configurations corresponding to the distortion path between them. The effect of spin-orbit coupling (SOC) were considered in the calculations.

Since the inclusion of SOC affects the band-gap and characterises the high-symmetry structure towards metallic behaviour, the PBEsol functional does not prove sufficient to obtain a good description of the dielectric tensors. Therefore, and for this effect, the HSE06 functional was employed with a reduced Γ-centered 6×6×6 **k**-point mesh and a plane-wave cut-off of 700 eV. The frequency dependant dielectric response was computed within the independent-particle approximation.

The macroscopic polarization was evaluated using the Berry phase expressions and we obayained a spontaneous polarization of $\Delta P_s = 0.533$ Cm^{-2}. This value is obtained by comparing the calculated polarisation of the centrosymmetric structure with that of the ferroelectric phase (more details in Sec. 4.1, Fig. 5.a).

Fig. 4-3 shows the computed energy landscapes and the results obtained from DFT by fitting the data to the electric equation of state (Eq. 4.17). The top panels of Fig. 4-3 (left) plot the relative energies of the six structures (referenced to the high-symmetry structure) along the distortion path. The top right panel shows the dielectric constants of the six structures, and as discussed in Sec. 4.3, the value for the cubic structure when compared to the ferroelectric phase at u=1.0 is very high. One must point out that the values presented in Sec. 4.3 are slightly different, since the present calculations were carried out by using the hybrid functional instead of PBEsol as in Sec. 4.3.

The middle panels of Fig. 4-3 show the behaviour of the Landau free energy from Eq. 4.17 (left) and the polarisation from Eq. 4.18 (right) as a function of the distortion, for different intensities of applied electric field. For $E = 0$, the free energy only depends on the relative

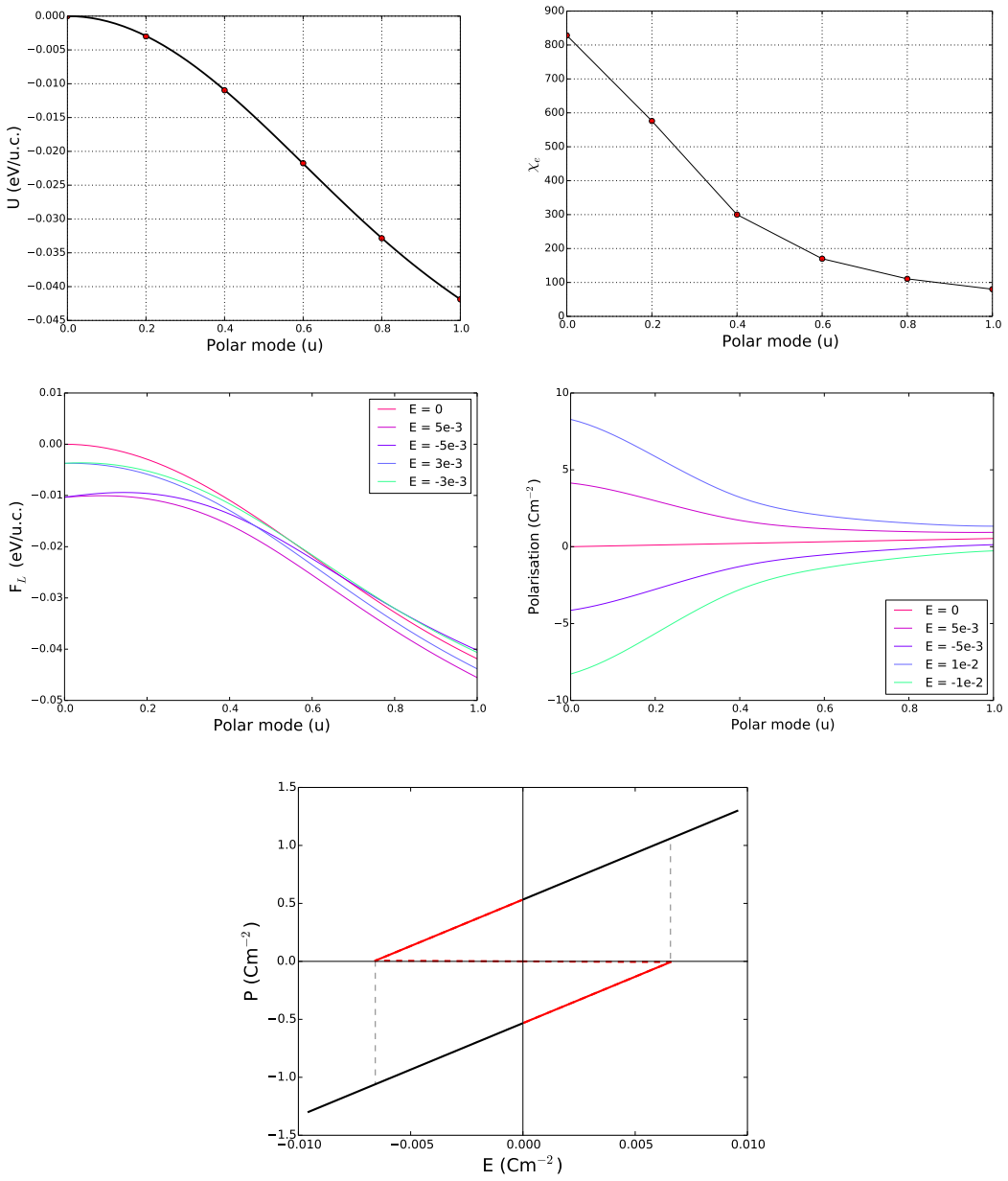

Figure 4-3: Computed energy landscape and electric equations of state for GeTe (with spin-orbit coupling). Top plots: Internal energy *vs* polar mode (left) and zero field electronic susceptibility *vs* polar mode (right). Middle plots represent the effect of the free energy density and polarisation under the application of different electric fields. Bottom plot: Polarisation *vs* Electric Field. Dashed red lines are locally unstable; solid red lines are locally stable; solid black lines are globally stable regions.

energies of the systems, as the last two terms in Eq. 4.17 vanish. When a field is applied we observe that for the same magnitude, but reversed sign, the features are symmetrical. The polarisation when $E = 0$ is zero at u=0.0, and has a finite value at u=1.0 (ΔP_s=0.533 C/m^2). The polarisation then assumes a finite value at u=0.0 when a field is applied. The polarisation values are quite large at u=0.0 and decrease at u=1.0, following a symmetric behaviour with the sign of the field. By inspecting Eq. 4.18, one may conclude that the large polarisation for the high-symmetry structure arises due to the large values of the dielectric constant f this phase, and since these are multiplied by E, the last term of Eq. 4.18 accounts for the increase of P when E increases.

The last panel of Fig. 4-3 plots the P-E hysteresis loop for GeTe. At E=0, we have a remanent polarisation, which is equal to the spontaneous polarisation of the material, P$_r$=0.533 C/m^2. Since P is multivalued at E=0, this indicates that GeTe is a ferroelectric, as expected. To destroy the remnant polarisation, the crystal must be polarised in the opposite direction by applying an opposite electric field. The coercive field at P=0 c/m^2, which is needed to counteract the polarisation, is E=0.007 C/m^2. The saturation limit, where all material dipole moments are aligned parallel to the external electric field (single domain), occurs when E=0.01 C/m^2, for P ∼1.324 C/m^2.

Chapter 5

Bilayer Graphene (BLG)

The thing that doesn't fit is the thing that's the most interesting: the part that doesn't go according to what you expected.
Richard P. Feynman

Many properties of the monolayer graphene (MLG) have been theoretically studied to allow further characterisation of this material. These properties are unconventional due to the unique band structure of graphene, which is described in terms of Dirac fermions.

The experimental study of graphene triggered a growing attention to its electronic properties [119], because the honeycomb lattice defines a band structure [120] with two nodal points in the Brillouin zone, which determines a relativistic Dirac-type electronic dynamics [121] (creating links with certain theories of particle physics). These properties are responsible for the unusual phenomena that emerge in the material, such as the fractional Hall effect [122, 123, 124, 125], which allows the possibility for magnetic catalysis of an excitonic gap [126, 127, 128, 129, 130], ferromagnetism and superconductivity [131].

More recently, attention has turned to multilayer graphene [132] and, particularly, to the bilayer graphene (BLG), which also reveals abnormalities, i.e. Quantum Hall effect [133]. In fact, it was shown that the BLG also shows unconventional behaviour in its properties, however, these properties are different from those observed in MLG.

Between several derivatives of the MLG system, special interest is also given to its bilayer allotrope. Two known modifications of bilayer graphene (BLG) can coexist with different stacking environments: the Bernal (or AB) and its alternative AA structure. The interest in BLG is mainly due to the possibility of inducing a semiconductor with a tunable band gap. The most reliable structure for external tuning has been observed for the Bernal-stacked BLG, which can occur through the application of an electric field normal to the layers [19].

The study of the structural (in)stabilities of the AB and AA stackings was structured between two different studies. The first study is related to the electronic properties of the

(un)biased systems, in which the widths of the band-gaps as a function of different bias strengths are analysed, together with the scaling behaviour of the band dispersion in momentum-space. The DFT-LDA electronic dispersion is compared with analytical tight-binding band dispersions, in order to adjust the convergence parameters of the DFT calculations accordingly. Moreover, the effects of spin-orbit coupling are also considered together with the applied bias. The second part relates lattice dynamics within the harmonic approximation with the different bias intensities.

5.1 Electronic and Phonon Instabilities in Bilayer Graphene under Applied External Bias

The manuscript that follows concludes the work carried out during the last stages of the PhD. For this, the acquired knowledge of lattice dynamics was essential to compute and analyse the phonon dispersions of the 2D biased bilayer systems. Also the work was extended to obtain a more complete understanding of the electronic properties of this graphene analogue for which the stacking layout deeply affects the weak coupling interaction of the two layers.

The following article is published as Tompsett, DA 2014, 'Electronic structure and phonon instabilities in the vicinity of the quantum phase transition and superconductivity of (Sr, Ca) 3 Ir 4 Sn 13', Physical Review B, vol. 89, no. 7, 075117 and is available online via: https://doi.org/10.1103/PhysRevB.89.075117.

Electronic and Phonon Instabilities in Bilayer Graphene under Applied External Bias

E. Lora da Silva[1], M. C. Santos[2], J. M. Skelton[1], Tao Yang[3,4], S. C. Parker[1], A. Walsh[5]

[1]Department of Chemistry, University of Bath, Bath BA2 7AY, United Kingdom
[2]Department of Physics, University of Coimbra, 3004-516 Coimbra, Portugal
[3]Key Laboratory of Biofuels, Qingdao Institute of Bioenergy and Bioprocess Technology, Chinese Academy of Sciences, Qingdao, 26610, China
[4]TEMA-NRG, Department of Mechanical Engineering, University of Aveiro, 3810-193 Aveiro, Portugal
[5]Department of Materials, Imperial College London, South Kensington Campus, London SW7 2AZ, United Kingdom

E-mail: a.walsh@imperial.ac.uk

February 2018

Abstract. We have performed electronic-structure and lattice-dynamics calculations on the AB and AA structures of bilayer graphene. We study the effect of external electric fields and compare results obtained with different levels of theory to existing theoretical and experimental results. Application of an external field to the AB bilayer alters the electronic spectrum, with the bands changing under bias from a parabolic to a "Mexican hat" structure. This results in a semi-metal-to-semiconductor phase transition, with the size of the induced electronic band-gap being tuneable through the field strength. A reduction of continuous symmetry from a hexagonal to a triangular lattice is also evidenced through in-plane electronic charge inhomogeneities between the sublattices. When spin-orbit coupling is turned on for the AB system, we find that the bulk gap decreases, gradually increasing for larger intensities of the bias. Under large bias the energy dispersion recovers the Mexican hat structure, since the energy interaction between the layers balances the coupling interaction. We find that external bias perturbs the harmonic phonon spectra and leads to anomalous behaviour of the out-of-plane flexural ZA and layer-breathing ZO' modes. For the AA system, the electronic and phonon dispersions both remain stable under bias, but the phonon spectrum exhibits zone-center imaginary modes due to layer-sliding dynamical instabilities.

Keywords: Bilayer graphene, electric field, electronic properties, lattice dynamics

1. Introduction

Among the numerous derivatives of the monolayer graphene (MLG) system, special interest has been given to the multi-layer allotropes [1], in particular *Bernal* bilayer graphene with AB stacking (AB-BLG) [2]. Like ML graphene, BL graphene also

displays unconventional properties [3] that are relevant to technological developments including tunnelling field-effect transistors [4], high-rate lithium-sulphur batteries [5, 6], nanophotonics [7], sensor modelling [8], among others. These properties originate from the weak coupling between layers, which allows for the properties of the base ML graphene material to be retained. Despite the similarities between ML and BL graphene, there are also significant differences between the two allotropes. ML graphene shows a linear band dispersion near the Fermi energy, and the valence and conduction bands touch at the K-point (the Dirac point), yielding the characteristic dispersion of relativistic massless Dirac electrons [9, 10]. For unbiased AB-BLG, on the other hand, the interlayer coupling produces a parabolic-like band structure around the K-point. These different features result in a vanishing of the density-of-states (DOS) at the Fermi energy for the MLG [10], in contrast to a finite DOS evidenced in the AB-BLG.

Another characteristic feature of AB-BLG is the behaviour of the system when an electric field is applied normal to the layers. It has recently been shown that biased AB-BLG can form a Wigner crystal, due to the existence of different kinetic-energy dispersions at different electron densities [11]. The energy band gap can be tuned in proportion to the intensity of the applied bias [2], and two distinct zero-temperature quantum phases at different electron densities can be formed [11, 12].

For the AB-BLG system, the presence of significant SOC has been evidenced by topological-insulator behaviour with a finite spin Hall conductivity [13]. Moreover, it has also been shown that biased BLG may exhibit two topologically-distinct phases depending on the intensity of the Rashba spin-orbit coupling (RSOC) [14]. For weak coupling, the system exhibits a quantum-valley Hall state, which can then transition to a topological insulator in the presence of strong coupling effects. It is possible to transition between these two phases by tuning the applied electric field [14]. In the presence of strong RSOC, and for sufficiently short-range electron-electron interactions, the system minimises its energy by adopting broken-symmetry states (mostly those which break rotational symmetry) in the limit of low densities [15]. These instabilities occur due to the energy dispersion having a minimum in a region of momentum-space which is bounded by two concentric circles with finite radius (annuli) [16]. Moreover, distortions to the Fermi surface, resulting from a momentum-space change in the Fermi radius (a Pomeranchuk instability) can reduce the lattice symmetry and lead to spontaneous longitudinal currents [16].

Another stacking arrangement of BL graphene, which coexists with the AB stacking, is the AA structure where the carbon atoms are positioned directly above each other in consecutive layers. The electronic properties differ from those of AB-BLG due to the the stacking arrangement. AA stacking has been experimentally observed in disordered or pregraphitic carbon, also known as turbostratic graphite, and can be distinguished from ML graphene by so-called tilting experiments [17, 18]. However, as the space groups of AA-BLG and MLG are the same ($P6/mmm$), similarities between the two are difficult to predict.

Between the two stacking environments, the AB stacking is the most energetically-

favourable form, and is separated from the AA stacking by a small energy barrier. Despite its instability, AA-BLG has started to receive significant attention. The AA configuration shows unusual electronic properties, with two degenerate electronic and hole bands crossing at the Fermi energy [19]. This electronic structure supports several electron and electron-phonon instabilities, which include, among others, a shear-shift instability [19]. It has further been observed that small perturbations can destabilize the degenerate spectrum and generate an excitonic gap [19, 20]. .

While the AB-BLG system is well studied both experimentally and theoretically, comparatively less attention has been given to the AA stacking. In the present work, we aim to provide more insight into the electronic and vibrational properties of biased AA-BLG, and to make a comparison to the AB-system, by employing first-principles simulation techniques.

We find that while the AB system presents variations on the electronic densities as a function of the applied bias, we observe that the AA system remains unaltered when an electric field is applied. SOC effects are also considerable for the biased AB-system, with the band-gap presenting different scaling behaviours according to the field intensities. The phonon dispersions of the biased AB system shows instabilities of the out-of-plane acoustic and optic modes, when compared to the stability of these modes for the unbiased system. On the other hand, phonon dispersions of the AA system remain stable under bias, but the phonon spectrum exhibits a zone-center imaginary mode resulting form the shear-mode instability.

2. Theoretical Framework

We study the electronic structure of the two different stacking environments of the BLG system (crystal structure of AB- and AA-BLG presented in figure 1) using density-functional theory (DFT) with the Local-Density Approximation (LDA) functional. An external electric field is applied in the direction of the interlayer plane with variable magnitude. Lattice dynamics are performed within the harmonic approximation, which yields phonon frequencies and the constant-volume terms in the free energy from lattice vibrations.

2.1. Density Functional Theory

Electronic-structure calculations were performed within the pseudopotential plane-wave density-functional theory (DFT) framework, as implemented in the *Vienna Ab-initio Simulation Package* (VASP) [21, 22, 23] code. The Ceperley and Alder form of the Local-Density Approximation (LDA) functional, parametrised by Perdew and Zunger [24], was used in conjunction with projector augmented-wave (PAW) pseudopotentials [25, 26]. We selected the LDA functional because it is known to perform well at capturing the interlayer distance in graphite and multi-layer graphene allotropes, as well as the essential physics of the electronic structure, and also performs well for calculating

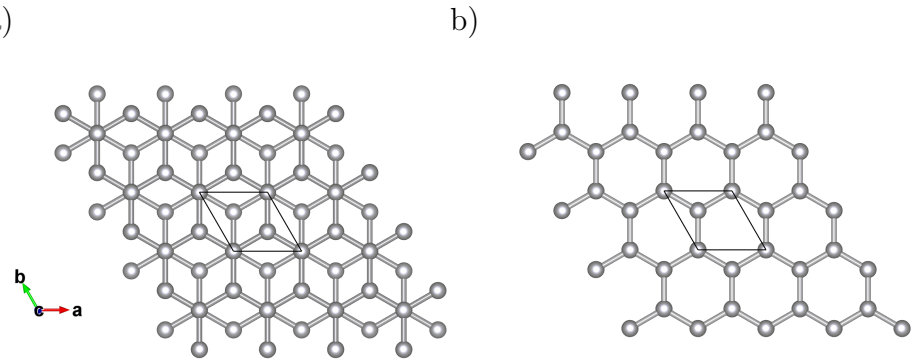

Figure 1. Supercell of the AB- (space group $P-3m1$, n^o 164; a) and AA-BLG (space group $P6/mmm$, n^o 191; b) systems, where the black line shows the unit-cell. BLG consists of two coupled monolayers of carbon atoms, each with a honeycomb crystal structure. In order to satisfy the translational and symmetry properties of the Bravais lattice, the honeycomb lattice can be seen as two triangular sublattices, mathematically labelled as inequivalent A and B lattices, each of which contains two atoms in the unit cell within each C sheet, with atom [a_1, a_2] $\in$ A and [b_1,b_2] $\in$ B for layer 1 and 2. The layers of the AB-BLG are arranged in such a way that one of the atoms from the lower-layer b_1 is directly below atom a_2 from the upper layer, and the remaining two atoms, a_1 and b_2, are shifted from each other by a vector displacement [10]. For the AA-BLG, the carbon atoms are aligned in the consecutive layers, directly above/below each other (a_1 with a_2 and b_1 with b_2).

interatomic force constants and phonon frequencies [27, 28].

A plane-wave cut-off of 800 eV was applied in all calculations; although convergence of the electronic structure was attained at a lower cut-off of $\sim$ 600 eV, a higher value was chosen to improve the description of the structural parameters and forces, which is important for accurate lattice-dynamics calculations [29]. The Brillouin zone (BZ) was sampled with Γ-centred Monkhorst-Pack meshes [30] with 44×44×1 and 90×90×1 subdivisions for AA- and AB-BLG respectively. It was found necessary to employ the denser **k**-point mesh for the AA-BLG model due to differences in the DFT electronic band structure relative to the spectra expected from tight-binding theory (section Appendix A). The vacuum spacing between periodic images along the Z direction was set to 15 Å for both configurations, and dipole corrections to the potential were applied to avoid interactions between periodic images.

Lattice-dynamics calculations were carried out using the Parlinski-Li-Kawazoe supercell finite-displacement method [31, 32], which is implemented in the Phonopy [33, 34] package; a detailed description of the theoretical implementation can be found in Refs. [35, 29]). The interatomic force constants were obtained by performing single-point force calculations on a series of symmetry-inequivalent displaced structures and fitting the resulting force/displacement curves to a harmonic function. VASP was used as the force calculator [32] and the calculations were performed on 4×4×1 supercells using a reduced **k**-point sampling mesh of 12×12×1 for both phases. For the calculations under bias, the electric field was applied during the force-constant calculations. To construct

the phonon density of states, the phonon frequencies were sampled on an interpolated 48×48×1 **q**-point mesh.

A non-analytical correction (NAC) was applied when computing the phonon-band dispersion [36] to correct for long-range Coulomb interactions. The requisite Born effective-charges and static dielectric constant were computed using the density-functional perturbation theory (DFPT) routines implemented in VASP [37]. Convergence of these quantities required increasing the **k**-point mesh for the AB system up to 80×80×1, whereas for the AA system the 90×90×1 mesh was found to be sufficient.

A bias was applied in the calculations as an external electrostatic field in the Z direction and geometries were re-optimised with different intensities of the field. Born effective-charges and dielectric tensors were calculated by considering the field perturbations. For the lattice-dynamics calculations, the bias was also applied during the calculations of the force constants.

3. Results and Discussion

The lattice parameters obtained within the LDA are a_0=2.42 Å and c_0=6.69 Å for the AB system, and a_0=2.45 Å and c_0=6.67 Å for the AA system. The intra-layer distance (C-C bond lengths) are on the order of 1.41 Å in both stacking environments, and the interlayer distance was calculated to be 3.35 Å and 3.34 Å for the AB and AA configurations, respectively. The parameters for AB-BLG are in agreement with those discussed in Ref. [38], where the calculations were also performed with DFT-LDA (intra-layer distance of 1.41 Å and interlayer distance of 3.31 Å). The present interlayer parameters also compare well to experimental results, where for the Bernal graphite the value of 3.35 Å [39] was observed. However, for the AA-BLG the present interlayer distance is found to be slightly lower than results found in literature: 3.59 Å from DFT-LDA calculations [38], and 3.55 Å from experimental observations on the AA graphite structure [40].

3.1. Electronic Spectrum from a Density-Functional and Tight-Binding Perspective

To study the electronic structure, we calculated the low-energy band dispersions using LDA-DFT with three intensities of applied electric field. The results are presented in figure 2. For the AB-BLG configuration (Figure 2.a), when $E = 0$ eV/Å, a zero-gap parabolic dispersion around the K-point is observed. The LDA-DFT electronic dispersion for the AB system shows similar features to the band-structure obtained from the tight-binding Hamiltonian (figure A1, Appendix A).

When a finite electric-field is applied perpendicular to the graphene layers in AB-BLG, the two layers are subject to inequivalent potentials. This effect breaks the inversion symmetry, resulting in the opening of a single-electron gap [2] at the K-point, which can be tuned up to mid-infrared energies ($\sim$ 300 meV) [41]. A spontaneous

a) b)

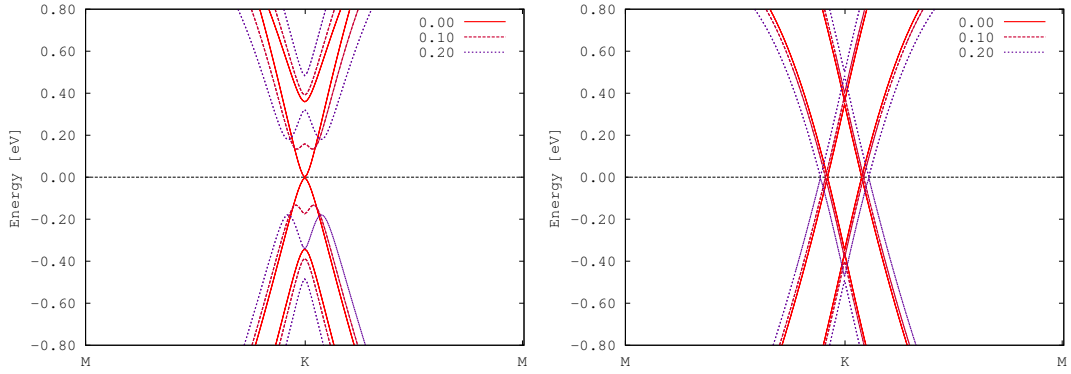

Figure 2. Low-energy DFT-LDA electronic band-structure of bilayer graphene with AB (a) and AA (b) stacking arrangements. Each dispersion is shown at different applied field intensities (label units given in eV/Å).

translation symmetry breaking also occurs, resulting in a charge separation between the inequivalent sublattices with spatial in-plane charge inhomogeneities [42, 11].

Figure 3 plots the electron charge densities of AB-BLG in the vicinity of the Fermi energy, inspection of which reveals differences between the isosurfaces without (a) and with (b) a bias applied. In the unbiased system (figure 3.a), the charge densities show hexagonal symmetry, indicating homogeneous electron delocalisation between the sublattices. On the other hand, when an interlayer electric field is applied (figure 3.b), redistribution of electron densities leads to charge separation between the A and B sublattices, leading to in-plane charge inhomogeneities [11].

The AA-stacking environment differs from the Bernal system by having a linear dispersion with two bands crossing each other at the Fermi energy [10]. Application of an external field does not alter the width of the band gap, and electronic structure remains qualitatively the same. This single-electron property seems to be quite stable to external bias both in the LDA calculations and also with a tight-binding Hamiltonian [10].

These results are consistent with the electronic dispersion calculated with the tight-binding method (figure A1), although, as noted above, obtaining a fully-converged dispersion from the DFT calculations required very dense **k**-point sampling. This is because the band crossing does not occur at a high-symmetry **k**-point, and thus a dense mesh is required in order to include sufficient sampling around the feature to accurately represent the bands in the vicinity of the Fermi energy.

Under bias, the dispersion relations of the AB system show a "Mexican hat" structure [2, 43]. With increasing field intensity, the width of the gap increases and the radius of the hat feature widens, with the two minima getting progressively further

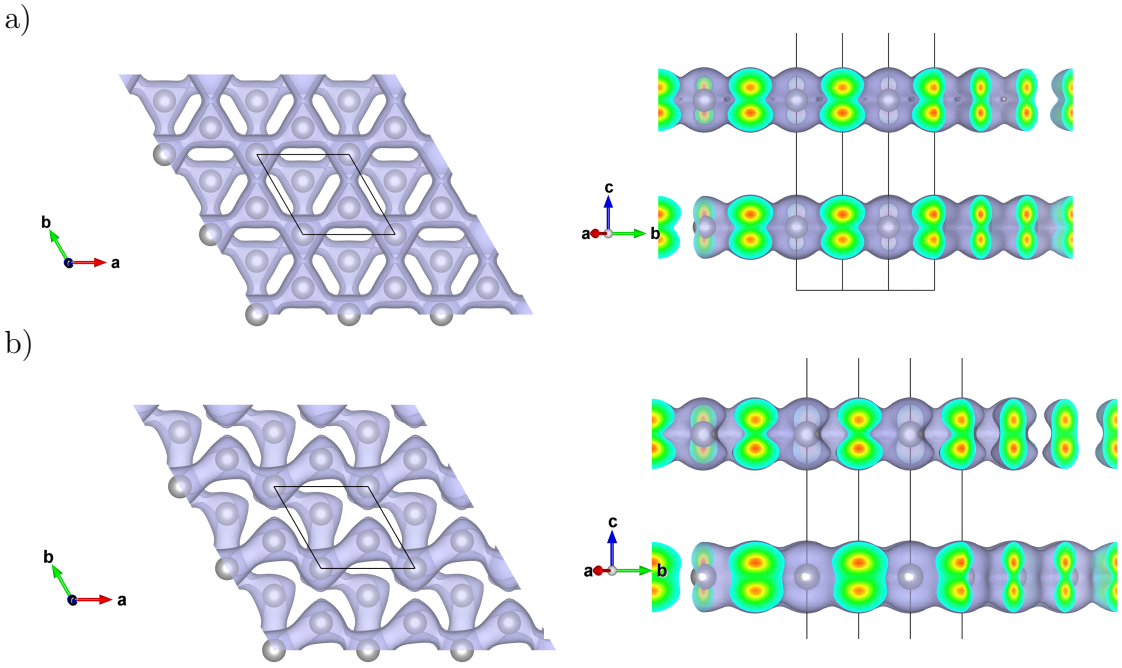

Figure 3. Two different views (top and side) of the isosurfaces (value defined at 0.016) of the electron charge densities around the Fermi energy for the AB-BLG system without (a) and with (b) an applied bias (electric field intensity of 0.05 eV/Å.

apart from the K-point [2]. This behaviour is consistent with the results from Ref. [11], which suggest that regions of the dispersion should exhibit different scaling behaviour as a function of momentum [11]. Moreover, controlling the magnitude of the gap through additional screening with a transverse electric field will afford control over the density of electrons [44].

Figure 4.a shows the electronic band-structure when spin-orbit coupling (SOC) is included in the calculations.

In the present study, we find that the bulk gap decreases when SOC is turned on, and then increases gradually for increasing field intensities (Figure 4.a) Under large filed intensities ($\sim$0.4 eV/Å), the energy dispersion recovers the Mexican hat structure, since the instability occurring at the Fermi-surface competes with the SOC interaction; the energy interaction between the layers balances the coupling interaction.

Moreover, Ref. [14] reported that the gap vanished as the SOC parameter increases, and that on further increasing the coupling parameter it then reopens with a behaviour characteristic of a band inversion, thus suggesting a topological phase transition [14]. However, since the model employed in [14] is different from the computations carried out for the presented work, a direct comparison between the two sets of results is not straightforward.

a) b)

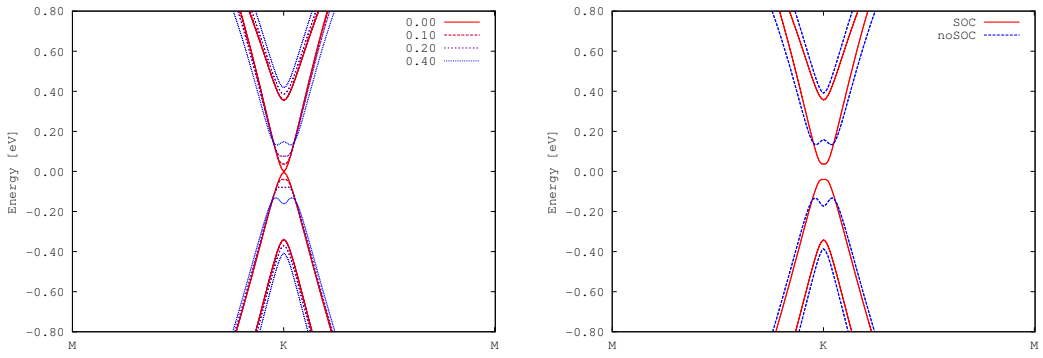

Figure 4. Low-energy DFT-LDA electronic band-structure of AB-stacked bilayer graphene. (a) Dispersions with different intensities of an applied external interlayer electric field, calculated with spin-orbit coupling. (b) Dispersions of a biased system ($E = 0.20$ eV/Å) with and without spin-orbit coupling included. Field strengths are given in eV/Å.

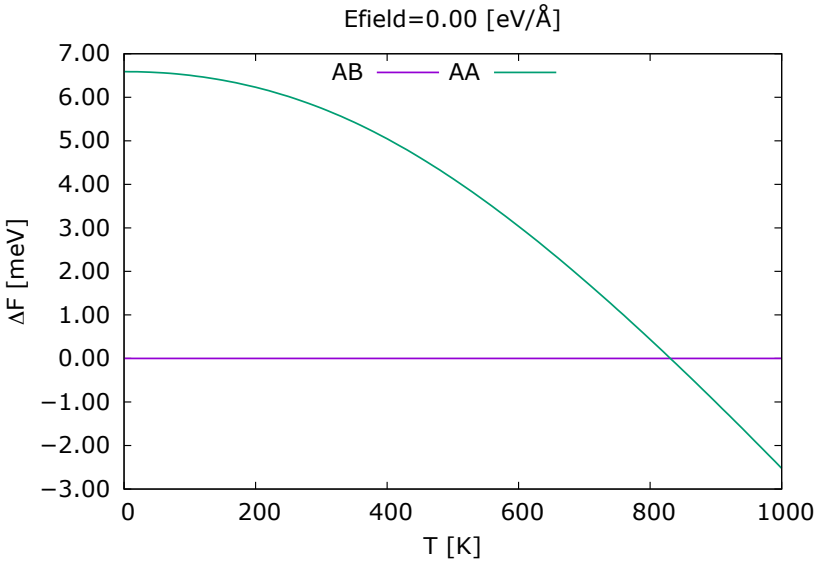

Figure 5. Relative free energy (Helmoltz) of the two graphene stacking environments, AB and AA, with no external electric-bias. The AB arrangement is calculated to be the most energetically-stable structure up to ∼800 K.

3.2. Structural Instabilities of Bilayer Graphene - Lattice-Dynamics

Figure 5 shows the constant-volume (Helmoltz) free energy of the AB and AA bilayer systems calculated without an applied bias. The energies are referenced to the lowest energy structure, which in the present calculations is the AB system. Our calculations indicate that the AA system is energetically unstable with respect to the AB phase up to approx. 800 K, above which the AA stacking becomes lower in energy.

The calculated in-plane phonon dispersion agrees well with the experimental measurements on graphite presented in [45] (Figure 6), apart from a small shift of the higher-frequency TO and LO modes. LDA calculations frequently overestimate the energies of higher-frequency phonons, but despite this difference the characteristic features of the phonon dispersion are well reproduced.

At low $\mathbf{q}$-vectors, the in-plane transverse acoustic (TA) and longitudinal acoustic (LA) modes show linear dispersions. Moreover, while the doubly-degenerate LA mode has zero frequency at the Γ-point, the TA mode (also known as the shear-mode) has a non-zero frequency at the zone-center [46] ($\nu = 0.82$ THz) (Figure 7).

The ZA mode is the flexural acoustic mode, which corresponds to out-of-plane, in-phase atomic displacements. In contrast to the TA and LA modes, the ZA branch shows a parabolic dispersion, i.e. $\nu \sim \mathbf{q}^2$, close to the Γ-point, indicating a low group velocity [47] and being a characteristic feature of layered materials [46, 47]. The existence of a flexural mode is also a signature of 2D systems, and in particular is a mode which is typically found in graphene-like systems. Since the long-wave flexural mode has the lowest frequency, it is the easiest to excite [48].

At slightly higher frequencies, the out-of-plane ZO' mode (Figure 7) can be observed, which corresponds to interlayer motion along the Z-axis (a layer-breathing mode). The other out-of-plane optic modes are characterised by the doubly degenerate ZO branch. At the Γ point, the interlayer coupling causes the LO and TO modes to split into two doubly-degenerate branches, both of which correspond to in-plane relative motion of atoms. With the exception of the ZA and ZO' modes, all the frequency branches have symmetry-imposed degeneracy at Γ (Figure 6).

Figure 8 compares the phonon dispersions of the two stacking modes. Both stacking configurations have similar mode characters, although differences emerge at the zone-centre.

For the AA system, a small phonon instability is observed at the Γ-point, which is denoted by an imaginary mode ($\nu = i1.04$ THz). This indicates that the AA-system is dynamically unstable, and prefers to adopt the AB-stacking configuration, in accordance with the free energies in Figure 5. As expected, the imaginary mode is a TA branch, which corresponds to the shear displacement of the layers with respect to one another. The ZA mode also shows instabilities in the vicinity of the zone-center, but has zero frequency at Γ.

The ZO' breathing mode of AA-stacked bilayer graphene is located in a similar frequency range to the corresponding mode in AB graphene, at $\nu = 2.16$ and $\nu = 2.25$

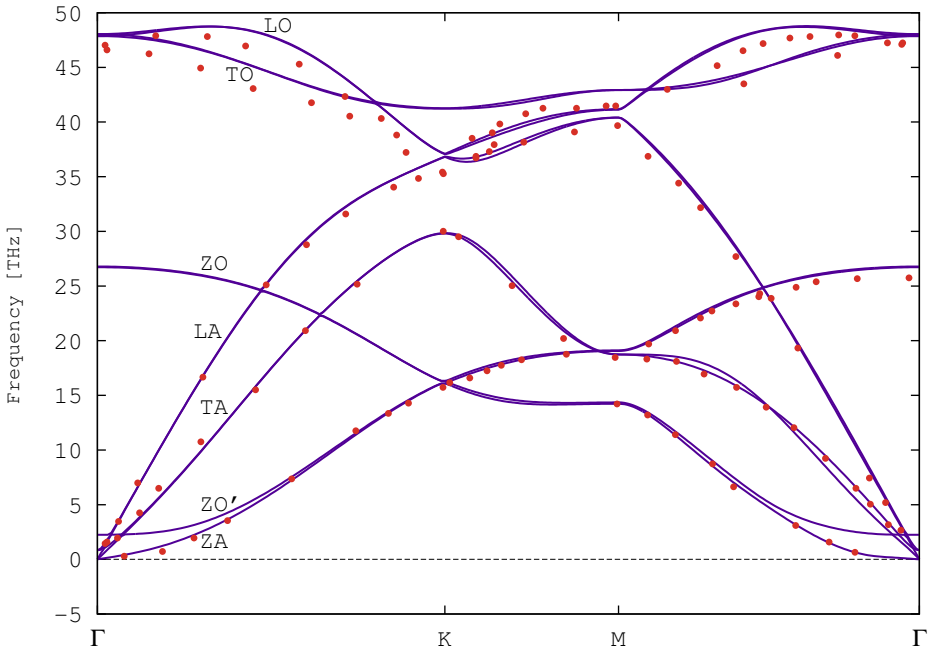

Figure 6. Phonon dispersion of AB-stacked bilayer graphene computed within the harmonic approximation (solid line). The unit cell contains four carbon atoms, leading to three acoustic (A) and $3N - 3 = 9$ optical (O) phonon branches. The calculated dispersions are compared to the in-plane phonon dispersion of graphite obtained from inelastic x-ray scattering [45] (red dots). The phonon branches are marked with the labels assigned to the Γ-point phonons.

THz, respectively. The biggest frequency differences are observed for the TO modes, which in the AB system occurs at higher frequency than in the AA configuration, with 0.72 THz of difference. This is partly because the LO/TO is larger in the AA than the AB system (0.57 and 0.18 THz, respectively).

Table 1 presents a summary of the zone-centre frequencies for the two stacking configurations.

We note that the AA phonon dispersion does not correspond to that in [49], where, in contrast to the present results, imaginary frequencies are not observed (with calculations carried out using the Born-von-Karman model of lattice dynamics for in-plane atomic coupling and the Lennard-Jones potential for interlayer coupling [49]).

The branches which originate from the out-of-plane modes at the Γ-point, i.e. ZA, ZO' and ZO, become degenerate at the K-point (Figure 8)). The in-plane LO and LA phonon branches also meet at the K-point, giving rise to a doubly-degenerate phonon band. It is also noteworthy that the dispersions of the out-of-plane modes behave linearly around the K-point in AA-BLG, whereas those in AB-BLG show a parabolic-

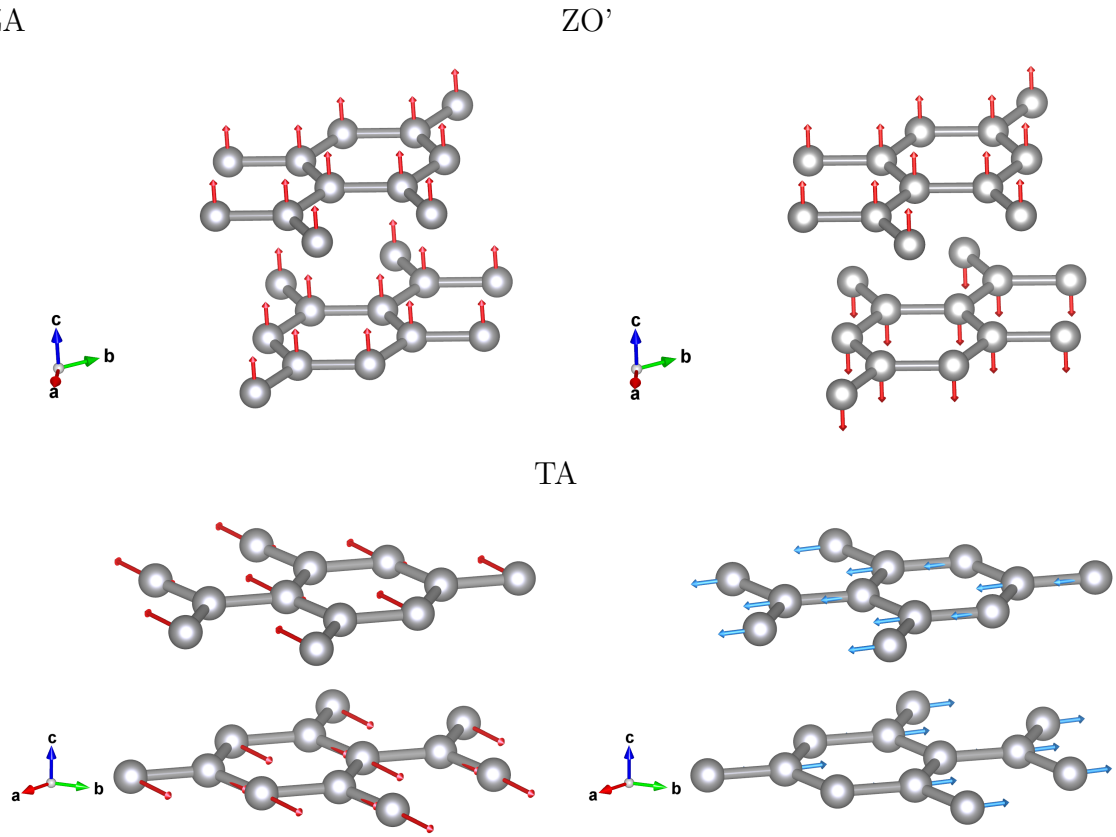

Figure 7. Eigenvectores corresponding to the vibrations in AB-stacked bilayer graphene. ZA and ZO' correspond to the out-of-plane vibrations, while TA denotes the degenerate in-plane transverse-acoustic modes.

Table 1. Frequencies (THz) of the Γ-point phonon modes in AB- and AA-stacked bilayer graphene.

Mode	ZA	ZO'	TA	LA	ZO	TO	LO
AB	0.00	2.25	0.82	0.00	26.72	47.86	48.04
AA	0.00	2.16	i 1.04	0.00	26.82	47.14	47.71

like dispersion similar to that suggested in [49]. Features in the electronic spectra near the K-point in the two BLG systems are therefore also reflected in the phonon spectra (c.f. Figures 2 and 8).

Further lattice-dynamics calculations were carried out to investigate the effect of electric fields on the phonon dispersions (Figure 9). Non-analytical corrections to the dynamical matrix at $q \to 0$ were considered in all calculations. We find that the dispersion of the AA system is relatively insensitive to the applied external bias, and that for all applied fields the Γ-point instability persists.

In comparison, the low-frequency branches of the AB band-structure show a significant response to the field (Figure 9.a). This effect results from the inclusion of non-analytical corrections; when these corrections are not included, the dispersions

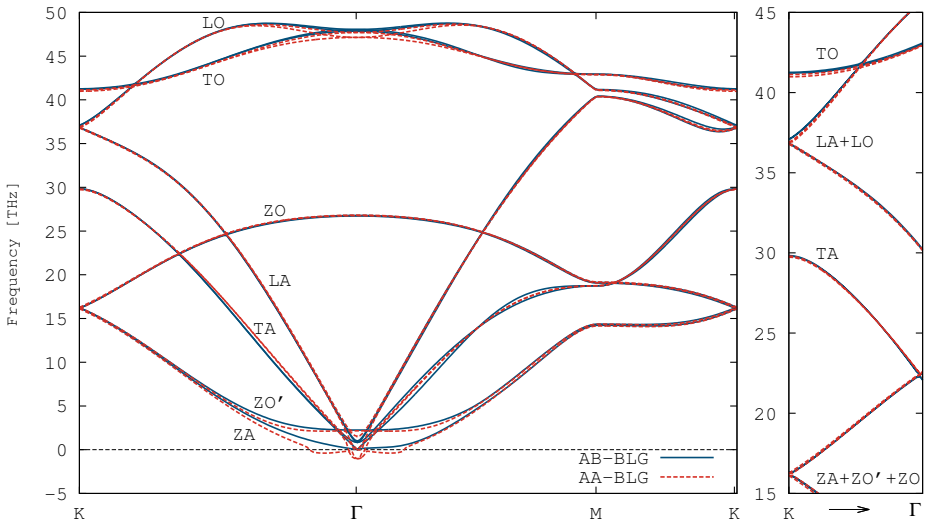

Figure 8. Phonon dispersions of the AB- and AA-stacked bilayer graphene systems computed with the harmonic approximation (blue solid and red dashed lines, respectively). The right-hand panel shows the dispersion along the K-Γ path. The phonon branches are denoted by the symbols of the Γ-point phonons, several of which become degenerate at the K-point.

are relatively unaffected by the bias. The layer-breathing mode (ZO') displays a discontinuity at the Γ-point, with different frequencies for different directions of approach. Moreover, the flexural-acoustic (ZA) mode shows instabilities in the vicinity of the zone-centre, but continue to show zero frequency at the Γ-point. Since the long-wave flexural mode has the lowest frequency, it is the easiest to excite [48] and is therefore more sensitive to the bias. At the K-point (Figure 9, inset), as occurs for the electronic band-structure the degeneracy of the out-of-plane modes split, with the magnitude of the splitting depending on the size of the applied bias.

4. Conclusions

In summary, we have performed a detailed first-principles study of the effect of applied fields on the electronic structure and lattice dynamics of bilayer graphene.

Application of an external field to the AB-stacked bilayer graphene system leads to drastic changes in the electronic properties, leading to the opening of the gap and asymmetry in the dispersion. This in turn induces in-plane inhomogeneities in the charge distribution on the sublattices, and the Coulomb interaction between electrons will thus cause a potential difference between the layers. Our results therefore show that the electron density can be controlled by tuning the band-gap width and dispersion asymmetry.

a)

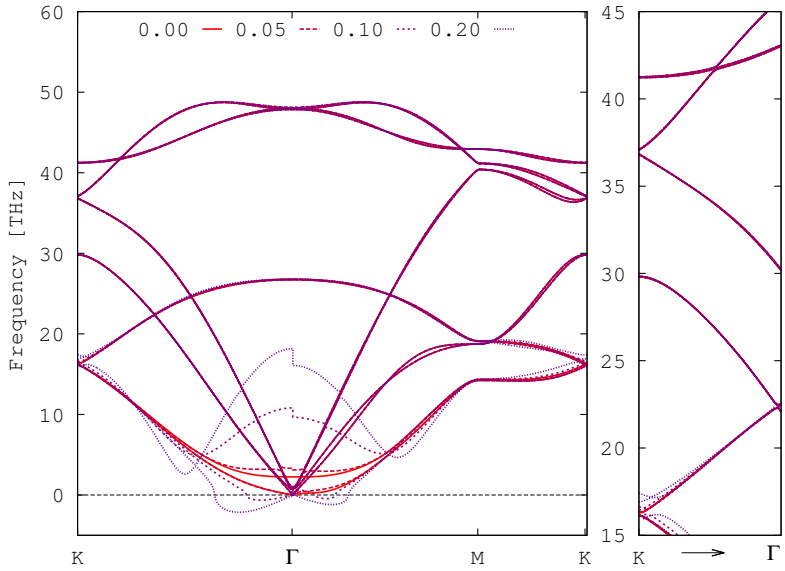

b)

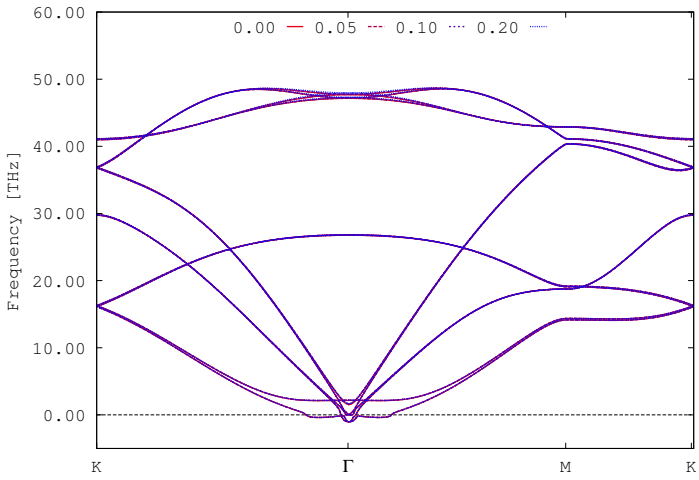

Figure 9. Harmonic phonon dispersions of the AB- (a) and AA-stacking (b) configurations of bilayer graphene under different applied bias. The right-hand panel in (a) shows the dispersion along the K-Γ segment. The AA system shows doubly-degenerate imaginary modes at the zone-center, which is consistent with the alternative AB stacking being the most favourable arrangement. Non-analytical corrections have been applied to the dispersions of both systems. The ZA and ZO' modes on the AB-BLG change significantly under bias, whereas the applied field has comparatively little effect on the dispersion of the AA-BLG system. Electric fields are given in eV/Å.

Spin-orbit coupling has a significant effect on the dispersion as short-range electron-electron correlations become important. The Mexican-hat structure disappears under low bias, and the energy gap decreases. At larger field strength, the asymmetry in the dispersion persists, since the energy scale set by the Fermi-surface instability is minimized.

On the other hand, the electronic structure of the AA system is relatively stable under bias.

As for its electronic structure, applied fields cause the phonon dispersions of the AB-stacked system to change significantly when non-analytical corrections for long-range Coulomb interactions are taken into account. These corrections mainly affect the lower-frequency out-of-plane ZA and ZO' modes. The phonon dispersion of the AA system shows degenerate imaginary modes at the Γ point, indicating the presence of a phonon instability. The dispersion of this stacking configuration is relatively insensitive to bias and does not change significantly in response to an applied field.

In order to obtain better consistency with available literature, we would need to go beyond LDA functional. The ground-state is likely to have additional broken-symmetry configurations, and the lifting of spin and valley degeneracies may depend on long-range fluctuations, effects which are not well captured by local DFT functionals. For example, in the literature it has been observed that the AA stacking configuration may be stabilised by an excitonic gap [19]. To study such effects, one would need to resort to the two-body Green function method (Bethe-Salpeter equation), a possibility which we are currently exploring.

Acknowledgments

This work was supported by EPSRC Programme Grants (nos. EP/K004956/1 and EP/K016288/1) and the ERC (Grant No. 277757). We acknowledge use of the ARCHER supercomputer through the PRACE Research Infrastructure (award no. 13DECI0313). The authors also acknowledge computing support from the University of Bath Computing Services, which maintains the Balena HPC cluster.

Appendix A. Tight-Binding Hamiltonian

To study the effects of an applied electric field on bilayer graphene, we begin by describing pure bilayer graphene system with Bernal stacking, considering only the t_z interlayer hopping amplitude, restricted to the nearest-neighbour carbon atoms. An electric bias $V = eEd$ is applied in the direction perpendicular to the layers, where e is the electron charge, E the applied electric field, and d the interlayer spacing [2]. The Fermi operators, written as:

$$a_{\mathbf{k}j} = N^{-1} \sum_n e^{\imath \mathbf{k}\cdot\mathbf{n}} a_{\mathbf{n}j} \qquad b_{\mathbf{k}j} = N^{-1} \sum_n e^{\imath \mathbf{k}\cdot\mathbf{n}} b_{\mathbf{n}j} \tag{A.1}$$

represent plane-wave states with momentum $\mathbf{k}$. The indices j refer to the layers in the nth unit-cell, $a_{\mathbf{n}j}$ and $b_{\mathbf{n}j}$ are operators referring to A- and B-type sites in the lattice (figure 1), and N is the number of cells in a layer. A 4−spinor is formed by:

$$\psi^\dagger_{\mathbf{k}} = \left(a^\dagger_{\mathbf{k}1}, b^\dagger_{\mathbf{k}1}, a^\dagger_{\mathbf{k}2}, b^\dagger_{\mathbf{k}2} \right). \tag{A.2}$$

The Hamiltonian is given in the second-quantized form by:

$$H_0 = \sum_{\mathbf{k}} \psi^\dagger_{\mathbf{k}} \hat{H}_{\mathbf{k}} \psi_{\mathbf{k}} \tag{A.3}$$

where the matrix has the form:

$$\hat{H}_{\mathbf{k}} = \begin{pmatrix} \frac{V}{2} & \gamma_{\mathbf{k}} & 0 & t_z \\ \gamma^\dagger_{\mathbf{k}} & \frac{V}{2} & 0 & 0 \\ 0 & 0 & -\frac{V}{2} & \gamma_{\mathbf{k}} \\ t_z & 0 & \gamma^\dagger_{\mathbf{k}} & -\frac{V}{2} \end{pmatrix} \tag{A.4}$$

The term $\gamma_{\mathbf{k}} = t \sum_{\boldsymbol{\delta}} e^{\imath \mathbf{k}\cdot\boldsymbol{\delta}}$ is related to the in-plane hopping amplitude, t, over the nearest-neighbour vectors $\boldsymbol{\delta}$ and defined as $t \approx 3$ according to experimental and first principles calculations suggested in Refs. [50] and [51]). The variable $\xi_{\mathbf{k}}$ is defined as $\hbar v_F(\mathbf{k} - K)$, with the Fermi velocity defined as $v_F = 3ta/2\hbar \approx 10^{-6}\mathrm{ms}^{-1}$, and a being the intra-layer distance between next-neighbour atoms of different sublattices and $\hbar$ the Planck constant [2]. The interlayer hopping amplitude, t_z, is related to t by the relation $t_z = t/10$ [50].

In the vicinity of the Dirac points $\pm K$ is defined by $\pm(4\pi/3\sqrt{3}a, 0)$ and $\gamma_{\mathbf{k}} \approx \xi_{\mathbf{k}} e^{\imath\varphi_{\mathbf{k}}}$, with $\varphi_{\mathbf{k}} = \tan^{-1} k_y/(k_x - K_x)$ [2]. After diagonalizing the matrix in Eq. A.4, and considering that the dispersion in the vicinity of the Dirac point is defined along a circle around each Dirac point, $\xi_{\mathbf{k}} \equiv \xi$, with maximum radius defined as $\hbar v_F \sqrt{K/a}$ [2], we obtain for the four bands:

$$\begin{aligned} \varepsilon_1(\xi) &= \pm \frac{1}{2} \sqrt{2t_z^2 + V^2 + 4\xi^2 + 2\sqrt{t_z^4 + 4(t_z^2 + V^2)\xi^2}} \\ \varepsilon_2(\xi) &= \pm \frac{1}{2} \sqrt{2t_z^2 + V^2 + 4\xi^2 - 2\sqrt{t_z^4 + 4(t_z^2 + V^2)\xi^2}} \end{aligned} \tag{A.5}$$

a) b)

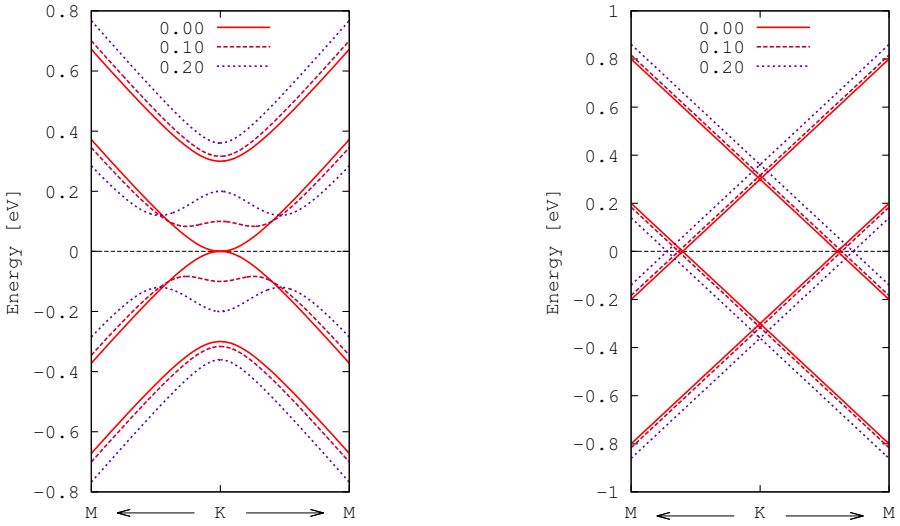

Figure A1. Low-energy tight-binding electronic band-structure of bilayer graphene in the AB (a) and AA (b) stacking arrangements. Dispersions are calculated for different intensities of V.

where ε_1 and ε_2 refer to the external and internal bands, respectively [2].

The bias-controlled gap will therefore result in:

$$\varepsilon_{\rm g} = \pm \frac{V}{2\sqrt{1+(\frac{V}{t_z})^2}}. \tag{A.6}$$

For the AA-BLG, the calculations are similar, although the matrix takes the form:

$$\hat{H}_{\mathbf{k}} = \begin{pmatrix} \frac{V}{2} & \gamma_{\mathbf{k}} & t_z & 0 \\ \gamma_{\mathbf{k}}^{\dagger} & \frac{V}{2} & 0 & t_z \\ t_z & 0 & -\frac{V}{2} & \gamma_{\mathbf{k}} \\ 0 & t_z & \gamma_{\mathbf{k}}^{\dagger} & -\frac{V}{2} \end{pmatrix} \tag{A.7}$$

and hence the eigenenergies will result in

$$\begin{aligned} \varepsilon_1(\xi) &= \pm \frac{1}{2}\sqrt{4t_z^2+V^2}+\xi \\ \varepsilon_2(\xi) &= \pm \frac{1}{2}\sqrt{4t_z^2+V^2}-\xi. \end{aligned} \tag{A.8}$$

[1] C. Berger, Z. Song, T. Li, X. Li, A. Y. Ogbazghi, R. Feng, Z. Dai, A. N. Marchenkov, E. H. Conrad, P. N. First, and W. A. de Heer. Ultrathin Epitaxial Graphite: 2D Electron Gas Properties and a Route Toward Graphene-Based Nanoelectronics. *J. Phys. Chem.*, 108:19912, 2004.

[2] M. C. Santos Y. G. Pogorelov and V. M. Loktev. Electric Bias Control of Impurity Effects in Bilayer Graphene. *Phys. Rev. B*, 92:075401, 2015.

[3] K. S. Novoselov, E. McCann, S. V. Morozov, V. I. Fal'ko, M. I. Katsnelson, U. Zeitler, D. Jiang, F. Schedin, and A. K. Geim. Unconventional Quantum Hall Effect and Berry's Phase of 2π in Bilayer Graphene. *Nature Physics*, 2:177, 2006.

[4] G. Fiori and journal = IEEE Electron Device Lett. volume = 30 pages = 1096 year = 2009 G. Iannaccone, title = Ultralow-Voltage Bilayer Graphene Tunnel FET.

[5] journal = Nature Nanot. volume = 12 pages = 895 year = 2017 M. Kühne, title = Ultrafast Lithium Diffusion in Bilayer Graphene.

[6] J.-Q. Huang G.-L. Tian J.-Q. Nie H.-J. Peng M.-Q. Zhao, Q. Zhang and journal = Nature Comms. volume = 5 pages = 3410 year = 2014 F. Wei, title = Unstacked Double-Layer Templated Graphene for High-Rate Lithium–Sulphur Batteries.

[7] H. Yan. Bilayer Graphene: Physics and Application Outlook in Photonics. *Nanophotonics*, 4:115, 2015.

[8] E. Akbari, R. Yusof, M. T. Ahmadi, A. Enzevaee, M. J. Kiani, H. Karimi, and M. Rahmani. Bilayer Graphene Application on NO_2 Sensor Modelling. *J. Nanomat.*, 2014:1, 2014.

[9] S. V. Morozov D. Jiang M. I. Katsnelson I. V. Grigorieva S. V. Dubonos A. A. Firsov K. S. Novoselov, A. K. Geim. Two-Dimensional Gas of Massless Dirac Fermions in Graphene. *Nature*, 438:197, 2005.

[10] A. L. Rakhmanov F. Nori A. V. Rozhkov, A. O. Sboychakov. Electronic Properties of Graphene-Based Bilayer Systems. *Phys. Rep.*, 648.

[11] P. G. Silvestrov and P. Recher. Wigner Crystal Phases in Bilayer Graphene. *Phys. Rev. B*, 95:075438, Feb 2017.

[12] Gregg Jaeger. The ehrenfest classification of phase transitions: Introduction and evolution. *Archive for History of Exact Sciences*, 53(1):51–81, May 1998.

[13] E. McCann and M. Koshino. The Electronic Properties of Bilayer Graphene. *Reports on Progress in Physics*, 76(5):056503.

[14] Zhenhua Qiao, Wang-Kong Tse, Hua Jiang, Yugui Yao, and Qian Niu. Two-Dimensional Topological Insulator State and Topological Phase Transition in Bilayer Graphene. *Phys. Rev. Lett.*, 107:256801, Dec 2011.

[15] Erez Berg, Mark S. Rudner, and Steven A. Kivelson. Electronic Liquid Crystalline Phases in a Spin-Orbit Coupled Two-Dimensional Electron Gas. *Phys. Rev. B*, 85:035116, Jan 2012.

[16] Jeil Jung, Marco Polini, and A. H. MacDonald. Persistent Current States in Bilayer Graphene. *Phys. Rev. B*, 91:155423, Apr 2015.

[17] J.-C. Charlier, J.-P. Michenaud, and X. Gonze. First-Principles Study of the Electronic Properties of Simple Hexagonal Graphite. *Phys. Rev. B*, 46:4531–4539, Aug 1992.

[18] Zheng Liu, Kazu Suenaga, Peter J. F. Harris, and Sumio Iijima. Open and Closed Edges of Graphene Layers. *Phys. Rev. Lett.*, 102:015501, Jan 2009.

[19] A. L. Rakhmanov, A. V. Rozhkov, A. O. Sboychakov, and Franco Nori. Instabilities of the *aa*-Stacked Graphene Bilayer. *Phys. Rev. Lett.*, 109:206801, Nov 2012.

[20] R. S. Akzyanov, A. O. Sboychakov, A. V. Rozhkov, A. L. Rakhmanov, and Franco Nori. *aa*-Stacked Bilayer Graphene in an Applied Electric Field: Tunable Antiferromagnetism and Coexisting Exciton Order Parameter. *Phys. Rev. B*, 90:155415, Oct 2014.

[21] G. Kresse and J. Furthmuller. Efficient iterative schemes for ab initio total-energy calculations using a plane-wave basis set. *Phys. Rev. B"*, 54:11169, 1996.

[22] G. Kresse and J. Hafner. *Ab initio* molecular dynamics for liquid metals. *Phys. Rev. B*, 47:R558, 1993.

[23] G. Kresse and J. Furthmuller. Efficiency of ab-initio total energy calculations for metals and

semiconductors using a plane-wave basis sefficient iterative schemes for ab initio total-energy calculations using a plane-wave basis set. *Compt. Mat. Sci.*, 6:15, 1996.

[24] J. P. Perdew and Alex Zunger. Self-interaction correction to density-functional approximations for many-electron systems. *Phys. Rev. B*, 23:5048–5079, May 1981.

[25] G. Kresse and D. Joubert. From ultrasoft pseudopotentials to the projector augmented-wave method. *Phys. Rev. B*, 59:1758–1775, Jan 1999.

[26] P. E. Blöchl. Projector augmented-wave method. *Phys. Rev. B*, 50:17953–17979, Dec 1994.

[27] Lianhua He, Fang Liu, Geoffroy Hautier, Micael J. T. Oliveira, Miguel A. L. Marques, Fernando D. Vila, J. J. Rehr, G.-M. Rignanese, and Aihui Zhou. Accuracy of Generalized Gradient Approximation Functionals for Density-Functional Perturbation Theory Calculations. *Phys. Rev. B*, 89:064305, Feb 2014.

[28] Fabio Favot and Andrea Dal Corso. Phonon Dispersions: Performance of the Generalized Gradient Approximation. *Phys. Rev. B*, 60:11427–11431, Oct 1999.

[29] E. Lora da Silva, Jonathan M. Skelton, Stephen C. Parker, and Aron Walsh. Phase Stability and Transformations in the Halide Perovskite $CsSnI_3$. *Phys. Rev. B*, 91:144107, Apr 2015.

[30] H. J. Monkhorst and J. D. Pack. Special Points for Brillouin-Zone Integrations. *Phys. Rev. B*, 13:5188, 1976.

[31] K. Parlinski, Z. Q. Li, and Y. Kawazoe. First-Principles Determination of the Soft Mode in Cubic ZrO_2. *Phys. Rev. Lett.*, 78:4063, 1997.

[32] L. Chaput, A. Togo, I. Tanaka, and G. Hug. Phonon-phonon interactions in transition metals. *Phys. Rev. B*, 84:094302, 2001.

[33] A Togo and I Tanaka. First principles phonon calculations in materials science. *Scr. Mater.*, 108:1, Nov 2015.

[34] A. Togo, F. Oba, and I. Tanaka. First-principles calculations of the ferroelastic transition between rutile-type and $CaCl_2$-type SiO_2 at high pressures. *Phys. Rev. B*, 78:134106, 2008.

[35] J. M. Skelton, S. C. Parker, A. Togo, I. Tanaka, and A. Walsh. Thermal physics of the lead chalcogenides PbS, PbSe, and PbTe from first principles. *Phys. Rev. B*, 89:205203, 2014.

[36] P. Y. Yu and M. Cardona. *Fundamentals of Semiconductors: Physics and Materials Properties.* Number pp. 104. 1996.

[37] M. Gajdoš, K. Hummer, G. Kresse, J. Furthmüller, and F. Bechstedt. Linear Optical Properties in the PAW Methodology. *Phys. Rev. B*, 73:045112, 2006.

[38] Yuehua Xu, Xiaowei Li, and Jinming Dong. Infrared and Raman Spectra of AA-Stacking Bilayer Graphene. *Nanotechnology*, 21(6):065711.

[39] M. Hanfland, H. Beister, and K. Syassen. Graphite Under Pressure: Equation of State and First-Order Raman Modes. *Phys. Rev. B*, 39:12598–12603, Jun 1989.

[40] Jae-Kap Lee, Seung-Cheol Lee, Jae-Pyoung Ahn, Soo-Chul Kim, John I. B. Wilson, and Phillip John. The Growth of AA Graphite on (111) Diamond. *The Journal of Chemical Physics*, 129(23):234709, 2008.

[41] Eduardo V. Castro, K. S. Novoselov, S. V. Morozov, N. M. R. Peres, J. M. B. Lopes dos Santos, Johan Nilsson, F. Guinea, A. K. Geim, and A. H. Castro Neto. Biased Bilayer Graphene: Semiconductor with a Gap Tunable by the Electric Field Effect. *Phys. Rev. Lett.*, 99:216802, Nov 2007.

[42] G. Semenoff. Condensed-Matter Simulation of a Three-Dimensional Anomaly. *Phys. Rev. Lett.*, 53:2449, 1984.

[43] Brian Skinner, B. I. Shklovskii, and M. B. Voloshin. Bound State Energy of a Coulomb Impurity in Gapped Bilayer Graphene. *Phys. Rev. B*, 89:041405, Jan 2014.

[44] Edward McCann. Asymmetry Gap in the Electronic Band Structure of Bilayer Graphene. *Phys. Rev. B*, 74:161403, Oct 2006.

[45] M. Mohr, J. Maultzsch, E. Dobardžić, S. Reich, I. Milošević, M. Damnjanović, A. Bosak, M. Krisch, and C. Thomsen. Phonon Dispersion of Graphite by Inelastic X-Ray Scattering. *Phys. Rev. B*, 76:035439, Jul 2007.

[46] Phonons in Bilayer Graphene. http://tkea.com.ua/siet/archive/2013-t2/130.pdf.

[47] Y. Chen S. Li. Thermal Transport and Anharmonic Phonons in Strained Monolayer Hexagonal Boron Nitride. *Scient. Rep.*, 7.

[48] S. V. Morozov D. Jiang M. I. Katsnelson I. V. Grigorieva S. V. Dubonos A. A. Firsov K. S. Novoselov, A. K. Geim. A Review on the Flexural Mode of Graphene: Lattice Dynamics, Thermal Conduction, Thermal Expansion, Elasticity and Nanomechanical Resonance. *J. Phys.: Condens. Matter*, 27:083001, 2015.

[49] Alexandr I. Cocemasov, Denis L. Nika, and Alexander A. Balandin. Phonons in Twisted Bilayer Graphene. *Phys. Rev. B*, 88:035428, Jul 2013.

[50] E. V. Castro, N .M. R. Peres, J. M. B. Lopes dos Santos, F. Guinea, and A. H. Castro Neto. *Strongly Correlated Systems, Coherence and Entanglement.* World Scientific Publishing Co. Pte. Ltd., 2007.

[51] J. C. Charlier, X. Gonze, and J. P. Michenaud. First-principles study of the electronic properties of graphite. 43:4579, 1991.

Chapter 6

Conclusions and Perspective

Temos de fazer, o que devemos fazer, para depois fazer o que temos de fazer
Unknown author

Ab-initio calculations within the framework of density functional theory (DFT) can yield high-quality results for a large variety of systems. However, DFT calculations are mostly limited to observables related to the electronic ground-state, while phenomena that occur when the system is perturbed, are often not correctly described.

Most theoretical calculations do not consider temperature effects; however, the study of materials at high-temperature, in particular the dynamic and thermodynamic properties of solids, requires accounting for the interatomic forces that atoms exert on each other, which depend upon the interaction between phonons (lattice vibrations).

The work carried out for the present thesis project involved not only the computation of the ground-state properties of materials, but we have also employed other techniques to probe temperature effects on phase-changing materials, such as lattice dynamics. Within this methodology it is possible to compute the structural properties as a function of temperature, giving a first-principles estimate of the temperature dependence of the lattice volume, thermal-expansion coefficient, and also thermoelastic properties [16].

In this sense, the anharmonic effects needed to account for thermal expansion are introduced by the quasi-harmonic approximation (QHA), in which the thermal expansion of the crystal lattice is obtained from the volume dependence of the phonon frequencies. However, it is also important to mention that the QHA is only considered to be valid up to 2/3 of the melting temperature, above which higher-order anharmonic effects become more prominent. We would thus expect that the high-temperature properties obtained from the QHA to have an error margin to some extent.

In this sense, molecular dynamics (MD) is an alternative method, proposed to treat the dynamics of strongly anharmonic lattices. The MD method allows estimating the lattice an-

harmonicity contribution in the structural instability in materials perturbed by extreme conditions, such as high-temperatures. This could be of particular importance to unveil the mechanisms of phase transitions; i.e., when the atomic displacements from the equilibrium positions may become considerable [134, 135]. Thus the possibility of employing higher-order phonon-phonon interactions (i.e., molecular dynamics) would come as an alternative to provide further insights on the phase-transition of the materials studied during this thesis.

The perovskite crystal manifests a huge variety of properties, because the majority of cubic perovskites are (dynamically) unstable, and the energy of the system is lowered mainly due to structural distortions, passing through one or more phase transitions and, hence providing complex phase diagrams. These properties include among others, ferroelectricity, ferromagnetism, piezoelectricity, multiferroicity, metal-insulator transitions [136].

For the particular case of $CsSnI_3$ further computations will be applied in order to destabilise the Pnma structure, in an attempt to search for a ferroelectric ground-state phase. It has been observed that by *artificially* removing the X_5^+ mode for perovskite oxides, it was possible to induce a ferroelectric ground-state. The X_5^+ mode is responsible for the displacement of the A-cation which accommodates the octahedra rotations. It has been argued that this would be the mode responsible for suppressing ferroelectricity rather than the expected rotations [136]. It is therefore possible to apply the knowledge gained in our analysis of the Pnma structure of $CsSnI_3$ to probe for mechanisms which will allow for *freezing* the mode responsible for the rattling of the Cs cation, which is most likely to occur for materials that are expected to have large rotations [136]. These mechanisms may include external perturbations to the system, such as pressure, electric fields, etc.

GeTe has at the same time the structural simplicity but a complex range of properties which require several tools in order to study and understand these properties. From a microscopic perspective, lattice dynamics allows one to study the nature of the phase transition, which is still today a area of intense debate for this material. With many-body perturbation theory, more specifically QSGW, allows one to yield an improved electronic-band structure and probe the spin-splitting of the bands due to the spin-orbit interactions. From QSGW it was also possible to extract further information regarding the dynamics of the Rashba splitting, crystal-field splittings and effective masses, all as a function of the polar mode. From a macroscopic perspective, the Landau theory of phase transition also allows bridging from the microscopic perspective and provides a more complete overview of the paraelectric-to-ferroelectric phase transition.

Moreover, it was possible to conclude that by applying pressure on the crystal structure of GeTe, the ferroelctricity can be suppressed. This effect arises due to the confinement of the Ge

atom at the centrosymmetric position. Further interest regarding the ferroelctric phase may be considered by perturbing the system with external fields (electric and/or magnetic) and observe the effects upon the spontaneous polarisation. For example, by applying an electric field in the direction of the polarisation it may be possible to promote the stability of the cubic phase.

Bilayer graphene is yet another system exhibiting structural simplicity, built with only four atoms in the unit-cell, but presenting a panoply of complex properties. These are mostly evidenced for the AB stacking environment, when an external bias is turned on. Not only is it possible to tune the width of the band-gap, but special features emerge in the electronic band-structure due to the variation of the electron density in the different sublattices.

Interest would thus lie in obtaining a phase diagram for the biased AB-system, for interactions that fall off the methodology used in the present work. Resorting to other methods, such as non-local functionals of the density (i.e. HSE06) or GW, it will be possible to obtain a better description of the dynamic correlations and long-range fluctuations of the systems. The AA-BLG cannot be overlooked as well, since the ground-state behaviour, with applied bias is still not fully understood. It has been argued about the possibility of stabilising the ground-state, through the opening of an excitonic gap, and coexistence of an antiferromagentic ordering [137], features that cannot be observed within the LDA approach.

Moreover, interest also lies in employing third order phonon interactions to compute the lattice thermal conductivity. Since the electric-field induces the opening of an electronic band-gap for the AB system, leading to a semimetal-to-semiconductor phase transition, this effect will thus alter the thermal conductivity between the unbiased and biased systems. For the AA system, the phonon and electronic band-structure remain practically unchanged under different biases. On the other hand, the thermal conductivity may be affected due to disorder introduced in the system thus altering the scattering rate of the phonon-phonon collisions [138].

Another application for BLG is to further study the electron-phonon coupling mechanisms near the Γ- and K-points. Mainly for the biased systems which should provide information about the modifications of the phonon and electronic structure of BLG due to the applied field.

Bibliography

[1] F. Nogueira, A. Castro, and M. A. L. Marques. *A Primer in Density Functional Theory*, chapter 6, page 218. Springer, 2002.

[2] Peter E. Blöchl, Clemens J. Först, and Johannes Schimpl. Projector augmented wave method:ab initio molecular dynamics with full wave functions. *Bulletin of Materials Science*, 26(1):33–41, Jan 2003.

[3] Lpaw basis functions. http://www2.mpi-halle.mpg.de/theory_department/research/elk_code_development/. Last accessed: 15/01/2018.

[4] J. P. Perdew, A. Ruzsinszky, J. Tao, V. N. Staroverov, G. E. Scuseria, and G. I. Csonka. Prescription for the design and selection of density functional approximations: More constraint satisfaction with fewer fits. *The Journal of Chemical Physics*, 123(6):062201, 2005.

[5] R. W. Godby and P. García-González. *A Primer in Density Functional Theory*, chapter 5. Springer, 2002.

[6] G. Rohringer K. Held, C. Taranto and A. Toschi. *The LDA+DMFT approach to strongly correlated materials. Modeling and Simulation Vol. 1*, chapter 13. Verlag des Forschungszentrum Jülich, 2011.

[7] M. van Schilfgaarde, Takao Kotani, and S. Faleev. Quasiparticle self-consistent *gw* theory. *Phys. Rev. Lett.*, 96:226402, Jun 2006.

[8] M. Shishkin, M. Marsman, and G. Kresse. Accurate quasiparticle spectra from self-consistent gw calculations with vertex corrections. *Phys. Rev. Lett.*, 99:246403, Dec 2007.

[9] M. T. Dove. Theory of Displacive Phase Transitions in Minerals. *American Mineralogist*, 82:213, 1997.

[10] Physics of ferroelectrics. http://www.tcm.phy.cam.ac.uk/~pbl21/ferroelectrics/ferro.pdf.

[11] Symmmodes. http://www.cryst.ehu.es/cryst/symmodes.html.

[12] Cesar Capillas, Eli Kroumova, Mois I. Aroyo, J. Manuel Perez-Mato, Harold T. Stokes, and Dorian M. Hatch. *SYMMODES*: a Software Package for Group-Theoretical Analysis of Structural Phase Transitions. *J. App. Crystall.*, 36(3 Part 2):953–954, Jun 2003.

[13] T. Fliessbach. *Curso de Física Estatística*, chapter 18. Fundação Calouste Gulbenkian, 3rd edition, 2000. Translated to portuguese from Statistische Physik, T. Fliessbach, Specktrum Akademischer Verlag GmbH, Berlim (1999), by J. da Providência, Jr.

[14] L. y. Huang and W. R. L. Lambrecht. Electronic Band Structure, Phonons, and Exciton Binding Energies of Halide Perovskites $CsSnCl_3$, $CsSnBr_3$, and $CsSnI_3$. *Phys. Rev. B*, 88:165203, 2013.

[15] C. Yu, Y. Ren, Z. Chen, and K. Shum. First-principles study of structural phase transitions in $CsSnI_3$. *J. Appl. Phys.*, 114:163505, 2013.

[16] E. Lora da Silva, Jonathan M. Skelton, Stephen C. Parker, and Aron Walsh. Phase Stability and Transformations in the Halide Perovskite $CsSnI_3$. *Phys. Rev. B*, 91:144107, Apr 2015.

[17] Silvia Picozzi. Ferroelectric rashba semiconductors as a novel class of multifunctional materials. *Front. Phys.*, 2:10, 2014.

[18] D. Di Sante, P. Barone, R. Bertacco, and S. Picozzi. Correction: Electric Control of the Giant Rashba Effect in Bulk GeTe. *Advanced Materials*, 25(27):3625–3626, 2013.

[19] Y. G. Pogorelov, M. C. Santos, and V. M. Loktev. Electric Bias Control of Impurity Effects in Bilayer Graphene. *Phys. Rev. B*, 92:075401, 2015.

[20] J. M. Thijssen. *Computational Physics*. Cambridge University Press, 1999.

[21] J. Coutinho. *Oxygen-Related Point Defects in Silicon and Germanium*. PhD thesis, Universty of Exeter, 2002.

[22] M. Born and R. Oppenheimer. Zur quantentheorie der molekeln. *Annalen der Physik*, 389(20):457–484, 1927.

[23] Attila Szabo and Neil S. Ostlund. *Modern Quantum Chemistry*. Dover Publications, Inc., 1996.

[24] R. M. Martin. *Electronic Structure - Basic Theory and Practical Methods.* Cambridge University Press, 2004.

[25] D. R. Hartree. The wave mechanics of an atom with a non-coulomb central field. part i. theory and methods. *Mathematical Proceedings of the Cambridge Philosophical Society*, 24(1):89110, 1928.

[26] M. P. Marder. *Condensed Matter Physics (chapter 9).* A Wiley-Interscience Publication, 2000.

[27] R. Jones and P. R. Briddon. *The Ab Initio Cluster Method and the Dynamics of Defects in Semiconductors*, chapter 6. Volume 51A, Semiconductors and Semimetals, Academic Press, Boston, 1998.

[28] W. Kohn and L. Sham. Self-Consistent Equations Including Exchange and Correlation Effects. *Phys. Rev.*, 140:A1133, 1965.

[29] P. Hohenberg and W. Kohn. Inhomogeneous Electron Gas. *Phys. Rev.*, 136:B864, 1964.

[30] J. Perdew and S. Kurth. *A Primer in Density Functional Theory*, chapter 1. Springer, 2002.

[31] R. G. Parr and W. Yang. *Density-Functional Theory of Atoms and Molecules.* Oxford: Oxford University Press, 1994.

[32] W. Koch and M. C. Holthausen. *A Chemist's Guide to Density Functional Theory.* Wiley-VCH Verlag GmbH, second edition edition, 2001.

[33] G. Grosso and G. P. Parravicini. *Solid State Physics.* Academic Press, 2003.

[34] G. P. Francis and M. C. Payne. Finite basis set corrections to total energy pseudopotential calculations. *J. Phys.: Condens. Matter*, 2, 1990.

[35] L. N. Kantorovich and I. I. Tupitsyn. Coulomb potential inside a large finite crystal. *J. Phys.: Condens. Matter*, 11, 1999.

[36] L. N. Kantorovich. Elimination of long-range dipole interaction in calculations with periodic boundary conditions. *Phys. Rev. B*, 60, 1999.

[37] E. Fermi. Sopra lo spostamento per pressione delle righe elevate delle serie spettrali. *Il Nuovo Cimento.*

[38] H. Hellmann. A new approximation method in the problem of many electrons. *J. Chem. Phys.*

[39] J. C. Phillips and L. Kleinman. New Method for Calculating Wave Functions in Crystals and Molecules. *Phys. Rev.*, 116:287, 1959.

[40] D. R. Hamann, M. Schlüter, and C. Chiang. Norm-Conserving Pseudopotentials. *Phys. Rev. Lett.*, 43:1494, 1979.

[41] D. Vanderbilt. Soft Self-Consistent Pseudopotentials in a Generalized Eigenvalue Formalism. *Phys. Rev. B*, 41:7892(R), 1990.

[42] P. E. Blöchl. Projector augmented-wave method. *Phys. Rev. B*, 50:17953, 1994.

[43] G. Kresse and D. Joubert. From ultrasoft pseudopotentials to the projector augmented-wave method. *Phys. Rev. B*, 59:1758, 1999.

[44] J.C. Slater. Wave Functions in a Periodic Potential. *Phys. Rev*, 51:846, 1937.

[45] Questaal Home. https://questaal.org. Last accessed: 18/12/2017.

[46] R. M. Martin. *Electronic Structure - Basic Theory and Practical Methods*. Cambridge University Press, 2004.

[47] Spherical harmonics. http://mathworld.wolfram.com/SphericalHarmonic.html. Last accessed: 10/02/2018.

[48] O. Krogh Andersen. Linear Methods in Band Theory. *Phys. Rev. B*, 12:3060–3083, Oct 1975.

[49] D. Singh. Ground-state properties of lanthanum: Treatment of extended-core states. *Phys. Rev. B*, 43.

[50] O. K. Andersen. *Computational Methods in Band Theory*. Plenum, New York, 1971.

[51] Bessel functions of the first and second kind. http://www.mhtlab.uwaterloo.ca/courses/me755/web_chap4.pdf. Last accessed: 09/01/2017.

[52] Takao Kotani and Mark van Schilfgaarde. Fusion of the LAPW and LMTO Methods: The Augmented Plane Wave Plus Muffin-Tin Orbital Method. *Phys. Rev. B*, 81:125117, Mar 2010.

[53] D. M. Ceperley and B. J. Alder. Ground State of the Electron Gas by a Stochastic Method. *Phys. Rev. Lett.*, 45:566, 1980.

[54] J. P. Perdew and A. Zunger. Self-interaction correction to density-functional approximations for many-electron systems. *Phys. Rev. B*, 23:5048, 1981.

[55] J. P. Perdew and Y. Wang. Accurate and simple analytic representation of the electron-gas correlation energy. *Phys. Rev. B*, 45:13244 – 13249, 1992.

[56] H. Jiang, R. I. Gomez-Abal, P. Rinke, and M. Scheffler. Localized and Itinerant States in Lanthanide Oxides United by *GW*@LDA+U. *Phys. Rev. Lett.*, 102:126403, 2009.

[57] J. P. Perdew, A. Ruzsinszky, G. I. Csonka, O. A. Vydrov, G. E. Scuseria, L. A. Constantin, X. Zhou, and K. Burke. Restoring the Density-Gradient Expansion for Exchange in Solids and Surfaces. *Phys. Rev. Lett.*, 100:136406, 2008.

[58] J. P. Perdew, A. Ruzsinszky, G. I. Csonka, O. A. Vydrov, G. E. Scuseria, L. A. Constantin, X. Zhou, and Kieron Burke. Erratum: Restoring the Density-Gradient Expansion for Exchange in Solids and Surfaces [Phys. Rev. Lett. 100, 136406 (2008)]. *Phys. Rev. Lett.*, 102:039902, 2009.

[59] Gábor I. Csonka, John P. Perdew, Adrienn Ruzsinszky, Pier H. T. Philipsen, Sébastien Lebègue, Joachim Paier, Oleg A. Vydrov, and János G. Ángyán. Assessing the Performance of Recent Density Functionals for Bulk Solids. *Phys. Rev. B*, 79:155107, Apr 2009.

[60] Xavier Andrade and Alán Aspuru-Guzik. Prediction of the derivative discontinuity in density functional theory from an electrostatic description of the exchange and correlation potential. *Phys. Rev. Lett.*, 107:183002, Oct 2011.

[61] John P. Perdew, Robert G. Parr, Mel Levy, and Jose L. Balduz. Density-functional theory for fractional particle number: Derivative discontinuities of the energy. *Phys. Rev. Lett.*, 49:1691–1694, Dec 1982.

[62] J. Tao, J. P. Perdew, V. N. Staroverov, and G. E. Scuseria. Climbing the density functional ladder: Nonempirical meta˘generalized gradient approximation designed for molecules and solids. *Phys. Rev. Lett.*, 91:146401, Sep 2003.

[63] T. Olsen and K. S. Thygesen. Randon phase approximation applied to solids, molecules, and graphene-metal interfaces: from van der waals to covalent bonding. *Phys. Rev. B*, 87, 2013.

[64] C. Joas X. Ren, P. Rinke and M. Scheffler. Random-phase approximation and its applications in computational chemistry and materials science. *J. Mater. Sci.*, 47, 2012.

[65] R. D. Mattuck. *A guide to Feynman Diagrams in the Many-Body Problem.* Dover Publications, Inc. New York, 2nd ed., 1976.

[66] A. L. Fetter and J. D. Walecka. *Quantum Theory of Many-Particle Systems.* Dover Publications, Inc. New York, 2003.

[67] L. Hedin. New Method for Calculating the One-Particle Green's Function with Application to the Electron-Gas Problem. *Phys. Rev.*, 139:A796, 1965.

[68] J. C. Inkson. *Many-Body Theory of Solids, An Introduction.* Plenum Press, New York, 1984.

[69] Takao Kotani, Mark van Schilfgaarde, and Sergey V. Faleev. Quasiparticle self-consistent *gw* method: A basis for the independent-particle approximation. *Phys. Rev. B*, 76:165106, Oct 2007.

[70] Mark S. Hybertsen and Steven G. Louie. Electron correlation in semiconductors and insulators: Band gaps and quasiparticle energies. *Phys. Rev. B*, 34:5390–5413, Oct 1986.

[71] B. Holm and U. von Barth. Fully self-consistent GW self-energy of the electron gas. *Phys. Rev. B*, 57:2108–2117, Jan 1998.

[72] M. T. Dove. *Structure and Dynamics*, volume 12. Oxford University Press, 2003.

[73] M. T. Dove. *Introduction to Lattice Dynamics*, volume 8. Cambridge University Press, 1993.

[74] L. Paulatto, I. Errea, M. Calandra, and F. Mauri. First-Principles Calculations of Phonon Frequencies, Lifetimes and Spectral Functions from Weak to Strong Anharmonicity: the Example of Palladium Hydrides. *arXiv:1411.5628v1 [cond-mat.mtrl-sci]*, 2014.

[75] M. T. Dove. *Introduction to Lattice Dynamics*, volume 5. Cambridge University Press, 1993.

[76] M. Sternik and K. Parlinski. Free-Energy Calculations for the Cubic ZrO_2 Crystal as an Example of a System with a Soft Mode. *J. Chem. Phys.*, 123:204708, 2005.

[77] L D Landau and E.M. Lifshitz. *Statistical Physics, Third Edition, Part 1: Volume 5.* Elsevier, Ltd, 1980.

[78] J. M. Skelton, S. C. Parker, A. Togo, I. Tanaka, and A. Walsh. Thermal physics of the lead chalcogenides PbS, PbSe, and PbTe from first principles. *Phys.Rev. B*, 89:205203, 2014.

[79] A. Togo, L. Chaput, I. Tanaka, and G. Hug. First-Principles Phonon Calculations of Thermal Expansion in Ti_3SiC_2, Ti_3AlC_2, and Ti_3GeC_2. *Phys. Rev. B*, 81:174301, 2010.

[80] K. Parlinski, Z. Q. Li, and Y. Kawazoe. First-Principles Determination of the Soft Mode in Cubic ZrO_2. *Phys. Rev. Lett.*, 78:4063, 1997.

[81] L. Chaput, A. Togo, I. Tanaka, and G. Hug. Phonon-phonon interactions in transition metals. *Phys. Rev. B*, 84:094302, 2001.

[82] F. D. Murnaghan. The Compressibility of Media under Extreme Pressures. *Proc. Natl. Acad. Sci.*, 30:244, 1944.

[83] P. Vinet, J. R. Smith, J. Ferrante, and J. H. Rose. Temperature Effects on the Universal Equation of State of Solids. *Phys. Rev. B*, 35:1945, 1987.

[84] L. H. Rimmer and M. T. Dove. Simulation Study of Negative Thermal Expansion in Yttrium Tungstate $Y_2W_3O_{12}$. *arXiv:1411.7071v1*, 2014.

[85] W. Miller, C. W. Smith, D. S. Mackenzie, and K. E. Evans. Negative Thermal Expansion: A Review. *J. Mater. Sci.*, 44:5441, 2009.

[86] P. Tschaufeser and S. C. Parker. Thermal Expansion Behavior of Zeolites and $AlP0_4$s. *J. Phys. Chem.*, 99:10609, 1995.

[87] R. Resta and D. Vanderbilt. *Physics of Ferroelectrics: A Modern Perspective, Topics Appl. Physics 105.* Springer-Verlag Berlin Heidelberg, 2007.

[88] P. Chandra and P. B. Littlewood. *Physics of Ferroelectrics: A Modern Perspective, Topics Appl. Physics 105.* Springer-Verlag Berlin Heidelberg, 2007.

[89] Nicole A. Benedek and Turan Birol. 'ferroelectric' metals reexamined: Fundamental mechanisms and design considerations for new materials. *J. Mater. Chem. C*, 4:4000–4015, 2016.

[90] R. Shaltaf, E. Durgun, J.-Y. Raty, Ph. Ghosez, and X. Gonze. Dynamical, Dielectric, and Elastic Properties of GeTe Investigated with First-Principles Density Functional Theory. *Phys. Rev. B*, 78:205203, Nov 2008.

[91] K. F. Garrity, K. M. Rabe, and D. Vanderbilt. Hyperferroelectrics: Proper Ferroelectrics with Persistent Polarization. *Phys. Rev. Lett.*, 112:127601, Mar 2014.

[92] Domenico Di Sante, Paolo Barone, Alessandro Stroppa, Kevin F. Garrity, David Vanderbilt, and Silvia Picozzi. Intertwined Rashba, Dirac and Weyl Fermions in Hexagonal Hyperferroelectrics. *Phys. Rev. Lett.*, 117:076401, Aug 2016.

[93] N. A. Spaldin. A Beginners Guide to the Modern Theory of Polarization. *J. Solid State Chem.*, 195:2–10, 2012.

[94] R. D. King-Smith and D. Vanderbilt. Theory of polarization os crystalline solids. *Phys. Rev. B*, 47:1651, 1993.

[95] R. M. Martin. *Electronic Structure - Basic Theory and Practical Methods*. Cambridge University Press, 2004.

[96] M. V. Berry. Quantal phase factors accompanying adiabatic changes. *Proc. Royal Soc. Lond. A: Math. Phys. Eng. Sci.*, 392(1802):45–57, 1984.

[97] U. V. Waghmare, N. A. Spaldin, H. C. Kandpal, and Ram Seshadri. First-principles indicators of metallicity and cation off-centricity in the iv-vi rocksalt chalcogenides of divalent ge, sn, and pb. *Phys. Rev. B*, 67:125111, Mar 2003.

[98] A. C. Garcia-Castro, Nicola A. Spaldin, A. H. Romero, and E. Bousquet. Geometric ferroelectricity in fluoroperovskites. *Phys. Rev. B*, 89:104107, Mar 2014.

[99] In Chung, Jung-Hwan Song, Jino Im, John Androulakis, Christos D. Malliakas, Hao Li, Arthur J. Freeman, John T. Kenney, and Mercouri G. Kanatzidis. $CsSnI_3$: Semiconductor or Metal? High Electrical Conductivity and Strong Near-Infrared Photoluminescence from a Single Material. High Hole Mobility and Phase-Transitions. *J. Am. Chem. Soc.*, 134:8579, 2012.

[100] L. y. Huang and W. R. L. Lambrecht. Lattice Dynamics in Perovskite Halides $CsSnX_3$ with X=I, Br, Cl. *Phys. Rev. B*, 90:195201, 2014.

[101] C. J. Howard and H. T. Stokes. Group-Theoretical Analysis of Octahedral Tilting in Perovskites. *Acta Cryst.*, B54:782, 1998.

[102] P. Vinet, J. Ferrante, J. H. Rose, and J. R. Smith. Compressibility of Solids. *J. Geophys. Res. B,*, 2:9319, 1987.

[103] Danel Orobengoa, Cesar Capillas, Mois I. Aroyo, and J. Manuel Perez-Mato. *AMPLIMODES*: Symmetry-Mode Analysis on the Bilbao Crystallographic Server. *J. App. Crystall.*, 42(5):820, Oct 2009.

[104] Amplimodes. http://www.cryst.ehu.es/cryst/amplimodes.html. Last accessed: 15/01/2018.

[105] D. Orobengoa J. M. Perez-Mato and M. I. Aroyo. Mode crystallography of distorted structures. *Acta Cryst.*, A66:558, 2010.

[106] A. V. Kolobov, D. J. Kim, A. Giussani, P. Fons, J. Tominaga, R. Calarco, and A. Gruverman. Ferroelectric switching in epitaxial gete films. *APL Materials*, 2(6):066101, 2014.

[107] Domenico Di Sante, Paolo Barone, Riccardo Bertacco, and Silvia Picozzi. Correction: Electric control of the giant rashba effect in bulk gete. *Advanced Materials*, 25(27):3625–3626, 2013.

[108] K.M. Rabe and J.D. Joannopoulos. Ab Initio Determination of a Structural Phase Transiton Temperature. *Phys. Rev. Lett.*, 59(5):570, 1987.

[109] K.M. Rabe and J.D. Joannopoulos. Theory of the Structural Phase Transiton of GeTe. *Phys. Rev. B*, 36(12):6631, 1987.

[110] M. I. Vasilevskiy and M. I. C. Ferreira. *Física dos Semicondutores*, volume 1. Edições Almedina, SA, 2005.

[111] HoSung Lee. University Lecture notes in Thermoelectrics II (Physics and Materials), ch. 11, SUM II (Tentative) 2017.

[112] P. Y. Yu and M. Cardona. *Fundamentals of Semiconductors: Physics and Materials Properties*. Number pp. 104. 1996.

[113] M. Gajdoš, K. Hummer, G. Kresse, J. Furthmüller, and F. Bechstedt. Linear Optical Properties in the PAW Methodology. *Phys. Rev. B*, 73:045112, 2006.

[114] E.F. Steigmeier and G. Harbeke. Soft Phonon Mode and Ferroelectricity in GeTe. *Solid State Communications*, 8:1275, 1970.

[115] Ruth A. Lunt, Adam J. Jackson, and Aron Walsh. Dielectric response of fe2o3 crystals and thin films. *Chemical Physics Letters*, 586:67 – 69, 2013.

[116] J. Robertson. *Comprehensive Semiconductor Science and Technology*, volume 4. Elsevier Science, 2011.

[117] I. Petousis, W. Chen, G. Hautier, T. Graf, T. D. Schladt, K. A. Persson, and F. B. Prinz. Benchmarking density functional perturbation theory to enable high-throughput screening of materials for dielectric constant and refractive index. *Phys. Rev. B*, 93, 2016.

[118] I. Petousis, D. Mrdjenovich, E. Ballouz, M. Liu, D. Winston, W. Chen, T. Graf, T. D. Schladt, K. A. Persson, and F. B. Prinz. High-throughput screening of inorganic compounds for the discovery of novel dielectric and optical materials. *Scientific Data*, 4, 2017.

[119] K. S. Novoselov, A. K. Geim, S. V. Morozov, D. Jaing, Y. Zhang, S. V. Dubonos, I. V. Grigorieva, and A. A. Firsov. Electric Field Effect in Atomically Thin Carbon Films. *Science*, 306:666, 2004.

[120] P. R. Wallace. The Band Theory of Graphite. *Phys. Rev.*, 77:622, 1947.

[121] G. Semenoff. Condensed-Matter Simulation of a Three-Dimensional Anomaly. *Phys. Rev. Lett.*, 53:2449, 1984.

[122] K. S. Novoselov, A. K. Geim, S. V. Morozov, D. Jaing, M. I. Katsnelson, I. V. Grigorieva, S. V. Dubonos, and A. A. Firsov. Two-Dimensional Gas of Massless Dirac Fermions in Graphene. *Nature*, 438:197, 2005.

[123] Y.-Y. Zhang, C. Fang, X. Zhou, K. Seo, W.-F. Tsai, B. A. Bernevig, and J. Hu. Quasiparticle Scattering Interference in Superconducting Iron Pnictides. *Phys. Rev. B*, 80:094528, 2009.

[124] V. P. Gusynin and S. G. Sharapov. Unconventional Integer Quantum Hall Effect in Graphene. *Phys. Rev. Lett.*, 95:146801, 2005.

[125] N. M. R. Peres, F. Guinea, and A. H. Castro Neto. Electronic Properties of Two-Dimensional Carbon. *Annals of Physics*, 321:1559, 2006.

[126] V. P. Gusynin, V. A. Miransky, and I. A. Shovkovy. Catalysis of Dynamical Flavor Symmetry Breaking by a Magnetic Field in 2 + 1 Dimensions. *Phys. Rev. Lett.*, 73:3499, 1994.

[127] D. V. Khveshchenko. Magnetic-Field-Induced Insulating Behavior in Highly Oriented Pyrolitic Graphite. *Phys. Rev. Lett.*, 87:206401, 2001.

[128] D. V. Khveshchenko. Ghost Excitonic Insulator Transition in Layered Graphite. *Phys. Rev. Lett.*, 87:246802, 2001.

[129] D. V. Khveschenko, A. G. Yashenkin, and I. V. Gornyj. Interacting Random Dirac Fermions in Superconducting Cuprates. *Phys. Rev. Lett.*, 86:4668, 2001.

[130] D. V. Khveshchenko. Electron Localization Properties in Graphene. *Phys. Rev. Lett.*, 97:036802, 2006.

[131] Y. Kopelevich, P. Esquinazi, J. H. S. Torres, and S. Moehlecke. Ferromagnetic- and superconducting-like behavior of graphite. *J. Low Temp. Phys.*, 119(5):691–702, Jun 2000.

[132] C. Berger, Z. Song, T. Li, X. Li, A. Y. Ogbazghi, R. Feng, Z. Dai, A. N. Marchenkov, E. H. Conrad, P. N. First, and W. A. de Heer. Ultrathin Epitaxial Graphite: 2D Electron Gas Properties and a Route Toward Graphene-Based Nanoelectronics. *J. Phys. Chem.*, 108:19912, 2004.

[133] K. S. Novoselov, E. McCann, S. V. Morozov, V. I. Fal'ko, M. I. Katsnelson, U. Zeitler, D. Jiang, F. Schedin, and A. K. Geim. Unconventional Quantum Hall Effect and Berry's Phase of 2π in Bilayer Graphene. *Nature Physics*, 2:177, 2006.

[134] E. B. Dolgusheva and V. Yu. Trubitsin. Vibrational spectra and anharmonic effects in crystals studied by molecular dynamics simulation. *AIP Conference Proceedings*, 1504(1):1150–1153, 2012.

[135] G. Cardini, P. Procacci, and R. Righini. Molecular Dynamics and Anharmonic Effects in the Phonon Spectra of Solid Carbon Dioxide. *Chem. Phys.*, 117(3):355 – 366, 1987.

[136] N. A. Benedek and C. J. Fennie. Why Are There So Few Perovskite Ferroelectrics? *J. Phys. Chem . C*, 117:13339, 2013.

[137] R. S. Akzyanov, A. O. Sboychakov, A. V. Rozhkov, A. L. Rakhmanov, and Franco Nori. *aa*-stacked bilayer graphene in an applied electric field: Tunable antiferromagnetism and coexisting exciton order parameter. *Phys. Rev. B*, 90:155415, Oct 2014.

[138] L. Paulatto M. Lazzeri N. Marzari G. Fugallo, A. Cepellotti and F. Mauri. Thermal Conductivy of Graphene and Graphite: Collective Excitationn and Mean Free Paths. *Nano Lett.*, 14.